New frontiers in G protein biology: biochemical, pharmacological, and structural characterization of intracellular signal transduction

by
Julian Harris

DISSERTATION
Submitted in partial satisfaction of the requirements for degree of
DOCTOR OF PHILOSOPHY

in

Chemistry and Chemical Biology

in the

GRADUATE DIVISION
of the
UNIVERSITY OF CALIFORNIA, SAN FRANCISCO

Approved:

DocuSigned by:
Aashish Manglik
4C1E8A184D2E493...

Aashish Manglik

Chair

DocuSigned by:
Jason Gestwicki

Jason Gestwicki

DocuSigned by:
Mark Von Zastrow
2453D8468F7C43C...

Mark Von Zastrow

Committee Members

Acknowledgements

This dissertation includes a reprint of “Selective G protein signaling driven by substance p-neurokinin receptor dynamics" as it appears in Harris, J.A.; Faust, B.; Gondin, A.B.; Dämgen, M.A.; Suomivuori, C-M.; Veldhuis, N.A.; Cheng, Y.; Dror, R.O., Thal, D.M.; Manglik, A. *Nat. Chem. Biol.* **18**, 109-115, (2022). Harris, J.A.; Faust, B.; Gondin, A.B.; Dämgen, M.A contributed equally to this work. Detailed author contributions for this work are described at the beginning of Chapter 1 of this dissertation.

This dissertation also includes unpublished results from a manuscript in preparation for submission written by Harris, J.A., Born, A., Kenanova, D., Powers, A.S., Jaimes Santiago, L., Olivares Rojas, A., Dror, R.O., Arkin, M., and Manglik, A. Harris, J.A., Born, A. and Kenanova, D. contributed equally to this work. Detailed author contributions for this work are described at the beginning of Chapter 2 of this dissertation.

The co-authors and Aashish Manglik directed and supervised the research described in this dissertation. Julian A. Harris provided the experimentation and manuscript preparation for much of the following dissertation, which is a substantive contribution comparable to other dissertations in biochemistry and chemical biology.

This material is based on work supported by the National Science Foundation Graduate Research Fellowship Program (J.A.H.) under grant no. 2034836. Any opinions, findings and conclusions or recommendations expressed in this material are those of the authors and do not necessarily reflect the views of the National Science Foundation.

-Aashish Manglik, M.D., Ph.D.

Dedication

To my advisor, Dr. Aashish Manglik: your careful, present, and unfailing support has carried me through graduate school. Thank you for sculpting me into the scientist I am incredibly proud of today. My career will forever bear the fruits of your precision, professionalism, and mentorship.

To my mentor, Dr. Ishan Deshpande: thank you for never hesitating to look at my insect cells, to recheck my FPLC protocol, and to answer my never-ending stream of questions. Your mentorship had a tremendous impact on my formative years of graduate school. You are a keen scientist with an enormous heart. My science will always carry the lessons you taught me.

To the graduate students in the Manglik Lab, Dr. Benjamin Barsi-Rhyne, Chase Webb, Nick Hoppe, Bryan Faust, and Simone Harrison: very few people in my life will ever really understand my time in graduate school. I have found so much solace, comfort, and validation in walking this path with you. You are some of brightest and most compassionate people I know. I will carry the feeling of this community for the rest of my career.

To the students I've mentored and taught, Nick Hoppe, Reuben Hogan, Ashley Olivares Rojas, Luis Jaimes Santiago, and countless others: It was an honor and a privilege to be your teacher. Thank you for entrusting me with the gift of your education. I'll carry the lessons I learned from being your mentor for the rest of my career. You taught me much more than I ever taught you.

To my parents, Kathleen and Daniel Harris: in the face of relentless and insurmountable illness, you fought hard to believe in a more optimistic future for your sons. Thank you for the gift of my education and my kind heart.

To my brother, Xander Harris: you always have, and always will be, my biggest role-model. You are an exemplar model of resilience, diligence, and compassion. You inspire me to be a better version of myself every day.

To Nicole Wenzell: I couldn't have asked for a better friend to share this grad school journey. Since day one, I've felt so affirmed, valued, and supported in our friendship. I wish I could share these last years with you in person but know I will be cheering you on from afar. You were my best friend during the hardest years of my life; a lifetime of thank you's will never be enough.

To Maura Taylor: your tremendous capacity for empathy and dedication to build a better world inspires me every day. I've never felt so seen and so valued as I do in your company. Thank you for always being my yoga partner, my kombucha companion, my Buffy-loving best friend, and one of the best people in my life.

To Jasmine Akiyama-Kim, my longest companion, my best-friend, and my birthday twin: while fate brought us together in high school speech and debate, our unfailing love keeps us close. There are two things I am most sure of in this world—your potential for greatness and your unconditional support. Your friendship is one of the greatest gifts of my lifetime.

Lastly, to my husband, Nic Tanji: you've given me more gifts in this lifetime than I can count. Thank you for your comfort, your love, and your companionship throughout this journey. My favorite thing in life is that I get to share it with you. I'll love you forever and always.

New frontiers in G protein biology: biochemical, pharmacological, and structural characterization of intracellular signal transduction

Julian Anderson Harris

Abstract

G protein-coupled receptors (GPCRs) are master regulators of human physiology and comprise the largest class of transmembrane receptors in the human genome. These cell-surface receptors respond to a wide variety of extracellular agonists—hormones, peptides, small molecules, ions, neurotransmitters—and convey this information to the cell by interacting with intracellular proteins. Heterotrimeric G proteins are the primary intracellular signaling partners of GPCRs and bind to agonist-activated GPCRs. Coupling to GPCRs causes G protein guanine nucleotide exchange. Release of inhibitory GDP and binding of activating GTP dissociates the heterotrimeric G protein, liberating the Gα and Gβγ subunits to activate downstream signaling pathways. The molecular mechanism governing GPCR-mediated activation of G proteins was first described more than 40 years ago. Nevertheless, there are fundamental aspects of GPCR–G protein biology that remain uncharacterized. This dissertation uses biochemical reconstitution, pharmacological manipulation, and structural biology to improve existing models of GPCR–G protein interactions. In chapter 1, we investigate how endogenous ligand–receptor interactions drive differential patterns of G protein engagement ($G\alpha_q$ vs. $G\alpha_s$) at a single GPCR. In chapter 2, we characterize the mechanism by which oncogenic mutations in $G\alpha_q$ drive constitutive G protein signaling in GPCR-independent pathways. We envision this work will advance our fundamental understanding of G protein biology and further translational efforts to manipulate G protein biology in human physiology.

Table of Contents

List of Figures

List of Tables

Chapter 1: Selective G protein signaling driven by substance p-neurokinin receptor dynamics

The text of this chapter is a reprint of the published manuscript “Selective G protein signaling driven by substance p-neurokinin receptor dynamics" as it appears in Harris, J.A., Faust, B., Gondin, A.B., Dämgen, M.A., Suomivuori, C-M., Veldhuis, N.A., Cheng, Y., Dror, R.O., Thal, D.M., Manglik, A. *Nat. Chem. Biol.* 18, 109-115, (2022).

Harris, J.A., Faust, B., Gondin, A., and Dämgen, M.A. contributed equally to this work.

Author contributions: Harris, J.A. purified NK1R constructs, Gβ1γ2 and Nb35, established biochemical approaches to reconstitute a NK1R–miniG protein complex and generated all NK1R mutants. Faust, B. purified Gβ1γ2 and Nb35, prepared samples for cryo-EM, identified optimal freezing conditions for cryo-EM, screened samples by cryo-EM, collected cryo-EM data and determined high-resolution cryo-EM maps by extensive image processing under the guidance of Manglik, A. and Cheng, Y. Harris, J.A. built and refined models of NK1R–miniG protein complexes with input from Faust, B. and Manglik, A. Gondin, A.B. generated NK1R stable cell lines and performed cellular signaling experiments under the guidance of Veldhuis, N.A. and Thal, D.M. Dämgen, M.A. and Suomivuori, C-M. performed and analyzed molecular dynamics simulations under the guidance of Dror, R.O. The text was written by Harris, J.A., Faust, B, Gondin, A.B., Dämgen, M.A., Suomivuori, C-M., Dror, R.O., and Manglik, A. with edits from Veldhuis, N.A., Thal, D.M., and Cheng, Y. and with approval from all authors. The overall project was supervised by Manglik, A.

1.1 Abstract

The neuropeptide substance P (SP) is important in pain and inflammation. SP activates the neurokinin-1 receptor (NK1R) to signal via Gq and Gs proteins. Neurokinin A also activates NK1R, but leads to selective Gq signaling. How two stimuli yield distinct G protein signaling at the same G protein-coupled receptor remains unclear. We determined cryogenic-electron microscopy structures of active NK1R bound to SP or the Gq-biased peptide SP6–11. Peptide interactions deep within NK1R are critical for receptor activation. Conversely, interactions between SP and NK1R extracellular loops are required for potent Gs signaling but not Gq signaling. Molecular dynamics simulations showed that these superficial contacts restrict SP flexibility. SP6–11, which lacks these interactions, is dynamic while bound to NK1R. Structural dynamics of NK1R agonists therefore depend on interactions with the receptor extracellular loops and regulate G protein signaling selectivity. Similar interactions between other neuropeptides and their cognate receptors may tune intracellular signaling.

1.2 Introduction

Substance P (SP) is a peptide with incredibly diverse roles in animal physiology. Like other neuropeptides, SP exerts long-lasting regulation of synaptic neurotransmission by activating its cognate G protein-coupled receptor (GPCR), the neurokinin 1 receptor (NK1R). SP action in the nervous system is important in pain, mood, respiration, and nausea[1]. Action of SP in other tissues is associated with inflammation or smooth muscle contraction[1]. Extensive studies suggest that inhibition of SP activity by NK1R antagonists might lead to effective treatments for pain, inflammation, and mood disorders[1], although the only clinical success to date has been for treatment of chemotherapy-induced nausea and vomiting[2].

The NK1R is endogenously activated by SP and another neuropeptide, neurokinin A (NKA). Both SP and NKA belong to the larger family of tachykinin neuropeptides that share a common C-terminal 'F(V/F)GLM-NH_2' consensus sequence, which is required for their activity at any of the three neurokinin receptors[1]. The more divergent N-terminal region of tachykinin peptides has previously been implicated in dictating which neurokinin receptor a tachykinin prefers[3]. Like other neuropeptides, tachykinin function follows the "message-address" framework, in which two distinct portions of a peptide encode either the efficacy (message) or receptor selectivity (address)[4]. Following this framework, NKA was initially described as specific for the neurokinin 2 receptor (NK2R)[3,5]. However, both SP and NKA activate NK1R in cell lines and in various physiological settings[6–9].

Intriguingly, activation of NK1R by SP or NKA induces distinct cellular responses and, in certain tissues, distinct physiological outcomes[7,10]. SP increases both inositol phosphate (IP) and cAMP second messengers downstream of G_q and G_s signaling pathways, respectively[8,9]. By contrast, NKA signals potently via G_q but has decreased G_s stimulatory activity[8,9]. Molecular pharmacology studies revealed that SP binding to NK1R is distinct from NKA binding[11,12]. A

common model proposed by these studies is that NK1R exists in two distinct active conformations: an SP-selective state and a general-tachykinin state that binds both SP and NKA[12,13]. Mutations can alter the relative proportion of these two states, yielding changes in the measured affinities for SP, NKA and related tachykinins[9,12]. These mutations also dramatically affect the ability of NK1R to signal via G_q or G_s, suggesting that these distinct active conformations are coupled to distinct signaling outcomes[9].

The ability of two agonists to induce distinct intracellular signaling cascades downstream of a single GPCR is well established. However, how two endogenous stimuli yield distinct G protein coupling preference at the same receptor remains unclear at the biochemical and structural level. Here, we combine structural biology with molecular dynamics simulations and cellular signaling studies to decipher the molecular basis of agonist-dependent G protein-selective signaling at the NK1R.

1.3 Results

Structure of the SP-NK1R-miniG$_{s/q70}$ complex

To enable structure determination of active human NK1R without thermostabilizing mutations or truncations, we generated a construct with the engineered Gα subunit miniG$_{s/q70}$[14] fused to the C-terminus of the receptor. The miniG$_{s/q70}$ protein presents the GPCR-interacting α5 helix of Gα$_q$ on an engineered Gα$_s$ protein stabilized in the active conformation and with complete truncation of the Gα alpha-helical domain. This strategy improved the biochemical stability of Substance P (SP)-bound receptor compared to NK1R alone (Extended Data Fig. 1.1). Purified SP-bound NK1R-miniG$_{s/q70}$ fusion protein was mixed with excess Gβγ and nanobody 35 (Nb35)[15] for structure determination by cryogenic-electron microscopy (cryo-EM) (Extended Data Fig. 1.1).

We determined a cryo-EM structure of the SP-NK1R-G$_{s/q70}$ complex at a global resolution of 3.0 Å (Fig. 1.1a and Extended Data Fig. 1.2). As is common for many GPCR-G protein complex structures, our initial maps yielded poor resolution for SP, the orthosteric binding pocket, and the extracellular loops. To improve reconstruction in these regions, we performed iterative focused refinements using a mask encompassing only the upper transmembrane region of the 7TM bundle. The resulting improved maps enabled an atomic model for all subunits of the complex and the SP peptide (Fig. 1.1b, Extended Data Fig. 1.2, Extended Data Fig. 1.3).

SP-activated NK1R is in a distinct active conformation when compared to other class A GPCRs. Like other GPCRs, active NK1R displays an 8.3 Å movement of transmembrane helix 6 (TM6) away from the 7TM helical bundle, enabling insertion of the C-terminal α5-helix of the miniG$_{s/q70}$ protein (Fig. 1.1c). This movement is associated with other conserved changes in class A GPCR activation, including displacement of the W$^{6.48}$ 'toggle-switch' (superscripts denote Ballesteros-Weinstein numbering[16]), rearrangement of the 'P$^{5.50}$I$^{3.40}$F$^{6.44}$' connector motif, and movement of the 'D$^{3.49}$R$^{3.50}$Y$^{3.51}$' motif (Extended Data Fig. 1.4)[15]. These conformational

changes link ligand binding in the orthosteric site to the intracellular G protein coupling site and facilitate G protein binding.

By contrast, the conserved '$N^{7.49}P^{7.50}xxY^{7.53}$' motif in the SP-NK1R-mini$G_{s/q70}$ structure remains in an inactive conformation. A hallmark of class A GPCR activation is inward movement of TM7 into the helical core[15] (Fig. 1.1d). This allows $Y^{7.53}$ of the NPxxY motif to engage in an extended water-mediated hydrogen bonding-network with other residues on the cytoplasmic face of TM3 and TM5, as observed for the active μ opioid receptor[17,18] (Fig. 1.1e). This inward movement of $Y^{7.53}$ is not observed in the SP-NK1R-mini$G_{s/q70}$ structure and TM7 remains in a conformation that closely resembles the inactive-state (Fig. 1.1e). Other structures of GPCRs solved in complex with $G_{q/11}$ family G proteins, miniG_s, and mini$G_{s/q70}$ proteins show canonical inward movement of TM7 upon receptor activation[19–21].

The unique active-state of SP-bound NK1R resembles a previously determined structure of the neurotensin 1 receptor (NTS_1R) bound to the cAMP inhibitory G protein G_i[22,23]. Two active-state conformations of NTS_1R bound to G_i have previously been observed: a canonical state with inward movement of TM7 and a 'noncanonical' state without TM7 rearrangement[22] (Fig. 1.1e). Although the 7TM of NK1R bound to mini$G_{s/q70}$ is in a similar conformation to the noncanonical NTS_1R conformation, we do not observe the 45° rotation of the G protein observed for noncanonical NTS_1R (Extended Data Fig. 1.4). While there are important caveats to our interpretation of the interactions between NK1R and the engineered mini$G_{s/q70}$ protein, we surmise that fully active NK1R bound to the C-terminus of G_q exists in a unique conformation compared to most class A GPCRs.

Unlike most (98%) of class A GPCRs, NK1R possesses a glutamate residue at the highly conserved $D^{2.50}$ position[24]. In inactive-state class A GPCRs, this canonical $D^{2.50}$ residue

participates in an extended, water-mediated hydrogen-bonding network between TM helices 2, 3, 6 and 7. For most GPCRs, activation is coupled with an inward movement of TM7 driven by a direct interaction between $D^{2.50}$ and $N^{7.49}$ (Extended Data Fig. 1.4) of the NPxxY motif. By contrast, $E78^{2.50}$ forms a direct interaction with $N301^{7.49}$ in the NK1R inactive-state. We speculate that the stable and direct $E^{2.50}$-$N^{7.49}$ interaction in the NK1R inactive-state disfavors inward TM7 motion during activation and contributes to the noncanonical active-state. Indeed, previous work has shown that disrupting the $E^{2.50}$-$N^{7.49}$ interaction with mutagenesis selectively diminishes G_s signaling but does not affect G_q signaling[25], suggesting that the noncanonical NK1R active conformation is important for robust G_s and G_q signaling downstream of NK1R activation.

Molecular recognition of SP by NK1R

SP binds with an expansive interface stretching from a deeply buried 7TM pocket to the distal portions of the NK1R ECL2 and N-terminus (Fig. 1.2a). We observed clearly resolved cryo-EM density for SP C-terminal residues 6-11, enabling us to unambiguously model this portion of the peptide (Fig. 1.2a). The N-terminal portion of SP, including residues 1-5, interact primarily with the extracellular loop 2 (ECL2) and the N-terminus of NK1R. The density for these residues is less well resolved, but we were able to confidently place all mainchain atoms and all side chains with the exception of R1 and K3.

SP binds to NK1R in a distinct manner compared to other neuropeptides at their cognate receptors. We compared the binding of SP to the NTS_1R bound to neurotensin 8-13[22], the μ-opioid receptor bound to the peptide mimetic agonist DAMGO[26], and the orexin 2 receptor bound to orexin B[27] (Extended Data Fig. 1.5). All of these neuropeptides make extensive contacts with the deep 7TM pocket, likely important for determining their efficacy as agonists for their respective receptors. The extended conformations of the peptides in the receptor binding

pockets enable further interactions with the extracellular loops. In contrast to the binding of these other neuropeptides at their cognate receptors, SP makes more extensive contacts with ECL2 and the N-terminus of NK1R, manifesting as an outward displacement of the extracellular tip of TM1 and a more ordered N terminus (Extended Data Fig. 1.5).

The SP orthosteric binding pocket is distinct from the binding sites of NK1R antagonists determined in previous inactive-state structures[24,28]. For example, the antagonist netupitant (Protein Data Bank (PDB) ID 6HLP, ref[24]) minimally overlaps with SP (Fig. 1.2b), with only the 2-methylphenyl and 3,5-bis(trifluoromethyl)phenyl groups of netupitant binding in the same region as M11 of SP (Fig. 1.2b). The core of the netupitant antagonist scaffold, however, extends along TM4 and TM5 toward the extracellular region of the receptor in a portion of the orthosteric pocket that is not occupied by SP. All structurally characterized NK1R antagonists possess a similar molecular scaffold to netupitant and bind to a relatively small portion of the total SP binding site (Extended Data Fig. 1.5). This distinct binding topology is consistent with prior mutagenesis data, which found only two NK1R residues, Q165$^{4.60}$ and Y287$^{7.35}$, are important for both SP and non-peptide antagonists binding[29] (Extended Data Fig. 1.5).

The expansive SP-NK1R interface is consistent with prior mutagenesis efforts, which found that residues both within the deep 7TM site and the NK1R N-terminus potently reduce SP binding affinity[29]. Our structure of the SP-NK1R complex revealed that the amidated C-terminus of SP forms an extensive hydrogen-bonding network with NK1R residues N85$^{2.57}$, N89$^{2.61}$, H108$^{3.28}$, and Y287$^{7.35}$ (Fig. 1.2d). To finely probe the importance of specific hydrogen bonds in SP binding to NK1R, we tested the ability of SP to activate NK1R mutants with conservative amino acid substitutions at these key positions in a Ca^{2+} mobilization assay. In contrast to the dramatic loss of potency previously observed with non-conservative alanine mutations at these sites[29],

we observed relatively minor changes in SP potency or maximal efficacy with these conservative mutations (Fig. 1.2e, Extended Data Fig. 1.6, Supplementary Table 1.1)

We hypothesized that other SP–NK1R interactions, perhaps those in the extracellular regions of the receptor, could compensate for the disrupted hydrogen bonding network in the deep portion of the NK1R pocket. To test this, we examined the potency and efficacy of a truncated version of SP containing only residues 6-11 (SP6-11, Fig. 1.3a), which would be unable to interact with the NK1R ECL2 and N-terminus. As observed previously[8,9], we found that SP6-11 is equally potent as SP in stimulating Ca^{2+} signaling and IP1 accumulation at wild-type NK1R (Fig. 1.3b,c, Supplementary Table 1.2). When tested against our conservative NK1R mutants targeting the SP C-terminal amide hydrogen bonding network, we observed a dramatic 30-1,000 fold loss in potency for SP6-11 (Fig. 1.2e, Supplementary Table 1.1). We therefore conclude that the extensive hydrogen bonding network recognizing the amidated C-terminus of SP is indeed important for Ca^{2+} signaling, but that the extended contacts between SP and NK1R in the extracellular regions serve an important role in NK1R signaling beyond simply dictating the tachykinin receptor subtype selectivity of SP.

Structural interrogation of NK1R signaling bias

While SP potently activates both G_q and G_s signaling downstream of NK1R, NKA and N-terminally truncated SP analogs are weaker agonists of G_s signaling[8,9]. We confirmed these prior results in signaling studies. SP, NKA, and SP6-11 produced equally potent and efficacious Ca^{2+} and IP signaling responses (Fig. 1.3b,c, Supplementary Table 1.2). By contrast, NKA and SP6-11 were 6- and 16-fold less potent than SP in eliciting cAMP accumulation, respectively (Fig. 1.3d, Supplementary Table 1.2), confirming their G_q selective signaling profiles. As kinetic parameters of G protein signaling can confound the determination of ligand signaling profiles[30], we sought to further characterize SP, NKA, and SP6-11 with time-resolved Ca^{2+} and cAMP

signaling studies (Extended Data Fig. 1.6). The kinetic profile of SP, NKA, and SP6-11 elicited Ca^{2+} and cAMP signaling responses do not appreciably differ from each other. However, NKA and SP6-11 fail to robustly activate cAMP accumulation at all examined time points, confirming our previous observation that NKA and SP6-11 are G_q selective.

Prior pharmacology studies have demonstrated that SP and its analogs bind to NK1R in two distinct conformations that likely depend on the specific G protein coupled to the receptor[12,31]. Indeed, NK1R-G_q and NK1R-G_s fusion proteins display different binding affinities for SP[31], suggesting that G_q- and G_s-coupled NK1R exist in distinct conformations. We performed bioluminescence resonance energy transfer (BRET) experiments[32] examining recruitment of mini$G_{s/q}$ and a miniG protein analog of G_s (miniG_s) to NK1R activated by SP, SP6-11, and NKA. SP6-11 is 5-fold less potent than SP at recruiting mini$G_{s/q}$ and roughly 60-fold weaker than SP in inducing miniG_s recruitment (Extended Data Fig. 1.6, Supplementary Table 1.3), suggesting that agonist-specific NK1R signaling with wild-type G proteins also extends to NK1R binding to miniG proteins. We therefore reasoned that additional cryo-EM structures of active NK1R may provide insight into how SP and other tachykinins induce distinct G_q and G_s signaling outcomes. In particular, we speculated that differences in the SP-ECL2 interaction interface may explain the diminished G_s agonism of NKA and SP6-11. To explore how SP induces G_s signaling, we determined the structure of SP-NK1R bound to miniG_{s399} at 3.1 Å resolution (Fig. 1.3e, Extended Data Fig. 1.1, Extended Data Fig. 1.7). Furthermore, to understand how NKA and SP6-11 induce G_q selective NK1R signaling, we determined the structure of a SP6-11-NK1R-mini$G_{s/q70}$ complex at 3.2 Å resolution (Fig. 1.3f, Extended Data Fig. 1.1, Extended Data Fig. 1.8).

The structure of the SP-NK1R-miniG_{s399} complex is almost identical to our SP-NK1R-mini$G_{s/q70}$ complex, with overall NK1R root mean square deviation (RMSD) of 0.43 Å. Importantly, we

observe clearly resolved EM density for the N-terminus of SP, which interacts with the NK1R extracellular regions in a very similar manner to the SP-NK1R-mini$G_{s/q70}$ structure (Extended Data Fig. 1.9). The similarity in these SP-NK1R-miniG protein structures suggests that the overall conformation of G_q- and G_s-coupled NK1R may be similar while bound to SP. However, there are important caveats to this interpretation. First, the primary interaction between NK1R and the miniG proteins is the insertion of the G protein C-terminal α5-helix into the receptor 7TM core. In the chimeric mini$G_{s/q70}$ protein, the α5-helix is derived from G_q, whereas the remainder of the mini$G_{s/q70}$ protein is derived from G_s. It is possible that the interaction between NK1R and wild-type G_q may be different from what we observe with mini$G_{s/q70}$ here. Both miniG proteins used here have been engineered to stabilize the active G protein conformation and increase the affinity of the G protein–GPCR interaction. We therefore cannot rule out the possibility that these modifications may influence the specific conformation of NK1R that we observed in our structures. Finally, our cryoEM reconstructions capture a single, low-energy state of a nucleotide-free NK1R-miniG protein complex. It is also possible that G_q and G_s signaling selectivity arises from transient NK1R G protein-coupled states that are not structurally observed in our work.

The structure of SP6-11 activated NK1R-mini$G_{s/q70}$ also revealed a highly similar receptor-G protein conformation when compared to full-length SP, with notable exceptions in the peptide binding site (Fig. 1.3g,h and Extended Data Fig. 1.9). We observed a shorter density for SP6-11 in the orthosteric binding pocket, consistent with the N-terminal truncation of SP. The cryo-EM density for SP6-11 is comparatively worse than the density for both full-length SP reconstructions when viewed with unsharpened maps at the same enclosed volume threshold (Fig. 1.3g,h). Specifically, there is a lack of continuous electron density between the peptide backbone and the F7 sidechain and the electron density for the M11 sidechain is completely missing. By contrast, the density for the receptor is comparatively well resolved for both full-

length SP and SP6-11 structures, suggesting that the weaker density we observed for SP6-11 does not arise from local resolution artifacts (Extended Data Fig. 1.9). Selectively weaker density for F7 and M11 may arise from increased dynamic motion of SP6-11 compared to full-length SP. We speculate that increased SP6-11 dynamic motion may result from a lack of stabilizing contacts between the N-terminus of SP and the extracellular regions of NK1R, potentially leading to both increased sensitivity of SP6-11 to mutations in the deep 7TM pocket (Fig. 1.2e) and decreased potency of SP6-11-mediated G_s-signaling (Fig. 1.3d).

Truncation of SP N terminus increases C terminus motility

We turned to all-atom molecular dynamics (MD) simulations to understand the mechanism by which SP N-terminal truncation leads to Gq selective signaling. To this end, we performed 12 independent 2-μs simulations of active NK1R bound to SP and another 12 of active NK1R bound to SP6-11.

In our simulations, SP6-11 is less restrained in its motion than the corresponding C-terminal residues of SP and explores more space within the binding pocket (Fig. 1.4). SP6-11 residues F7 and M11 exhibit particularly notable differences in dynamics compared to SP. In simulations of NK1R bound to full-length SP, the F7 side chain remains mostly between TM7 and TM2, as in the SP-bound NK1R structure (Fig. 1.4a). In simulations with SP6-11, on the other hand, the F7 side chain samples a wider range of orientations (Fig. 1.4c). The side chain of M11 adopts two major orientations in simulations of SP: one pointing between TM5 and TM6 as in the SP-bound structure of NK1R and one pointing between TM6 and TM7. For SP6-11, we observe a wider range of M11 side chain orientations with additional conformations pointing towards TM6 and TM7 (Fig. 1.4c). Altogether, we observe a significant increase in the root mean square fluctuation (r.m.s.f.) for SP6-11 bound to NK1R, both for the entire C-terminal peptide region and for the F7 and M11 residues (Fig. 1.4b). This increased flexibility is consistent with poorly

resolved regions for the SP6-11 peptide in our cryo-EM structure (Fig. 1.3h). Furthermore, increased flexibility of NK1R-bound SP6-11 is consistent with previous studies reporting that SP6-11-like ligands dissociate faster from NK1R with slightly lower binding affinities than SP[12,33]. We conclude that disruption of the interactions between the SP N-terminus and the NK1R leads to destabilization of SP C-terminal residues.

The different orientations observed for M11 and F7 affect contacts with TM7. Given that active NK1R is already in an unusual noncanonical conformation, with TM7 inactive but TM6 in an outward position, it is tempting to speculate that these different interactions with TM7 could also stabilize distinct intracellular conformations differing in TM7 conformation. Different TM7 conformations have been previously shown to mediate differential signaling responses of another peptidergic GPCR, the angiotensin II type 1 receptor[34].

Disruption of SP contacts with ECL2 biases signaling

Our simulations suggested that the interactions of the N-terminal region of SP with NK1R ECL2 serve to stably position the C-terminus of the peptide. Disruption of these interactions may therefore destabilize the C-terminal region of SP and achieve similar G_q preferential signaling as observed for SP6-11. In support of this hypothesis, our molecular dynamics simulations of SP and SP6-11 bound to NK1R suggest that SP6-11 spends less time than SP in contact with R177, a residue on ECL2 that interacts with both peptides (Extended Data Fig. 1.10). To directly test the relevance of interactions between ECL2 and SP, we designed NK1R mutations that disrupt the SP-ECL2 interface (Extended Data Fig. 1.10). Two such mutations, M174I and R177M, displayed G_q preferential signaling by SP. In structures of NK1R bound to SP, M174 makes hydrophobic contacts with F8 of SP while R177 forms an extended hydrogen-bond network with the SP backbone and NK1R residues N96$^{2.68}$ in TM2 and N23 in the N-terminus (Fig. 1.5a). In signaling studies, both M174I and R177M are equally potent and efficacious as

wild-type NK1R at Ca^{2+} mobilization and IP1 accumulation (Fig. 1.5b,c, Supplementary Table 1.1). By contrast, both of these mutations notably decrease cAMP production by SP, with R177M displaying a 20-fold reduction in potency and a greater than 3-fold reduction in efficacy compared to wild-type NK1R (Fig. 1.5d, Supplementary Table 1.1). These mutants are expressed at similar levels as wild-type NK1R and the kinetic profiles of G_q and G_s signaling for both mutants do not appreciably differ from wild-type NK1R (Extended Data Fig. 1.10). Contacts between SP and NK1R ECL2 are therefore critically important for potent G_s-coupled cAMP signaling.

1.4 Discussion

Substance P is a prototypical member of the broader family of neuropeptides that act at GPCRs to modulate neuronal function. Our structures of full-length SP bound to active NK1R revealed an extensive contact interface with NK1R, stretching from the deeply buried regions in the 7TM domain to the extracellular regions of the receptor. A network of specific hydrogen bonds between the amidated C-terminus of SP and the deep orthosteric pocket of NK1R are important for peptide recognition; removal of specific hydrogen bonds impairs the ability of SP6-11 to activate NK1R. Our structures also reveal important contacts between the SP N-terminus and the extracellular loops of NK1R, providing insight into how less-conserved sequences in neuropeptides engage their cognate receptors. These high-resolution observations further establish the significance of ligand interactions at the extracellular receptor surface, as has been observed for multiple other GPCRs[35]. While our structural views of full-length neuropeptides bound to their cognate GPCRs remains limited to only a few other examples, an emerging theme is that peptides bind in an extended manner, with regions of the peptide engaging the receptor extracellular loops.

Our work revises the 'message-address' model for peptidergic signaling at GPCRs. In particular, we demonstrate that interactions between the N-terminal region of SP and the extracellular loops of NK1R, which were previously characterized as conferring receptor subtype selectivity, are also required for balanced signaling via both the G_q and G_s signaling pathways. Loss of these interactions, due to either truncation of SP's N-terminus or NK1R ECL2 mutations, leads to G_q-selective signaling. Other endogenous tachykinins that signal selectively via G_q, such as NKA, probably do so because they lack sequences that can engage the NK1R extracellular loops. Neuropeptide regions that engage GPCR extracellular loops may therefore specify not only which receptor subtype a peptide preferentially engages but also the signaling outcomes downstream of a specific GPCR.

Our work has broader implications for other neuropeptide GPCRs. Pharmacological studies with other neuropeptides, including opioid peptides[36], neuropeptide S[37], and neuropeptide Y[38] suggest that interactions between the divergent, less conserved regions of the neuropeptide and their cognate receptor extracellular loops, which also diverge in sequence, can tune signaling efficacy via multiple G proteins or β-arrestins. Our work highlights the role of peptide-receptor extracellular contacts in determining the conformational flexibility of the core “message” region of SP. A similar mechanism may be responsible for fine-tuning intracellular signaling, or for promoting a complete signaling response when multiple endogenous neuropeptides are present and acting at a single GPCR. Assessing the structure and dynamics of neuropeptides bound to their cognate receptors thus promises to yield a mechanistic understanding of what drives GPCR signaling complexity, and may eventually provide a path to control such complex signaling with designed molecules.

1.5 Materials and Methods

Expression and purification of Substance P-NK1R-miniG$_{s/q70}$ complex

For structure determination, human *TACR1* with an N-terminal HA signal sequence followed by a FLAG epitope tag was cloned into a pcDNA^{TM}3.1/Zeo$^{(+)}$ vector containing a tetracycline-inducible expression cassette. The miniG$_{s/q70}$ protein[14] was fused to the NK1R C-terminus, preceded by a flexible glycine/serine linker and rhinovirus 3C protease recognition site (LEVLFQGP). The resulting NK1R-miniG$_{s/q70}$ fusion construct was transfected into adherent Expi293F^{TM} Inducible Human Embryonic Kidney Cells (unauthenticated and untested for mycoplasma contamination, Life Technologies) using Lipofectamine 2000© and cells were maintained in DMEM (Gibco, 11995-065) + 10% FBS (Gibco), 100 U/mL penicillin and 100 µg/mL streptomycin at 37 °C and 5% CO_2 in a standing incubator. Cells stably incorporating the NK1R-miniG$_{s/q70}$ fusion plasmid were selected under antibiotic pressure with zeocin (500 µg/mL) and blasticidin (10 µg/mL). The resulting polyclonal Expi293F^{TM} NK1R-miniG$_{s/q70}$ stable cell line was then adapted to suspension culture and maintained in Expi293^{TM} Expression Medium (Gibco) supplemented with zeocin (5 µg/mL) and blasticidin (5 µg/mL) at 37 °C and 8 % CO_2 on a shaking platform at 125 rpm. Expression of NK1R-miniG$_{s/q70}$ fusion protein was induced with addition of 4 µg/mL doxycycline hyclate (Sigma Aldrich) and enhanced with 20 mM sodium butyrate (Sigma Aldrich). Two liters of induced Expi293F^{TM} NK1R-miniG$_{s/q70}$ stable cells were harvested 24 hours after induction and stored at -80 °C until further use.

For purification, cells were thawed and washed with hypotonic buffer (20 mM HEPES pH 7.5, 1 mM EDTA) supplemented with protease inhibitors (20 µg/mL leupeptin, 160 µg/mL benzamidine, 1 mM PMSF), reducing agent (100 µM TCEP) and 100 nM Substance P (Tocris). The membrane fraction was then solubilized with 50 mM HEPES pH 7.5, 300 mM NaCl, 1% (w/v) lauryl maltose neopentyl glycol (L-MNG, Anatrace), 0.1% cholesteryl hemisuccinate (CHS, Steraloids), protease inhibitors, 100 µM TCEP, 5 mM ATP, 2 mM $MgCl_2$, and 1 µM Substance P

for 1.5 hours at 4 °C. After high-speed centrifugation, the supernatant was subjected to affinity purification using homemade M1 anti-FLAG antibody coupled to Sepharose beads. NK1R-mini$G_{s/q70}$ bound to M1-beads was washed extensively to gradually decrease detergent and salt concentration and was eluted in 50 mM HEPES pH 7.5, 150 mM NaCl, 0.0075% (w/v) L-MNG, 0.0025% (w/v) glyco-diosgenin (GDN, Anatrace), 0.001% CHS, 100 µM TCEP, 100 nM Substance P, 5 mM EDTA, and 0.2 mg/mL FLAG peptide (Genscript). Eluted NK1R-mini$G_{s/q70}$ was concentrated with a 50 kDa MWCO spin concentrator (Millipore) and purified to homogeneity with size-exclusion chromatography, using a Superdex S200 Increase 10/300 GL column (GE Healthcare) equilibrated in 20 mM HEPES pH 7.5, 150 mM NaCl, 0.0075% (w/v) L-MNG, 0.0025% (w/v) GDN, 0.001% CHS, 100 µM TCEP, and 100 nM Substance P. Fractions containing monodisperse NK1R-mini$G_{s/q70}$ fusion protein were pooled, mixed with 2.5x molar excess of $G\beta_1\gamma_2$ heterodimer, Nb35[15], and Substance P, and incubated overnight at 4 °C. The next day, the heterotrimeric complex was concentrated with a 50 kDa MWCO spin concentrator and excess $G\beta_1\gamma_2$ and Nb35 was removed via size-exclusion chromatography, using a Superdex S200 Increase 10/300 GL column (GE Healthcare) equilibrated in 20 mM HEPES pH 7.5, 150 mM NaCl, 0.00075% (w/v) L-MNG, 0.00025% (w/v) GDN, 0.0001% CHS, 100 µM TCEP, and 100 nM Substance P. Resulting SP-NK1R-mini$G_{s/q70}$ heterotrimeric complex was concentrated with a 50 kDa MWCO spin concentrator to 1.93 mg/mL (14 µM) for preparation of cryo electron microscopy grids.

Expression and purification of Substance P (6-11)-NK1R-mini$G_{s/q70}$ complex

The SP6-11-bound NK1R-mini$G_{s/q70}$ fusion protein was expressed and purified exactly as described above for the SP-NK1R-mini$G_{s/q70}$ fusion protein, except for replacing all SP incubations with SP6-11 throughout the purification. Incubation of SP6-11-NK1R-mini$G_{s/q70}$ fusion protein with $G\beta_1\gamma_2$ and Nb35 was performed as described above for the SP complex. The resulting SP6-11-NK1R-mini$G_{s/q70}$ heterotrimeric complex was concentrated with a 50 kDa

MWCO spin concentrator to 2.91 mg/mL (21 µM) for preparation of cryo electron microscopy grids.

Expression and purification of Substance P-NK1R-miniG$_{s399}$ complex

The NK1R-miniG$_{s/q70}$ fusion construct (generation described above) was modified to replace the miniG$_{s/q70}$ protein with the miniG$_{s399}$[21] protein using Gibson cloning. The subsequent NK1R-miniG$_{s399}$ fusion construct was transiently transfected into 200-mLs of Expi293F™ Inducible Human Embryonic Kidney Cells (unauthenticated and untested for mycoplasma contamination, Life Technologies) using the Expifectamine Transfection Kit (Life Technologies), following the manufacturer's instructions. Expression of the NK1R-miniG$_{s399}$ fusion protein was induced and enhanced 18 hours after transfection with addition of 1 µg/mL doxycycline hyclate (Sigma Aldrich), 10 mM sodium butyrate (Sigma Aldrich), and addition of enhancers from the Expifectamine Transfection Kit, as per the manufacturer's instructions. Cells were harvested 24 hours after induction and stored at -80 °C until further use.

The SP-NK1R-miniG$_{s399}$ fusion protein was purified exactly as described above for the SP-NK1R-miniG$_{s/q70}$ fusion protein. Incubation of SP-NK1R-miniG$_{s399}$ fusion protein with G$\beta_1\gamma_2$ and Nb35 was performed exactly as described above for the SP-NK1R-miniG$_{s/q70}$ complex. The resulting SP-NK1R-miniG$_{s399}$ heterotrimeric complex was concentrated with a 50 kDa MWCO spin concentrator to 2.86 mg/mL (20 µM) for preparation of cryo electron microscopy grids.

Expression and purification of G$\beta_1\gamma_2$

The G$\beta_1\gamma_2$ heterodimer was expressed in *Trichoplusia ni* (Hi5) insect cells (Expression Systems, unauthenticated and untested for mycoplasma contamination) using a single baculovirus. Briefly, a single bicistronic baculovirus encoding the human Gβ_1 subunit with a N-terminal 6x His-tag and rhinovirus 3C protease site and untagged human Gγ_2 subunit was generated using

the BestBac method (Expression systems) in *Spodoptera frugiperda* (Sf9) insect cells (Expression Systems 94-001F, unauthenticated and untested for mycoplasma contamination). Hi5 insect cells were transduced with baculovirus at a density of ~3.0 x 10^6 cells/mL, grown at 27 °C and shaking at 130 rpm. Cultures were harvested 48 hours after transduction, and cell pellets were stored at -80 °C until further use. Frozen cell pellets were thawed and washed in a hypotonic buffer containing 10 mM Tris pH 8.0, 5 mM β-mercaptoethanol (β-ME), and protease inhibitors (20 µg/mL leupeptin, 160 µg/mL benzamidine). The membrane fraction was collected by centrifugation and then solubilized with 20 mM HEPES pH 7.5, 100 mM NaCl, 1% (w/v) sodium cholate, 0.05% dodecyl maltoside (DDM, Anatrace), 0.005% cholesteryl hemisuccinate (CHS, Steraloids), 5 mM β-ME, protease inhibitors, and 5 mM Imidazole for 1 hour at 4 °C. After high-speed centrifugation, the supernatant was subjected to affinity purification with HisPur™ Ni-NTA resin (Thermo Scientific). Bound $G\beta_1\gamma_2$ heterodimer was washed extensively, and detergent was slowly exchanged to 0.1% (w/v) lauryl maltose neopentyl glycol (L-MNG, Anatrace) and 0.01% CHS before elution with 20 mM HEPES pH 7.5, 100 mM NaCl, 0.1% L-MNG, 0.01% CHS, 270 mM imidazole, 1 mM dithiothreitol (DTT), and protease inhibitors. Eluted $G\beta_1\gamma_2$ heterodimer was pooled and 3C protease was added to cleave the N-terminal 6x His-tag. The resulting $G\beta_1\gamma_2$ heterodimer was dialyzed overnight in 20 mM HEPES pH 7.5, 100 mM NaCl, 0.02% L-MNG, 0.002% CHS, 1 mM DTT, and 10 mM imidazole. Reverse Ni-NTA affinity chromatography was performed to remove uncleaved heterodimer. The resulting $G\beta_1\gamma_2$ was then incubated for 1 hour at 4 °C with lambda phosphatase (New England Biolabs), calf intestinal phosphatase (New England Biolabs), and antarctic phosphatase (New England Biolabs) to dephosphorylate the protein. $G\beta_1\gamma_2$ was further purified by anion exchange chromatography using a MonoQ 4.6/100 PE (GE Healthcare) column. The resulting protein was pooled and dialyzed overnight in 20 mM HEPES pH 7.5, 100 mM NaCl, 0.02% L-MNG, and 100 µM TCEP, concentrated with a 3 kDa centrifugal concentrator. Glycerol was added to a final

concentration of 20%, and the protein was flash frozen in liquid N_2 and stored at -80 °C until further use.

Expression and purification of Nb35

Nanobody35 (Nb35)[15] with a N-terminal pelB signal sequence and a C-terminal Protein C affinity tag (EDQVDPRLIDGK) was cloned into a pET-26b IPTG-inducible bacterial expression vector. This vector was transformed into BL21 Rosetta *Escherichia coli* cells and grown overnight in Luria Broth supplemented with 50 µg/mL kanamycin shaking at 225 rpm and 37 °C. Next day, the saturated overnight culture was used to inoculate 8 L of Terrific Broth (supplemented with 0.1% glucose, 2 mM MgCl2, and 50 µg/mL kanamycin) and cells were grown shaking at 225 rpm at 37 °C. When cells reached an OD_{600} = 0.6, expression of Nb35 was induced with addition of 400 µM IPTG and the temperature was reduced to 20 °C for 21 hours. Cells were harvested by centrifugation and stored in the -80 °C until further use. For purification of Nb35, cells were thawed and resuspended in SET Buffer (200 mM Tris pH 8.0, 500 mM sucrose, 0.5 mM EDTA) supplemented with protease inhibitors (20 µg/mL leupeptin, 160 µg/mL benzamidine) and benzonase. After 30 minutes of stirring, two equal volumes of miliQ H_2O were added to initiate hypotonic lysis. After 45 minutes of stirring, NaCl was added to 150 mM, CaCl2 was added to 2 mM, and MgCl2 was added to 2mM. Insoluble matter was then separated by high-speed centrifugation and the supernatant was subjected to affinity purification with homemade anti-Protein C antibody coupled to Sepharose beads. After extensive washing, bound Nb35 was eluted with 20 mM HEPES pH 7.5, 100 mM NaCl, and 2 mM CaCl2, 0.2 mg/mL Protein C peptide, and 5 mM EDTA pH 8.0. Eluted Nb35 was collected, concentrated, and injected over an Superdex S75 Increase 10/300 GL column (GE Healthcare) size-exclusion chromatography column equilibrated in 20 mM HEPES pH 7.5, 100 mM NaCl. Fractions containing Nb35 were collected, concentrated, glycerol was added to a final concentration of

20%, and aliquots of Nb35 were flash frozen in liquid nitrogen and stored in the -80 °C until further use.

Cryo-EM sample vitrification and data collection

For cryogenic electron microscopy, 3 µL of the SP-NK1R-mini$G_{s/q70}$ heterotrimeric complex at 13.8 µM was added to 300 Mesh 1.2/1.3R Au Quantifoil grids previously glow discharged at 15 mA for 30 seconds with a Pelco easiGlow Glow discharge cleaning system. Grids were blotted with Whatman No. 1 qualitative filter paper in a Vitrobot Mark IV (Thermo Fisher) at 8°C and 100% humidity for 1 second using a blot force of 4 prior to plunging into liquid ethane. The SP-NK1R-miniG_{s399} and SP6-11-NK1R-mini$G_{s/q70}$ heterotrimeric complexes were frozen under identical blotting conditions at 20 µM and 20.7 µM, respectively.

For the SP-NK1R-mini$G_{s/q70}$ heterotrimeric complex, 3,755 super-resolution movies were recorded with a 300 keV Titan Krios (Thermo Fisher) equipped with a K3 detector and BioQuantum energy filter (Gatan) with a zero-loss energy selection slit width set to 20 eV and a defocus range of -0.8 to -2.0 µm. Each dose-fractionated 120-frame movie was collected at a dose rate of 8.0 $e^{-}pix^{-1}s^{-1}$ for 5.9 seconds at a nominal magnification of 105,000x (physical pixel size of 0.835 Å pix^{-1}) resulting in a cumulative dose of 67 e^{-} $Å^{-2}$. Exposure areas were acquired with automated scripts in a 3x3 image shift collection strategy using SerialEM. The 3878 super-resolution movies of the SP6-11-NK1R-mini$G_{s/q70}$ heterotrimeric complex were acquired with identical acquisition settings on the same 300 keV Titan Krios as previously described.

For the SP-NK1R-miniG_{s399} heterotrimeric complex, 3670 dose-fractionated movies were collected in counting mode with a 300 keV Titan Krios equipped with a K3 detector and BioQuantum energy filter (Gatan) with a zero-loss energy selection slit width set to 20 eV and a defocus range of -0.8 to -2.1 µm. At a dose rate of 24 $e^{-}pix^{-1}s^{-1}$, each 1.52s exposure was

fractionated across 60 frames for a total dose of 49.4 e^{-} $Å^{-2}$. Data were collected using aberration free image shift (AFIS) with EPU 2.10.

Cryo-EM Image Processing

During data collection, movies of the NK1R-mini$G_{s/q70}$ complex were motion corrected and dose weighted with UCSF MotionCor2[39] and binned to physical pixel size. Post-acquisition, micrographs were imported into cryoSPARC[40] for contrast transfer function determination via patch CTF. 7,329,811 particles were template picked with 20 Å low-pass filtered projections of the NK1R-mini$G_{s/q70}$ heterotrimeric complex from a prior screening collection on a 200 keV Talos Arctica. 3,555 micrographs comprising 6,945,760 particles were curated for further processing via CTF fit estimated resolution, ice thickness, and particle pick power scores. Particles were extracted in a 72-pixel box, Fourier cropped from 288 pixels. 200 2D class averages were generated using a maximum alignment resolution of 8 Å, 30 online-EM iterations, and 200 particles per class during each online EM iteration. 1,901,254 particles were selected from qualitatively "good" classes containing any averages that showed "multi-lobed" densities or appeared to be "top" or "bottom" views. Following 2D classification, 500,000 selected particles were used for *ab initio* reconstruction into 3 classes. A single "multi-lobed" class suggestive of an intact NK1R-mini$G_{s/q70}$ heterotrimeric complex was selected and used alongside three poorly aligned "junk" classes generated from *ab initio* volumes from <100 particles. All particles selected from 2D classification as described above were subject to 3D classification with alignment against the NK1R-mini$G_{s/q70}$ and poorly aligned classes from the earlier *ab initio* runs. 718,386 particles in the NK1R complex class were re-extracted without Fourier cropping and subject to the same 3D classification scheme with a new *ab initio* NK1R-mini$G_{s/q70}$ heterotrimeric complex class generated from 300,000 particles and three "junk" classes. Using UCSF pyEM[41], 589,973 particles in the NK1R-mini$G_{s/q70}$ class were exported from cryoSPARC for alignment-free classification in RELION[42] into 4 classes for 50 iterations with a τ parameter of 8. Two

classes containing 122,222 particles were imported into cisTEM[43] for manual "focused" refinements utilizing whole complex and upper-transmembrane domain masks, respectively. To generate local resolution estimates, the NK1R-mini$G_{s/q70}$ complex mask and unfiltered half maps were imported into cryoSPARC. The same half maps and mask were used for directional FSC curve generation, as described in Dang, S. *et al. Nature* 552, 426-429 (2017).

3,670 SP-NK1R-miniG_{s399} movies were motion-corrected post acquisition with UCSF MotionCor2. CTF estimation and template-based automatic particle picking were performed in cryoSPARC. 4,865,341 particles were picked using templates generated from 2D class averages of SP-NK1R-miniG_{s399} as determined from an earlier screening collection. 4,256,322 particles were extracted in an 80 pixel box after curating micrographs via CTF fit estimated resolution, ice thickness, and particle pick power scores. Extracted particles were subject to a round of 3D classification with alignment (Heterogeneous refinement) using a 20Å low-pass filtered initial volume of NK1R-miniG_{s399} and three additional naïve classes generated from a deliberately under-sampled *Ab initio* job. Particles classified into the NK1R-miniG_{s399} class were selected for further workup. This process was repeated over two additional rounds, decreasing particle Fourier cropping at each subsequent extraction round. 561,901 unbinned particles particles classified into the NK1R-miniG_{s399} complex class were then exported to RELION for alignment-free classification on only 7TM domain features for 25 iterations, 4 classes, τ = 8. 288,659 particles in three classes were imported into cisTEM for manual "focused" refinements as in the NK1R-mini$G_{s/q70}$ processing.

3,878 motion-corrected, dose-weighted SP6-11-NK1R-mini$G_{s/q70}$ complex sums were imported into cryoSPARC for CTF estimation and template-based autopicking as previously described. 4,135,538 particles were picked with templates generated from 2D classes determined from a prior screening dataset. Particles were extracted in a 72-pixel box and underwent iterative

rounds of 3D classification with alignment on successively unbinned particles classified into a SP6-11-NK1R-mini$G_{s/q70}$ complex class. 553,506 particles were exported to RELION for alignment-free classification on the 7TM domain using the same parameters as previously described, though with six classes instead of four. Visual inspection of each class led to selection of a single class generated from 59,926 particles for manual "focused" refinements in cisTEM using the same masking scheme as for the previously described complexes. Half maps and masks were re-imported into cryoSPARC for GS-FSC determination. dFSC curve calculation utilized the same half maps and masks from focused refinement.

Model building and refinement: SP-NK1R-mini$G_{s/q70}$

The initial model for NK1R was taken from the high-resolution (2.2 Å) inactive-state structure of NK1R bound to the clinically approved antagonist, netupitant (PDB 6HLP, ref[24]). The model was docked into the 3.0 Å EM density map using manual adjustment and the 'fit in map' function in UCSF ChimeraX[44]. The initial model was manually rebuilt in Coot and refined with both iterative adjustment in Coot and multiple rounds of global minimization and real space refinement using the Phenix.real_space_refine tool in Phenix[45]. In areas of weak sidechain density, residues were capped at the Cβ position to retain sequence information; in areas of weak mainchain density, residues were truncated from the final model. This process was repeated to model the mini$G_{s/q70}$ subunit (starting model miniG_{s399} subunit, PDB 6GDG, ref[21]), $G\beta_1\gamma_2$ (starting model $G\beta_1\gamma_2$ heterodimer, PDB 3SN6, ref[15]), and Nb35 (starting model Nb35, PDB 3SN6, ref[15]). Models were combined into one PDB file in Coot and the model geometry was assessed using Molprobity[46]. Further validation was performed with EMRinger[47] to compare the map to the model. Finally, map-to-model FSCs were calculated in Phenix[45]. All structure figures were prepared with PyMOL (The PyMOL Molecular Graphics System, Version 2.0 Schrödinger, LLC.) or UCSF ChimeraX[44].

To model the Substance P peptide, all peptide residues were manually built into the Substance P EM density in Coot. The resulting Substance P model was refined with iterative adjustment in Coot and multiple rounds of global minimization and real space refinement using the real_space_refine tool in Phenix. Due to weak side chain density, R1 and K3 of the peptide are capped at the Cβ position of the residue. To build the amidated C-terminus of M11, a peptide bond connecting the carbonyl-carbon of M11 to a new nitrogen atom was created in Coot. Bond-lengths, bond-angles, dihedral angles, and planes for the new amide moiety were manually adjusted to reflect the accepted values for amide moieties in protein structures.

Model building and refinement: SP-NK1R-miniG$_{s399}$ & SP6-11-NK1R-miniGs/q70 complexes
The SP-NK1R-miniG$_{s/q70}$ complex model was docked into the 3.1 Å and 3.2 Å EM density maps for the SP-NK1R-miniG$_{s399}$ and SP6-11-NK1R-miniGs/q70, respectively. The models were built and refined as described above. Models were combined into one PDB file in Coot and the model geometry was assessed using Molprobity[46]. Further validation was performed with EMRinger[47] to compare the map to the model. Finally, map-to-model FSCs were calculated in Phenix[45]. All structure figures were prepared with PyMOL (The PyMOL Molecular Graphics System, Version 2.0 Schrödinger, LLC.) or UCSF ChimeraX[44].

Generation of Stable Cell lines and Transfection for signaling assays

Flp-In-HEK293 cells were grown in DMEM supplemented with 5% fetal bovine serum and maintained at 37 °C in a humidified incubator containing 5% CO2. Flp-In-HEK cells were transfected with the pOG44 vector encoding Flp recombinase and the pcDNA5 vector encoding the NK1R at a ratio of 9:1 using lipofectamine as the transfection reagent. Twenty-four hours after transfection, the cells were subcultured and forty-eight hours later, the medium was supplemented with 200 µg/ml Hygromycin B as selection agent, to obtain cells stably expressing the NK1R.

Intracellular Ca^{2+} mobilization signaling assay

Flp-In-HEK293 cells stably expressing human NK1R WT or mutants were plated in Poly-D-Lysine coated 96-well plates. Cells were washed with calcium buffer (10 mM HEPES, 150 mM NaCl, 2.2 mM $CaCl_2$, 1.18 mM $MgCl_2$, 2.6 mM KCl, 10 mM D-glucose, 0.5% w/v BSA, 4 mM probenecid, 0.05% v/v pluronic acid F127; pH 7.4) and then loaded with 1 µM Fura-2 AM ester (Life Technologies) in calcium buffer for 45 min at 37°C. Calcium mobilization was measured using a FlexStation 3 plate reader (Molecular Devices). Fluorescence (excitation: 340 nm and 380 nm; emission: 520 nm) was measured at 4 s intervals for 5 cycles. After establishing baseline fluorescence, cells were stimulated with increasing concentrations of the agonists or 1 µM ionomycin (positive control for normalization, to obtain a receptor-independent response) and the response was measured for 17 cycles in SoftMax Pro (v5.4.4) software. Representative kinetic traces were chosen and show time-dependent Ca^{2+} mobilization after agonist addition. For Ca^{2+} mobilization assays, GraphPad Prism software (v. 9.0) was used to calculate the area under the curve from the kinetic data and for normalization to vehicle and positive control.

cAMP accumulation signaling assay

Flp-In-HEK293 cells stably expressing the human NK1R WT or mutants were seeded at a density of 2,000,000 cells per 10-cm dish and were transfected the following day using polyethylenimine as the transfection reagent. The cells were transfected with 5 µg CAMYEL biosensor (cAMP sensor using YFP-Epac-RLuc), to allow the detection of cAMP levels by Bioluminescence Resonance Energy Transfer. Twenty-four hours after transfection, the cells were plated into Poly-D-Lysine coated 96-well CulturPlates (PerkinElmer) and grown overnight. The cells were equilibrated in Hank's balanced salt solution at 37 °C before starting the experiment. Coelenterazine (Promega) was added at a final concentration of 5 µM at least 3 min before measurement. After establishing a baseline response, cells were stimulated with increasing concentrations of the agonists or 10 µM forskolin (positive control for normalization,

to obtain a receptor-independent response) and the response was measured for a total of 30 min. The signals were detected at 445–505 nm and 505–565 nm using a LUMIstar Omega instrument (BMG LabTech). Representative kinetic traces were chosen and show time-dependent cAMP accumulation after agonist addition. For cAMP accumulation assays, GraphPad Prism software (v. 9.0) was used to calculate the area under the curve from the kinetic data and for normalization to vehicle and positive control.

IP1 accumulation signaling assay

Flp-In-HEK293 cells stably expressing the human NK1R WT or mutants were plated in Poly-D-Lysine coated 96-well plates overnight. Cells were equilibrated in Cisbio Bioassays' IP-One Gq kit stimulation buffer (10 mM HEPES, 146 mM NaCl, 4.2 mM KCl, 0.5 mM $MgCl_2$, 1 mM $CaCl_2$, 5.5 mM D-Glucose, 50 mM LiCl, pH 7.4) for 1 hour prior to agonist stimulation for 1 hour at 37 °C. Cells were then lysed in 25 µl of lysis buffer (50 mM HEPES, 15 mM KF, 1.5% (v/v) Triton-X-100, 3% (v/v) fetal bovine serum, 0.2% (w/v) bovine serum albumin, pH 7.0) and 14 µl of lysis were added to wells of a 384 well white proxiplate (PerkinElmer) for analysis. The Cisbio Bioassays' IP-One competitive immunoassay kit was used to measure myo-Inositol 1 phosphate (IP1) accumulation in cells, based on HTRF® fluorescence resonance energy transfer (FRET) between d2-labeled IP1 (acceptor) and anti-IP1-Cryptate (donor) antibody. These reagents were diluted 1:20 in the lysis buffer and 3 µl of each was added to each well containing the lysates. Lysates were incubated for 1 hour at room temperature before FRET was detected using an Envision plate reader (PerkinElmer). Emission of Lumi4TM-Tb cryptate was detected at 620 nm and emission of d2-conjugated IP1 at 665 nm. Results were calculated from the 665 nm / 620 nm ratio and were normalized to the individual baseline values and the E_{max} of wild-type NK1R with SP in GraphPad Prism software (v. 9.0).

Enzyme-linked immunosorbent assay (ELISA)

Flp-In-HEK293 cells stably expressing human Flag-NK1R WT, mutants, or untransfected as a control were plated into poly-D-lysine–coated 48-well plates and allowed to adhere overnight. Cells were fixed with 3.7% (v/v) paraformaldehyde in tris-buffered saline (TBS) for 30 min. For total expression, cells were permeabilized by 30-min incubation with 0.5% (v/v) NP-40 in TBS. Cells were then incubated in blocking buffer [1% (w/v) skim milk powder in 0.1 M $NaHCO_3$] for 4 hours at room temperature and incubated with mouse M2 anti-FLAG antibody (1:2000, overnight at 4°C). After washing three times with TBS, cells were incubated with anti-mouse horseradish peroxidase–conjugated antibody (1:2000) for 2 hours at room temperature. Cells were washed and stained using the SIGMAFAST OPD substrate (Sigma-Aldrich). Absorbance at 490 nm was measured using an EnVision Multilabel Reader (PerkinElmer). Data were normalized to intact HEK293 cells transfected with NK1R WT.

MiniG protein BRET recruitment assay

HEK293 cells were seeded at a density of 2,000,000 cells per 10 cm dish and were transfected the following day using polyethylenimine as the transfection reagent. Cells were transfected with 1 µg of hNK1R-NLuc and either 4 µg of miniGs-Venus or miniGs/q-Venus, to measure agonist-induced recruitment of the miniG proteins to NK1R with Bioluminescence Resonance Energy Transfer. Twenty-four hours after transfection, the cells were plated into Poly-D-Lysine coated 96-well CulturPlates (PerkinElmer) and grown overnight. The cells were equilibrated in Hank's balanced salt solution at 37 °C before starting the experiment. Furimazine (Promega) was added at a final concentration of 5 µM at least 3 min before measurement. After establishing a baseline response, cells were stimulated with increasing concentrations of agonist and the response was measured for a total of 30 min. The signals were detected at 445–505 nm and 505–565 nm using a LUMIstar Omega instrument (BMG LabTech). Representative kinetic traces were chosen and show time-dependent recruitment of the miniG protein after agonist

addition. For miniG protein recruitment assays, GraphPad Prism software (v. 9.0) was used to calculate the area under the curve from the kinetic data for normalization to vehicle and positive control (10 μM SP).

Quantification and Statistical Analysis

GraphPad Prism software (v. 9.0) was used for signaling data and statistical analysis. Data points are presented as mean ± standard error of the mean (s.e.m.) based on at least 3 biologically independent experiments with the precise number indicated in Supplementary Tables 1, 2 and 3. Data points were normalized to vehicle as 0% and positive control (1 μM ionomycin for Ca^{2+} mobilization, 10 μM forskolin for cAMP accumulation, and the E_{max} of wild-type NK1R with SP for IP1 accumulation) as 100%. Concentration-response curves were fitted using the three parameter log(agonist) vs. response equation. pEC50 values were extracted from the curve fit of each individual experiment. Emax was calculated by subtracting Bottom from Top from the curve fit of each individual experiment. Statistical analysis of pEC50 and Emax values was performed using one-way analysis of variance (ANOVA) with Dunnett's multiple comparison–corrected post hoc test against NK1R WT SP or NK1R WT SP6-11 unless otherwise stated.

Molecular Dynamics: System setup

We performed simulations of NK1R bound to full-length substance P (SP) and a truncated version of SP reduced to the C-terminal residues 6-11 (SP6-11). These simulations were initiated from the cryo-EM structure of SP-bound NK1R, with the intracellular G protein removed and, for SP6-11-bound simulations, residues 1-5 of SP removed.

The peptide-bound NK1R structure was prepared for simulation with Maestro (Schrödinger, LLC). Missing amino acid side chains were modeled using Prime (Schrödinger, LLC). Residues

226–237 are missing in the cryo-EM structure and were not modeled in. Neutral acetyl and methylamide groups were added to cap the N- and C-termini, respectively, of the NK1R protein chains. The N-termini of SP and SP6-11 were prepared in their charged form, while the C-termini were amidated. Titratable residues were kept in their dominant protonation state at pH 7, except for E2.50 (E78) and D3.49 (D129), which were protonated to their neutral form, as studies indicate that these conserved residues are protonated in active class-A GPCRs[48,49]. The hydrogen bond network was optimized in Maestro and verified by visual inspection. Histidine residues were modeled as neutral, with a hydrogen atom bound to either the delta or epsilon nitrogen depending on which tautomeric state optimized the local hydrogen-bonding network. Dowser[50] was used to add water molecules to protein cavities, and the protein structures were aligned on the transmembrane (TM) helices of the inactive NK1R crystal structure (PDB ID 6HLP, ref[24]) in the Orientation of Proteins in Membranes (OPM) database[51]. The aligned structures were inserted into a pre-equilibrated palmitoyloleoyl-phosphatidylcholine (POPC) membrane bilayer using Dabble[52]. Sodium and chloride ions were added to neutralize each system at a concentration of 150 mM. The final systems comprised 57605–58494 atoms, including 134 lipid molecules and 11565–11831 water molecules. Approximate system dimensions were 80 Å x 80 Å x 94 Å.

Molecular Dynamics: Simulation protocols

For each simulation condition (SP-bound and SP6-11–bound), we performed 12 independent simulations (~2 μs each) in which initial atom velocities were assigned randomly and independently. We employed the CHARMM36m force field for protein molecules, the CHARMM36 parameter set for lipid molecules and salt ions, and the associated CHARMM TIP3P model for water[53,54]. Simulations were run using the AMBER18 software[55] under periodic boundary conditions with the Compute Unified Device Architecture (CUDA) version of Particle-Mesh Ewald Molecular Dynamics (PMEMD) on one GPU[56].

After energy minimization, the systems were first heated over 12.5 ps from 0 K to 100 K in the NVT ensemble using a Langevin thermostat with harmonic restraints of 10.0 kcal·mol^{-1}·Å^{-2} on the non-hydrogen atoms of the lipids, protein, and ligand. Initial velocities were sampled from a Boltzmann distribution. The systems were then heated to 310 K over 125 ps in the NPT ensemble. Equilibration was performed at 310 K and 1 bar in the NPT ensemble, with harmonic restraints on the protein and ligand non-hydrogen atoms tapered off by 1.0 kcal·mol^{-1}·Å^{-2} starting at 5.0 kcal·mol^{-1}·Å^{-2} in a stepwise manner every 2 ns for 10 ns, and finally by 0.1 kcal·mol^{-1}·Å^{-2} every 2 ns for an additional 18 ns. All restraints were completely removed during production simulation. Production simulations were performed at 310 K and 1 bar in the NPT ensemble using the Langevin thermostat and Monte Carlo barostat. Lengths of bonds to hydrogen atoms were constrained using SHAKE, and the simulations were performed using a timestep of 4.0 fs while employing hydrogen mass repartitioning[57]. Non-bonded interactions were cut off at 9.0 Å, and long-range electrostatic interactions were calculated using the particle-mesh Ewald (PME) method with an Ewald coefficient (β) of approximately 0.31 Å and B-spline interpolation of order 4. The PME grid size was chosen such that the width of a grid cell was approximately 1 Å.

Molecular Dynamics: Simulation analysis protocols

The AmberTools17 CPPTRAJ package[58] was used to reimage trajectories. Visual Molecular Dynamics (VMD)[59] and PyMOL (The PyMOL Molecular Graphics System, Version 2.0 Schrödinger, LLC.) were used for visualization. MDAnalysis[60] as well as VMD were used for simulation analysis.

Root mean square fluctuation (RMSF) values shown in Figure 4B measure the extent to which a group of atoms fluctuates around its average position in simulation and is thus a measure for mobility. The first 500 ns of each simulation trajectory were omitted from this analysis to avoid

including any initial relaxation of the system in the measurement. The analysis was performed on 1501 frames per simulation, where each frame is separated by 1 ns. For each simulation, an average position of each atom in a specified group (residues 6-11, F7, or M11; for each of these three groups all atoms were included) was calculated. Then, the RMSF was obtained as the time-average of the RMSD to the average structure for each simulation. For the RMSF of residues 6-11, trajectories were aligned to the initial cryo-EM structure on all transmembrane helix Ca atoms. For the RMSF of residues F7 and M11, trajectories were aligned to the initial cryo-EM structure on all Ca atoms of residues 6-11 of SP to better capture the individual residue movement independent of the overall movement of the entire peptide. Each bar in Figure 4 represents the mean RMSF value over all 12 simulations per condition (either SP or SP6-11) and the error bars denote the standard error of the mean. To test statistical significance, we performed two-sided t-tests of unequal variance (Welch's t-tests).

For each of the 3 renderings in Figure 4A and for each of the 3 renderings in Figure 4C, we chose 10 representative simulation frames illustrating the dynamics of the backbone of residues 6-11 and the side chains of F7 and M11.

The fraction of time R177 is in contact with SP or SP6-11 shown in Extended Data Figure 10 was calculated as follows. The first 500 ns of each simulation trajectory were omitted from this analysis to avoid including any initial relaxation of the system in the measurement. The analysis was performed on 1501 frames per simulation, where each frame is separated by 1 ns. We calculated the minimal distance between any atom in R177 and any atom in SP (or SP6-11). If this minimal distance was 3 Å or less, R177 and SP (or SP6-11) were classified to be in contact. Each bar in Extended Data Figure 10 represents the mean value over all 12 simulations per condition (either SP or SP6-11), and the error bars denote the standard error of

the mean. To test statistical significance, we performed a two-sided t-test of unequal variance (Welch's t-test).

Data Availability Statement

All data generated or analyzed during this study are included in this published article and its Supplementary Information. Coordinates for SP-NK1R-mini$G_{s/q70}$, SP-NK1R-miniG_{s399}, and the SP6-11-NK1R-mini$G_{s/q70}$ complex have been deposited in the Protein Data Bank under accession codes 7RMG, 7RMH, 7RMI, respectively. Unsharpened and sharpened electron microscopy density maps and half maps for SP-NK1R-mini$G_{s/q70}$, SP-NK1R-miniG_{s399}, and the SP6-11-NK1R-mini$G_{s/q70}$ complex have been deposited in the Electron Microscopy Data Bank under accession codes 24569, 24570, and 24572, respectively. Final particle stacks for SP-NK1R-mini$G_{s/q70}$, SP-NK1R-miniG_{s399}, and the SP6-11-NK1R-mini$G_{s/q70}$ complex reconstruction have been uploaded to the Electron Microscopy Public Image Archive (EMPIAR) under the accession code 10786. Simulation trajectories for molecular dynamics simulations have been deposited on Zenodo, and are available at https://doi.org/10.5281/zenodo.5113874

1.6 References

1. Steinhoff, M. S., Mentzer, B. von, Geppetti, P., Pothoulakis, C. & Bunnett, N. W. Tachykinins and Their Receptors: Contributions to Physiological Control and the Mechanisms of Disease. *Physiol. Rev.* 94, 265–301 (2014).
2. Hargreaves, R. *et al.* Development of aprepitant, the first neurokinin-1 receptor antagonist for the prevention of chemotherapy-induced nausea and vomiting. *Ann. N. Y. Acad. Sci.* **1222**, 40–48 (2011).
3. Maggi, C. A. The mammalian tachykinin receptors. *Gen. Pharmacol.* **26**, 911–944 (1995).
4. Schwyzer, R. ACTH: A Short Introductory Review. *Ann. N. Y. Acad. Sci.* **297**, 3–26 (1977).
5. Hökfelt, T., Pernow, B. & Wahren, J. Substance P: A Pioneer Amongst Neuropeptides. *J. Intern. Med.* 27–40 (2001).
6. Mazzone, S. B. & Geraghty, D. P. Respiratory actions of tachykinins in the nucleus of the solitary tract: characterization of receptors using selective agonists and antagonists. *Br. J. Pharmacol.* **129**, 1121–1131 (2000).
7. Trafton, J. A., Abbadie, C. & Basbaum, A. I. Differential contribution of substance P and neurokinin A to spinal cord neurokinin-1 receptor signaling in the rat. *J. Neurosci.* **21**, 3656–3664 (2001).
8. Sagan, S., Chassaing, G., Pradier, L. & Lavielle, S. Tachykinin Peptides Affect Differently the Second Messenger Pathways after Binding to CHO Expressed Human NK1 Receptors. *JPET* **276**, 1039–1048 (1996).
9. Riitano, D., Werge, T. M. & Costa, T. A mutation changes ligand selectivity and transmembrane signaling preference of the neurokinin-1 receptor. *J. Biol. Chem.* **272**, 7646–7655 (1997).
10. Evans, T. W., Dixon, C. M., Clarke, B., Conradson, T. B. & Barnes, P. J. Comparison of neurokinin A and substance P on cardiovascular and airway function in man. *Br. J. Clin. Pharmacol.* **25**, 273–275 (1988).

11. Hastrup, H. & Schwartz, T. W. Septide and neurokinin A are high-affinity ligands on the NK-1 receptor: evidence from homologous versus heterologous binding analysis. *FEBS Lett.* **399**, 264–266 (1996).
12. Ciucci, A., Palma, C., Manzini, S. & Werge, T. M. Point mutation increases a form of the NK receptor with high affinity for neurokinin A and B and septide. *British Journal of Pharmacology* **125**, 393–401 (1998).
13. Maggi, C. A. & Schwartz, T. W. The dual nature of the tachykinin NK1 receptor. *Trends Pharmacol. Sci.* **18**, 351–355 (1997).
14. Nehmé, R. *et al.* Mini-G proteins: Novel tools for studying GPCRs in their active conformation. *PLoS One* **12**, e0175642 (2017).
15. Rasmussen, S. G. F. *et al.* Crystal structure of the β2 adrenergic receptor-Gs protein complex. *Nature* **477**, 549–555 (2011).
16. Ballesteros, J. A. & Weinstein, H. Chapter 19: Integrated methods for the construction of three-dimensional models and computational probing of structure-function relations in G protein-coupled receptors. in *Receptor Molecular Biology* (ed. Sealfon, S. C.) 366–428 (Academic Press, 1995).
17. Huang, W. *et al.* Structural insights into μ-opioid receptor activation. *Nature* **524**, 315–321 (2015).
18. Manglik, A. *et al.* Crystal structure of the μ-opioid receptor bound to a morphinan antagonist. *Nature* **485**, 321–326 (2012).
19. Kim, K. *et al.* Structure of a Hallucinogen-Activated Gq-Coupled 5-HT2A Serotonin Receptor. *Cell* **182**, 1574–1588.e19 (2020).
20. Maeda, S., Qu, Q., Robertson, M. J., Skiniotis, G. & Kobilka, B. K. Structures of the M1 and M2 muscarinic acetylcholine receptor/G-protein complexes. *Science* **364**, 552–557 (2019).
21. García-Nafría, J., Lee, Y., Bai, X., Carpenter, B. & Tate, C. G. Cryo-EM structure of the adenosine A2A receptor coupled to an engineered heterotrimeric G protein. *Elife* **7**, (2018).

22. Kato, H. E. *et al.* Conformational transitions of a neurotensin receptor 1-Gi1 complex. *Nature* **572**, 80–85 (2019).

23. Egloff, P. *et al.* Structure of signaling-competent neurotensin receptor 1 obtained by directed evolution in Escherichia coli. *Proc. Natl. Acad. Sci. U. S. A.* **111**, E655–62 (2014).

24. Schöppe, J. *et al.* Crystal structures of the human neurokinin 1 receptor in complex with clinically used antagonists. *Nat. Commun.* **10**, 17 (2019).

25. Valentin-Hansen, L., Frimurer, T. M., Mokrosinski, J., Holliday, N. D. & Schwartz, T. W. Biased Gs versus Gq proteins and β-arrestin signaling in the NK1 receptor determined by interactions in the water hydrogen bond network. *J. Biol. Chem.* **290**, 24495–24508 (2015).

26. Koehl, A. *et al.* Structure of the μ-opioid receptor-Gi protein complex. *Nature* **558**, 547–552 (2018).

27. Hong, C. *et al.* Structures of active-state orexin receptor 2 rationalize peptide and small-molecule agonist recognition and receptor activation. *Nat. Commun.* **12**, 815 (2021).

28. Yin, J. *et al.* Crystal structure of the human NK1 tachykinin receptor. *Proc. Natl. Acad. Sci. U. S. A.* **115**, 13264–13269 (2018).

29. Fong, T. M. *et al.* Mutational analysis of neurokinin receptor function. *Can. J. Physiol. Pharmacol.* **73**, 860–865 (1995).

30. Lane, J. R., May, L. T., Parton, R. G., Sexton, P. M. & Christopoulos, A. A kinetic view of GPCR allostery and biased agonism. *Nat. Chem. Biol.* **13**, 929–937 (2017).

31. Holst, B., Hastrup, H., Raffetseder, U., Martini, L. & Schwartz, T. W. Two active molecular phenotypes of the tachykinin NK1 receptor revealed by G-protein fusions and mutagenesis. *J. Biol. Chem.* **276**, 19793–19799 (2001).

32. Wan, Q. *et al.* Mini G protein probes for active G protein–coupled receptors (GPCRs) in live cells. *J. Biol. Chem.* **293**, 7466–7473 (2018).

33. Nederpelt, I., Bleeker, D., Tuijt, B., IJzerman, A. P. & Heitman, L. H. Kinetic binding and activation profiles of endogenous tachykinins targeting the NK1 receptor. *Biochem. Pharmacol.* **118**, 88–95 (2016).

34. Suomivuori, C.-M. *et al.* Molecular mechanism of biased signaling in a prototypical G protein-coupled receptor. *Science* **367**, 881–887 (2020).

35. Wheatley, M. *et al.* Lifting the lid on GPCRs: the role of extracellular loops. *Br. J. Pharmacol.* **165**, 1688–1703 (2012).

36. Thompson, G. L. *et al.* Biased Agonism of Endogenous Opioid Peptides at the μ-Opioid Receptor. *Mol. Pharmacol.* **88**, 335–346 (2015).

37. Liao, Y. *et al.* Human Neuropeptide S Receptor Is Activated via a Gαq Protein-biased Signaling Cascade by a Human Neuropeptide S Analog Lacking the C-terminal 10 Residues. *J. Biol. Chem.* **291**, 7505–7516 (2016).

38. Kaiser, A., Wanka, L., Ziffert, I. & Beck-Sickinger, A. G. Biased agonists at the human Y1 receptor lead to prolonged membrane residency and extended receptor G protein interaction. *Cell. Mol. Life Sci.* **77**, 4675–4691 (2020).

39. Zheng, S. Q. *et al.* MotionCor2: anisotropic correction of beam-induced motion for improved cryo-electron microscopy. *Nat. Methods* **14**, 331–332 (2017).

40. Punjani, A., Rubinstein, J. L., Fleet, D. J. & Brubaker, M. A. cryoSPARC: algorithms for rapid unsupervised cryo-EM structure determination. *Nat. Methods* **14**, 290–296 (2017).

41. Asarnow, D., Palovcak, E. & Cheng, Y. *asarnow/pyem: UCSF pyem v0.5*. (2019). doi:10.5281/zenodo.3576630.

42. Scheres, S. H. W. RELION: implementation of a Bayesian approach to cryo-EM structure determination. *J. Struct. Biol.* **180**, 519–530 (2012).

43. Grant, T., Rohou, A. & Grigorieff, N. cisTEM, user-friendly software for single-particle image processing. *eLife* vol. 7 (2018).

44. Pettersen, E. F. *et al.* UCSF ChimeraX: Structure visualization for researchers, educators, and developers. *Protein Sci.* **30**, 70–82 (2021).

45. Liebschner, D. *et al.* Macromolecular structure determination using X-rays, neutrons and electrons: recent developments in Phenix. *Acta Crystallogr D Struct Biol* **75**, 861–877 (2019).

46. Williams, C. J. *et al.* MolProbity: More and better reference data for improved all-atom structure validation. *Protein Sci.* **27**, 293–315 (2018).

47. Barad, B. A. *et al.* EMRinger: side chain-directed model and map validation for 3D cryo-electron microscopy. *Nat. Methods* **12**, 943–946 (2015).

48. Ghanouni, P. *et al.* The Effect of pH on β2 Adrenoceptor Function: Evidence for Protonation-Dependent Activation. *J. Biol. Chem.* **275**, 3121–3127 (2000).

49. Ranganathan, A., Dror, R. O. & Carlsson, J. Insights into the role of Asp79(2.50) in β2 adrenergic receptor activation from molecular dynamics simulations. *Biochemistry* **53**, 7283–7296 (2014).

50. Zhang, L. & Hermans, J. Hydrophilicity of Cavities in Proteins. *PROTEINS: Structure, Function, and Genetics* **24**, 433–438 (1996).

51. Lomize, M. A., Lomize, A. L., Pogozheva, I. D. & Mosberg, H. I. OPM: orientations of proteins in membranes database. *Bioinformatics* **22**, 623–625 (2006).

52. Betz, R. M. *Dabble*. (2017). doi:10.5281/zenodo.836914.

53. Huang, J. *et al.* CHARMM36m: an improved force field for folded and intrinsically disordered proteins. *Nat. Methods* **14**, 71–73 (2017).

54. Klauda, J. B. *et al.* Update of the CHARMM all-atom additive force field for lipids: validation on six lipid types. *J. Phys. Chem. B* **114**, 7830–7843 (2010).

55. D.A. Case *et al.* AMBER 2018. *University of California, San Francisco* (2018).

56. Salomon-Ferrer, R. *et al.* Routine microsecond molecular dynamics simulations with AMBER on GPUs. 1. Generalized Born. *J. Chem. Theory Comput.* **8**, 1542–1555 (2012).

57. Hopkins, C. W., Le Grand, S., Walker, R. C. & Roitberg, A. E. Long-Time-Step Molecular Dynamics through Hydrogen Mass Repartitioning. *J. Chem. Theory Comput.* **11**, 1864–1874 (2015).

58. Roe, D. R. & Cheatham, T. E., 3rd. PTRAJ and CPPTRAJ: Software for Processing and Analysis of Molecular Dynamics Trajectory Data. *J. Chem. Theory Comput.* **9**, 3084–3095 (2013).

59. Humphrey, W., Dalke, A. & Schulten, K. VMD: visual molecular dynamics. *J. Mol. Graph.* **14**, 33–8, 27–8 (1996).

60. Michaud-Agrawal, N., Denning, E. J., Woolf, T. B. & Beckstein, O. MDAnalysis: a toolkit for the analysis of molecular dynamics simulations. *J. Comput. Chem.* **32**, 2319–2327 (2011).

1.7 Figures

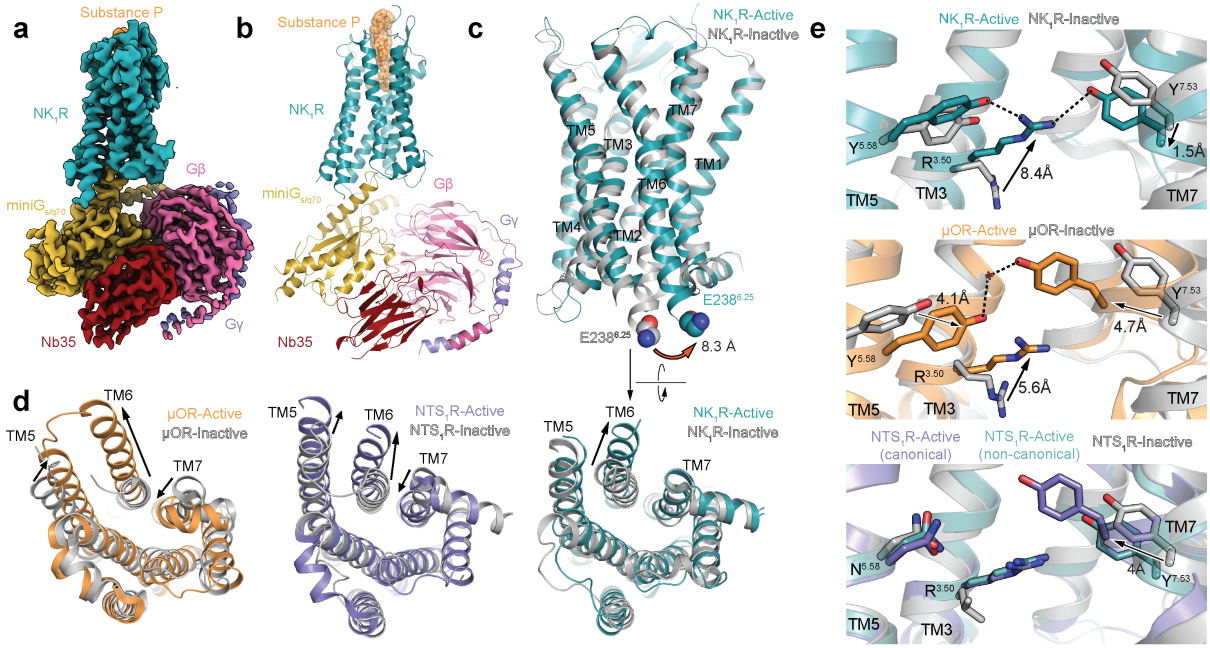

Figure 1.1 Cryo-EM structure of active NK1R bound to SP

(a) Unsharpened cryo-EM map of Substance P-bound NK1R-mini$G_{s/q70}$-Nb35 complex. (b) Ribbon diagram of NK_1R-mini$G_{s/q70}$-Nb35 complex. Substance P is shown as orange spheres. (c) Alignment of active NK_1R with inactive, antagonist-bound NK1R (PDB 6HLP, ref[24]) shows 8.3 Å outward displacement of TM6. (d) Comparison of active NK_1R to other active-state GPCRs shows minimal inward movement of TM7 upon activation. Activation-dependent inward movement of TM7 for two class A neuropeptide GPCRs is shown for comparison: μ-opioid (μOR, active PDB 5C1M, ref[17] and inactive PDB 4DKL, ref[18]) and neurotensin 1 (NTS_1R, active PDB 6OS9, ref[22] and inactive PDB 4BUO, ref[23]). (e) The active-state NK1R NPxxY motif shows a similar conformation to the 'non-canonical' active-state NTS_1R conformation (PDB 6OSA, ref[22]). Inward movement of $Y^{7.53}$ and TM7 for canonically active μOR and NTS_1R is shown for comparison.

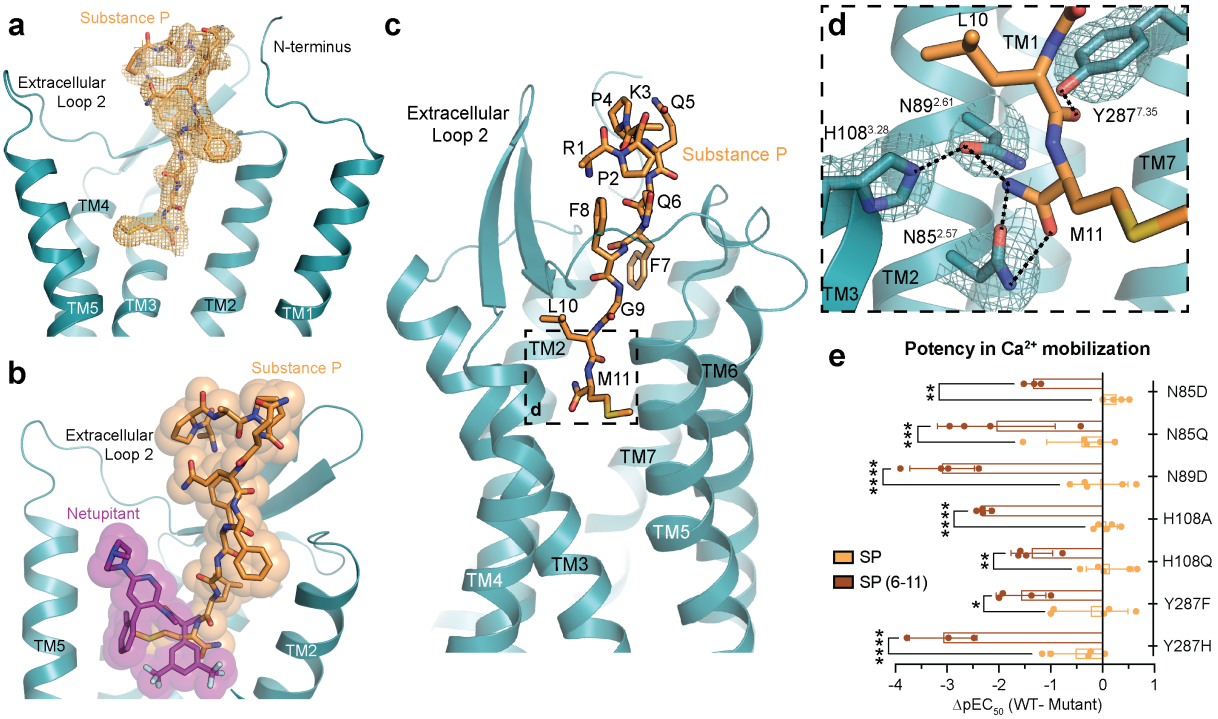

Figure 1.2 Molecular recognition of SP by NK1R
(a) Sharpened cryo-EM density map for Substance P (SP) in the NK1R binding pocket shown as orange mesh and contoured at a distance of 1.85 Å from the placement of Substance P atoms. (b) Overlay of Substance P and netupitant binding sites in NK1R orthosteric site. (c) Substance P forms an extensive interaction interface with NK1R, reaching from the deep orthosteric pocket to the distal extracellular regions. (d) The C-terminally amidated methionine of Substance P (M11) forms an extended hydrogen-bonding network with NK1R. Sharpened cryo-EM density map for sidechains is contoured 1.85 Å away from modeled atoms. (e) Truncated SP6-11 is sensitive to mutations in the deep orthosteric pocket, highlighting the importance of the extended hydrogen-bond network for Substance P recognition. Bar graphs represent mean ΔpEC_{50} (WT - Mutant) ± s.e.m. from n > 3 independently fit biological replicates. Statistical significance between SP and SP6-11 ΔpEC_{50} for each mutant is compared in a two-way analysis of variance (ANOVA) with Šídák's multiple comparison–corrected post hoc test, (* = $p < 0.05$, ** = $p < 0.01$, *** = $p < 0.001$, **** = $p < 0.0001$). Full quantitative parameters from this experiment are listed in Supplementary Table 1.1.

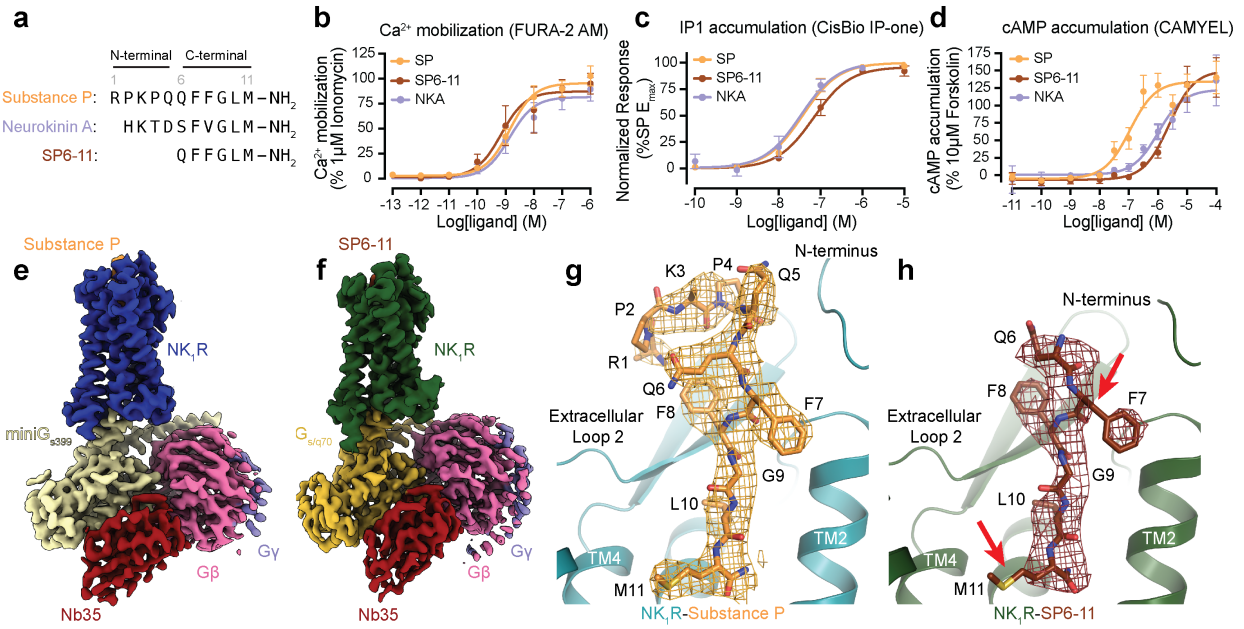

Figure 1.3 Structural interrogation of SP6-11, a G_q-selective tachykinin

(a) Sequence of SP, Substance P 6-11 (SP6-11) and Neurokinin A (NKA). (b,c,d) Ca^{2+}, IP1, and cAMP signaling assays demonstrate that SP6-11 and NKA signal potently through G_q but have lower potency for G_s signaling. Signaling graphs represent the global fit of grouped data ± s.e.m. from n > 3 independent biological replicates. Full quantitative parameters from this experiment are listed in Supplementary Table 1.2. (e) Cryo-EM map of SP-NK1R-miniG_{s399}-Nb35 complex. (f) Cryo-EM map of SP6-11-bound NK1R-mini$G_{s/q70}$-Nb35 complex. (g,h) Unsharpened density maps at equivalent enclosed volume thresholds for SP and SP6-11 are shown as mesh. For SP6-11, density for the M11 side chain is absent, as is connecting density for the F7 side chain (indicated by red arrows). By contrast, these regions are clearly resolved for SP. Density map for the peptide is contoured 2 Å away from modeled atoms.

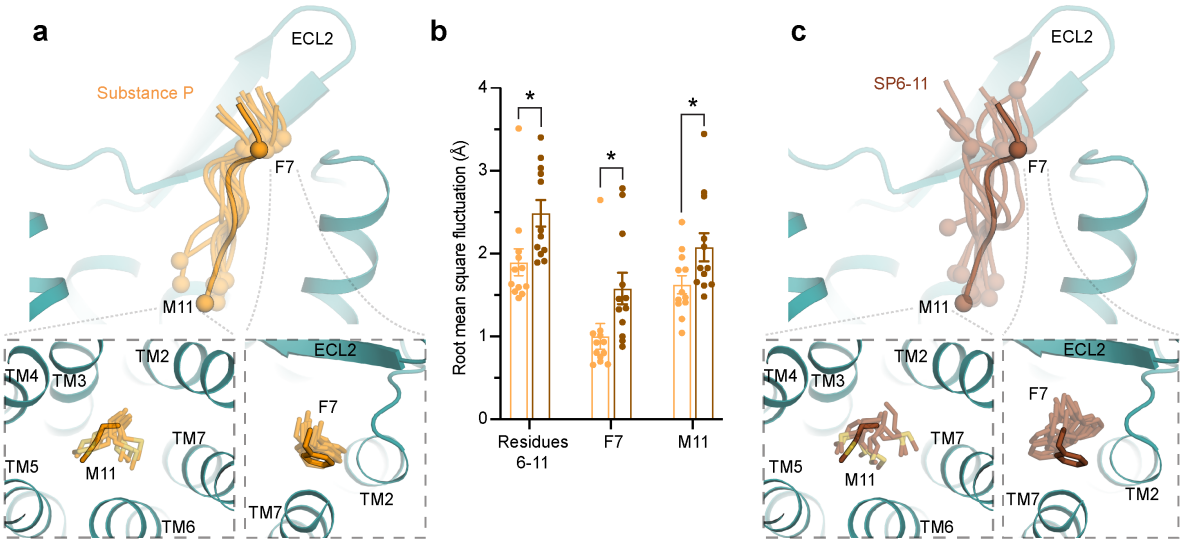

Figure 1.4 Molecular dynamics shows increased motility of SP6-11
(a) Molecular dynamics simulation snapshots for backbone of C-terminal residues of Substance P (SP). Cα atoms for methionine 11 (M11) and phenylalanine 7 (F7) are shown as spheres. The starting cryo-EM structure of SP in the binding pocket is shown with outline; simulation snapshots are transparent. Simulations included all 11 amino-acids of SP, but only residues 6-11 are shown here to enable comparison with SP6-11. Insets show conformations for F7 and M11 side chains of SP. (b) Quantitation of peptide mobility in molecular dynamics simulations as measured by root mean square fluctuation (RMSF). Bar graphs show mean RMSF ± s.e.m. from twelve independent molecular dynamics simulations (* = $p < 0.05$, two-sided Welch's t-test). (c) Simulation snapshots for SP6-11. Insets show alternative conformations for F7 and M11 side chains of SP6-11.

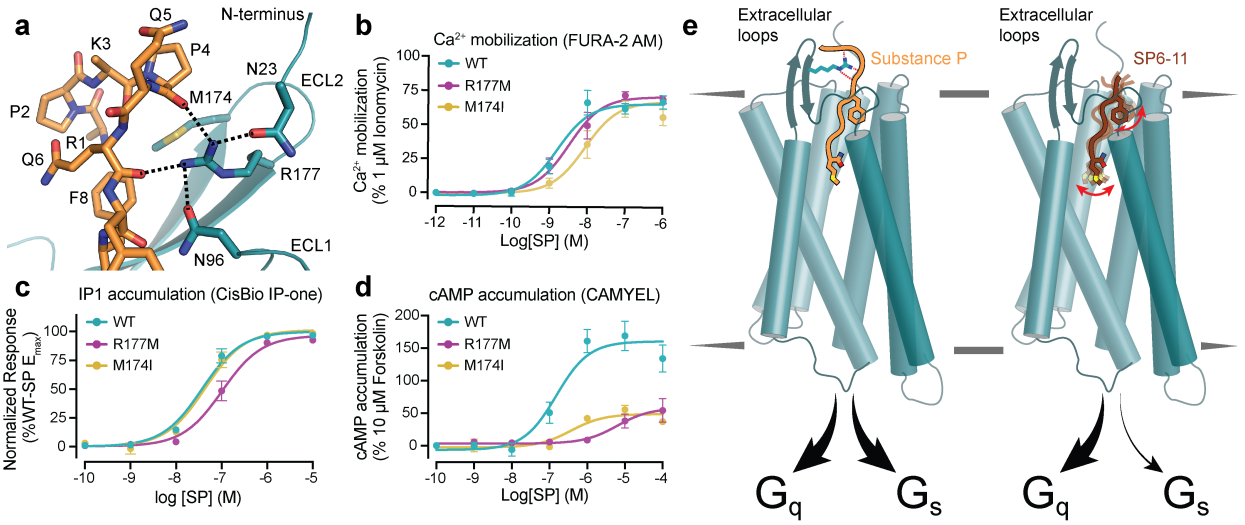

Figure 1.5 Disruption of SP-NK1R ECL2 contacts leads to G_q-selective signaling
(a) NK1R ECL2 contacts with the N-terminal region of SP. R177 engages in an extended hydrogen bonding network with the SP backbone while M174 makes van der Waals contacts with R1 and P4 (b,c,d) Ca^{2+}, IP1, and cAMP signaling assays for point mutants disrupting ECL2-SP interactions. Disruption of SP-NK1R ECL2 contacts leads to G_q selective signaling. Signaling graphs represent the global fit of grouped data ± s.e.m. from n $\geq$ 3 independent biological replicates. Full quantitative parameters from this experiment are listed in Supplementary Table 1.1. (e) Model for tuning of G protein selectivity driven by contacts between SP and ECL2.

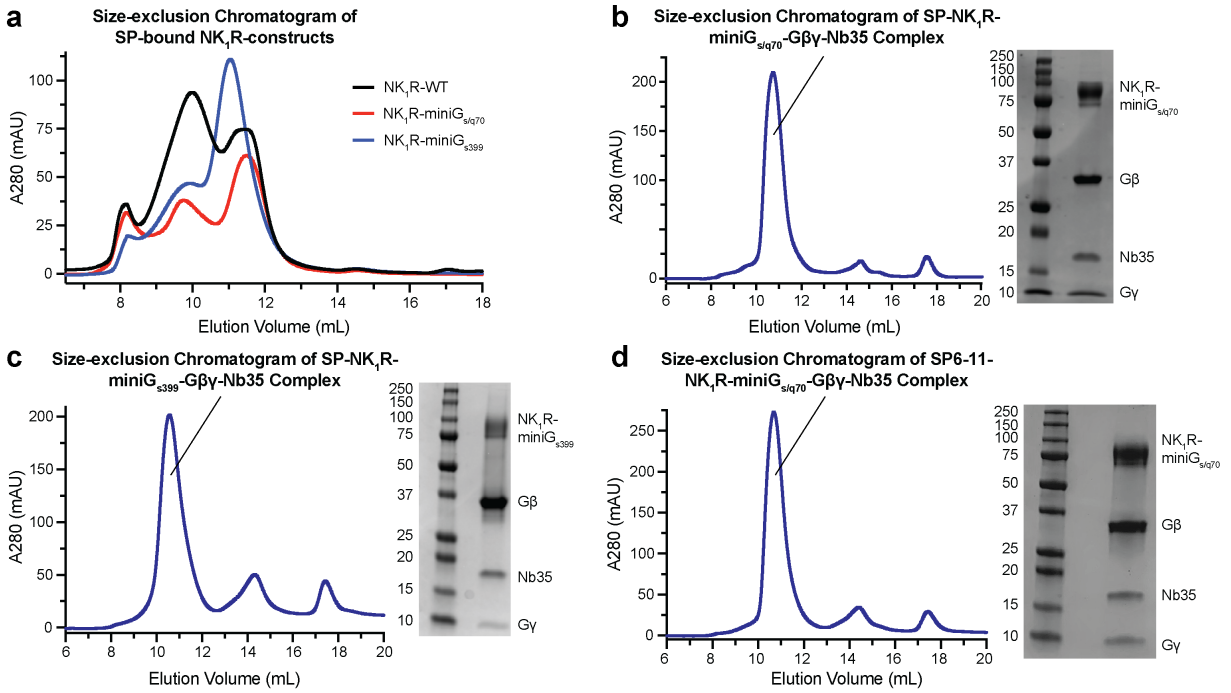

Extended Data Figure 1.1 Biochemistry of active-state NK1R-miniG protein complexes
Size-exclusion chromatography of SP-bound NK1R, NK1R-mini$G_{s/q70}$ and NK1R-miniG_{s399} shows an increase in the fraction of monomeric receptor species for NK1R-miniG fusion proteins. Size-exclusion chromatography traces and SDS-PAGE gels of purified (b) SP-bound NK1R-mini$G_{s/q70}$ complex, (c) SP-bound NK1R-miniG_{s399} complex, and (d) SP6-11-bound NK1R-mini$G_{s/q70}$ complex.

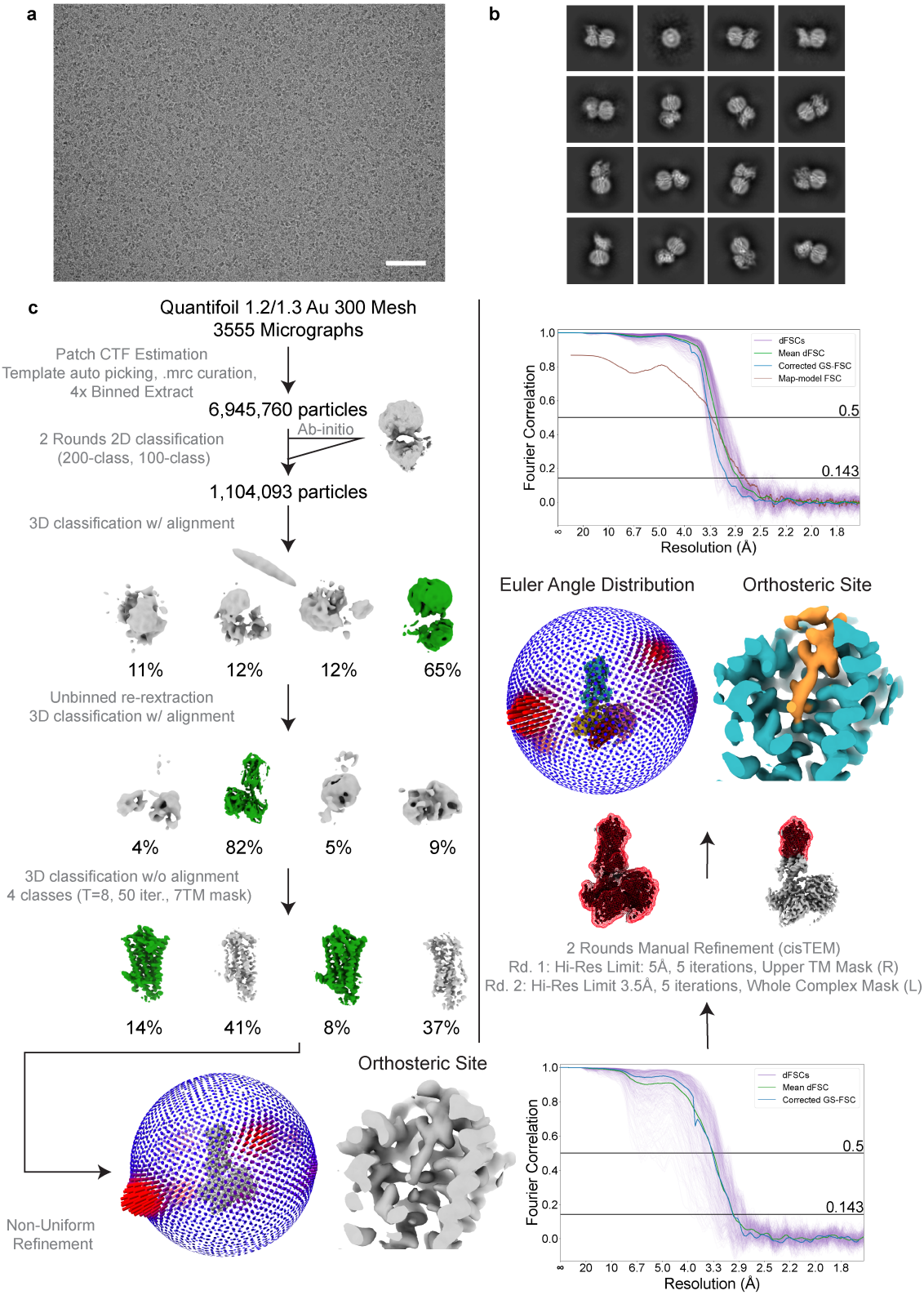

Extended Data Figure 1.2 Cryo-EM data processing workflow for SP-NK1R-mini$G_{s/q70}$ heterotrimeric complex.
(See next page for caption)

Extended Data Figure 1.2 Cryo-EM data processing workflow for SP-NK1R-mini$G_{s/q70}$ heterotrimeric complex

Representative micrograph. Scale bar, 50 nm (a) and 2D-class averages (b) for SP-NK1R-mini$G_{s/q70}$ complex. (c) A flowchart representation of the processing pipeline used for structural determination of the SP-NK1R-mini$G_{s/q70}$ complex. Contrast transfer function (CTF) estimation, 2D classification and all 3D classification jobs with alignment were performed with cryoSPARC. 3D classification without alignment was performed with RELION using a mask encompassing only the receptor transmembrane and final focused refinements were performed with cisTEM. Focused refinement masks are shown as red mesh. Gold-standard fourier shell correlation (GS-FSC) was calculated from a cryoSPARC Local Resolution job using the focused refinement mask encompassing the entire SP-NK1R-mini$G_{s/q70}$ complex. A viewing distribution plot was generated using scripts from the pyEM software suite and visualized in ChimeraX. Directional FSC curves (dFSCs) are shown as purple lines and were determined as previously described in Dang, S. *et al. Nature* 552, 426-429 (2017).

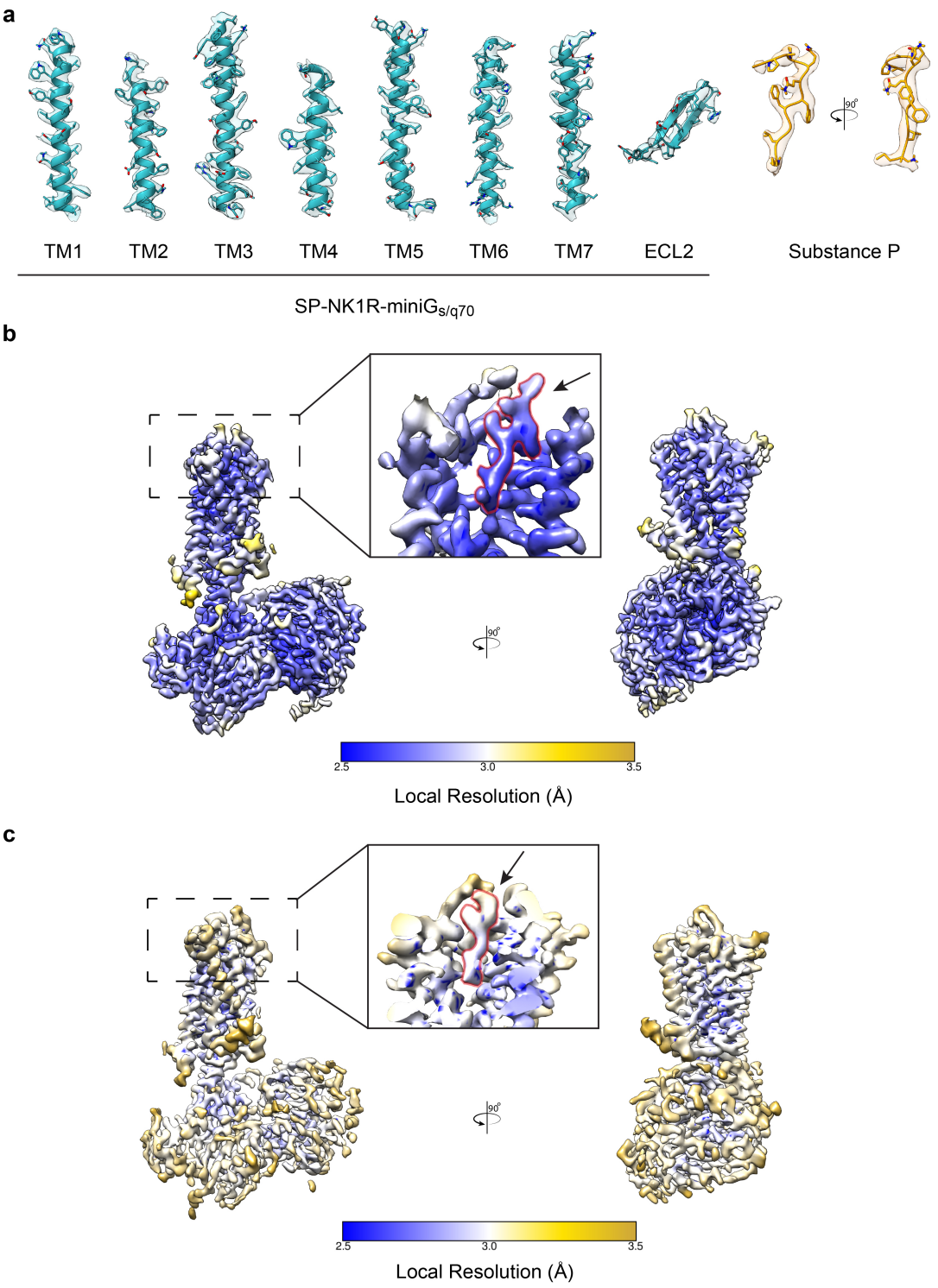

Extended Data Figure 1.3 Cryo-EM density map for NK1R-miniG$_{s/q70}$ heterotrimeric complex

(See next page for caption)

Extended Data Figure 1.3 Cryo-EM density map for NK1R-mini$G_{s/q}$70 heterotrimeric complex

(a) Unsharpened Cryo-EM density map for individual NK1R helices and Substance P density as determined by extending a 2.5 Å radius away from each modeled atom. Local resolution estimation of unsharpened Cryo-EM density maps for (b) SP-NK1R-mini$G_{s/q70}$ and (c) SP6-11-NK1R-mini$G_{s/q70}$ heterotrimeric complex from cryoSPARC. SP and SP6-11 density are highlighted in and shown at equivalent enclosed volume thresholds.

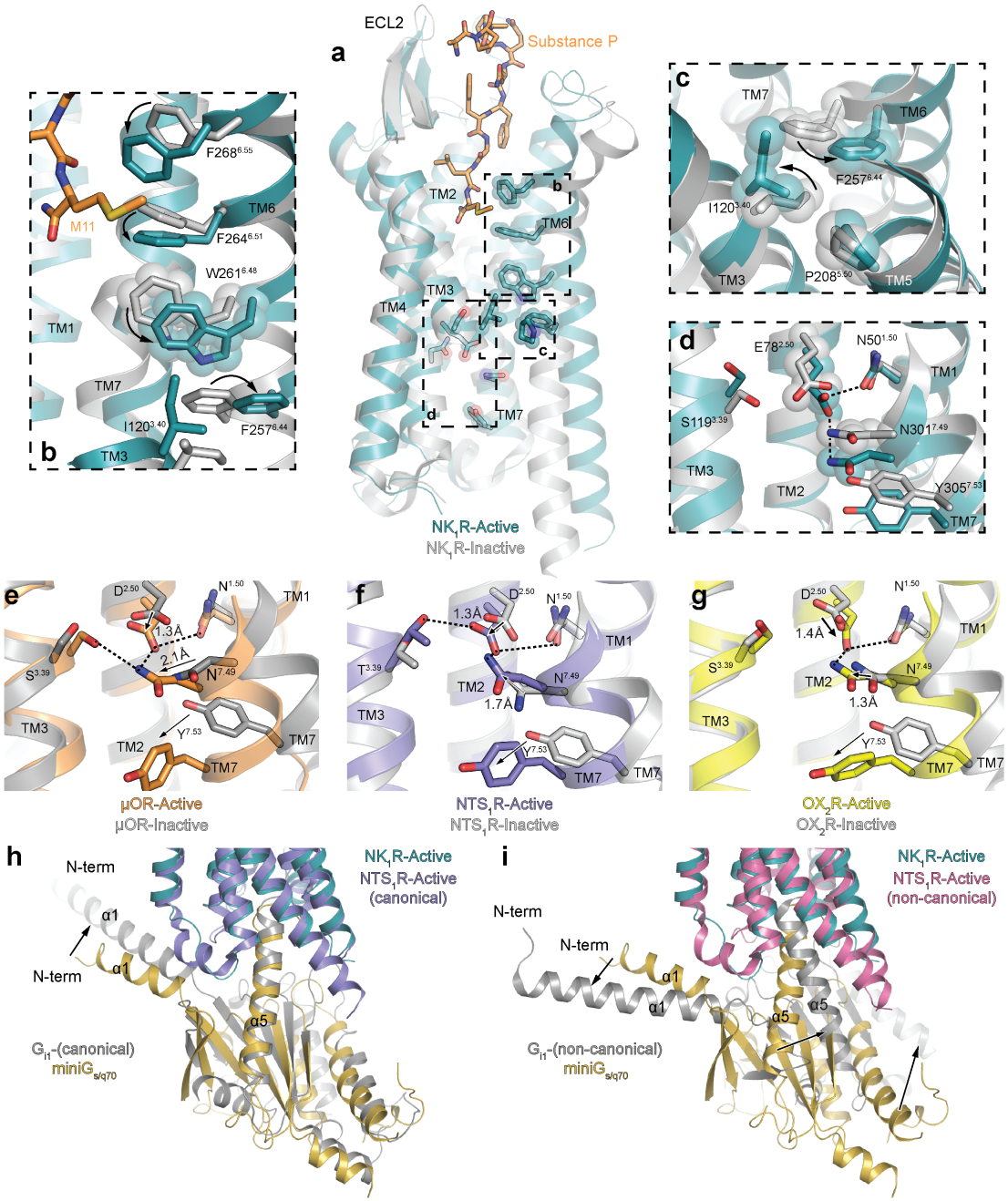

Extended Data Figure 1.4 Structural hallmarks of NK1R activation

(a) Alignment of the SP-NK1R-mini$G_{s/q70}$ structure with an inactive-state NK1R structure (PDB: 6HLP[24]) reveals rearrangement of NK1R structural motifs indicative of class A GPCR activation, including: (b) displacement of the $W^{6.48}$ 'toggle-switch' and (c) rearrangement of the '$P^{5.50}I^{3.40}F^{6.44}$' connector motif. (d) The non-canonical $E78^{2.50}$-$N301^{7.49}$ interaction in NK1R is unchanged between inactive- and active-state structures. We compared the NK1R $E78^{2.50}$-$N301^{7.49}$ interaction to the $D^{2.50}$-$N^{7.49}$ interaction in three class A neuropeptide-binding GPCRs, including: (e) the μ-opioid receptor (Active PDB: 5C1M[17], Inactive PDB: 4DKL[18]), (f) the neurotensin 1 receptor (Active PDB: 6OS9[22], Inactive PDB: 4BUO[23]), and (g) the orexin 2 receptor (Active PDB: 7L1U, Inactive PDB: 5WQC). Alignment of the SP-NK1R-mini$G_{s/q70}$ structure with (h) canonical (PDB: 6OS9[22]) and (i) 'non-canonical' (PDB: 6OSA[22]) active-state NTS_1R reveals that the mini$G_{s/q70}$ protein adopts the canonical G protein coupling orientation.

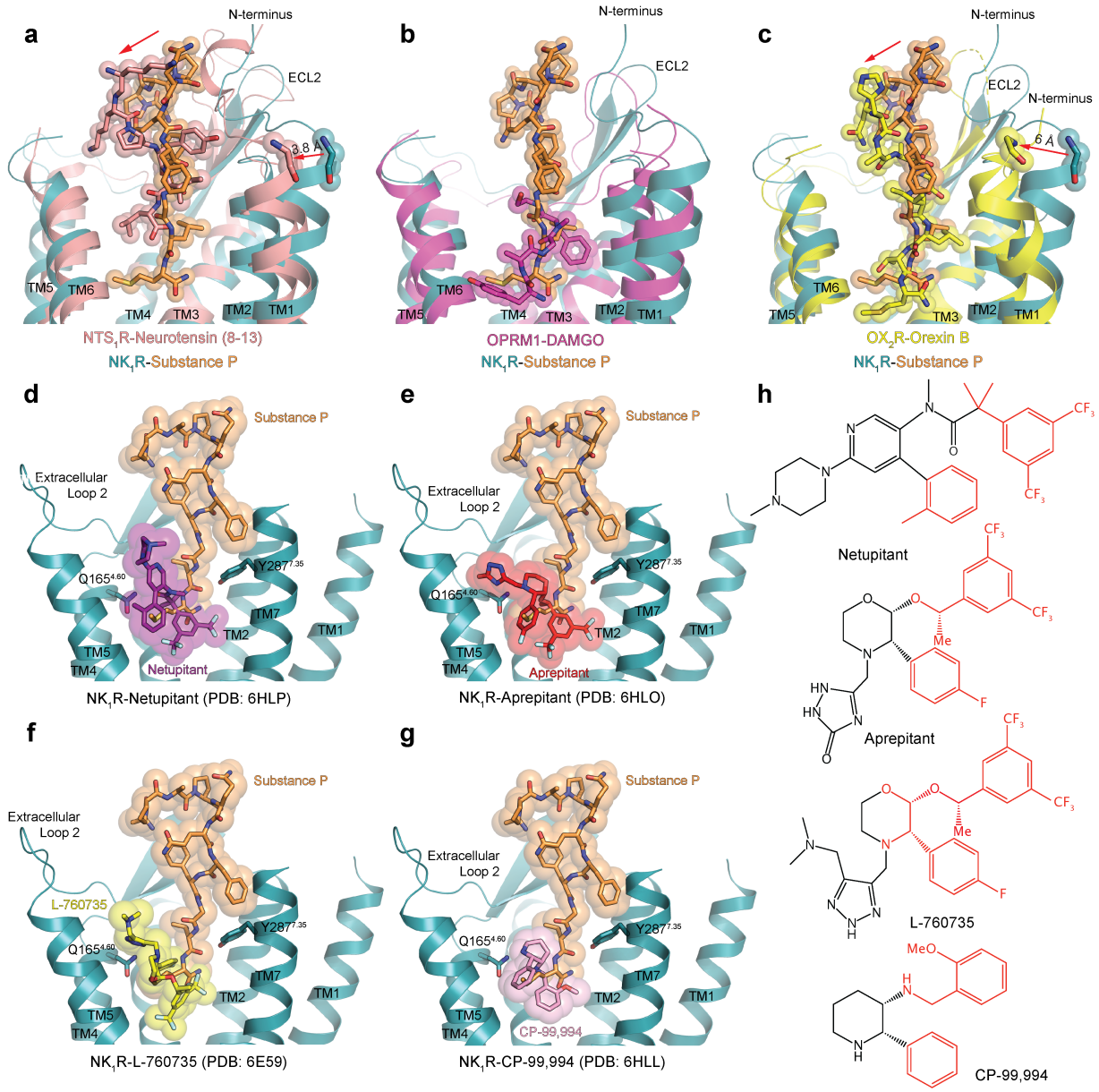

Extended Data Figure 1.5 Comparison of SP-NK1R binding site to related Neuropeptide GPCRs and Inactive-State NK1R Structures

Comparison of SP-bound NK1R-mini$G_{s/q70}$ structure to neuropeptide GPCRs bound to peptidergic ligands, including: (a) the neurotensin 1 receptor bound to neurotensin 8-13 (PDB: 6OS9[22]), (b) the μ-opioid receptor bound to the peptide mimetic agonist DAMGO (PDB: 6DDE[26]), and (c) the orexin 2 receptor bound to orexin B (PDB: 7L1U[27]). Alignment of SP-bound NK1R with inactive-state NK1R structures, including: (d) netupitant-bound (PDB: 6HLP[24]), (e) aprepitant-bound (PDB: 6HLO[24]), (f) L-760,735-bound (PDB: 6E59[28]), and (g) CP-99,994-bound NK1R (PDB: 6HLL[24]). (h) Antagonist chemical structures shown with regions that compete with SP binding site in red.

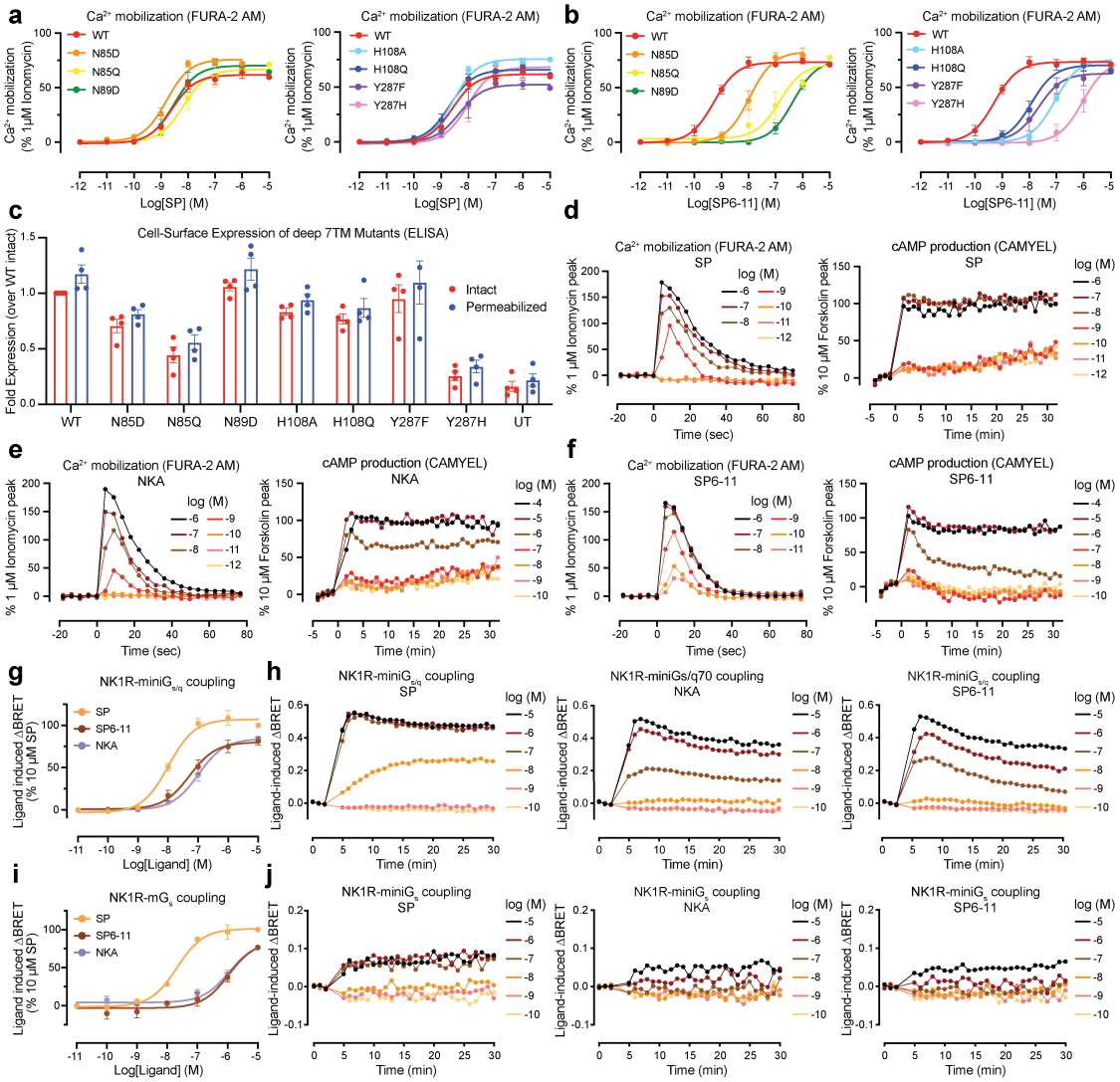

Extended Data Figure 1.6 Signaling studies for NK1R mutations in the deep 7TM region
Ca^{2+} mobilization of wild-type and NK1R mutants after stimulation with (a) SP and (b) SP6-11. Signaling graphs represent the global fit of grouped data ± s.e.m. from n > 3 independent biological replicates. Full quantitative parameters from this experiment are listed in Supplementary Table 1.1. (c) Cell-surface expression of deep 7TM NK1R mutants as determined by ELISA. Untransfected (UT) control shows low ELISA signal. Bar graphs represent mean ± s.e.m. from n = 4 independent biological replicates. Representative kinetic traces of (d) SP (e) NKA, and (f) SP6-11 elicited Ca^{2+} mobilization and cAMP accumulation from n > 3 independent biological replicates. (g) Ligand induced coupling of mini$G_{s/q}$-Venus to hNK1R-RLuc as determined by BRET. Graphs represent the global fit of grouped data ± s.e.m. from n = 3 independent biological replicates. Full quantitative parameters from this experiment are listed in Supplementary Table 1.3. (h) Representative kinetic traces of SP, NKA, and SP6-11 induced recruitment of mini$G_{s/q}$-Venus to hNK1R-RLuc as determined by BRET from n = 3 independent biological replicates. (i) Ligand induced coupling of miniG_s-Venus to hNK1R-RLuc as determined by BRET. Graphs represent the global fit of grouped data ± s.e.m. from n = 3 independent biological replicates. Full quantitative parameters from this experiment are listed in Supplementary Table 1.3. (j) Representative kinetic traces of SP, NKA, and SP6-11 induced recruitment of miniG_s-Venus to hNK1R-RLuc as determined by BRET from n = 3 independent biological replicates.

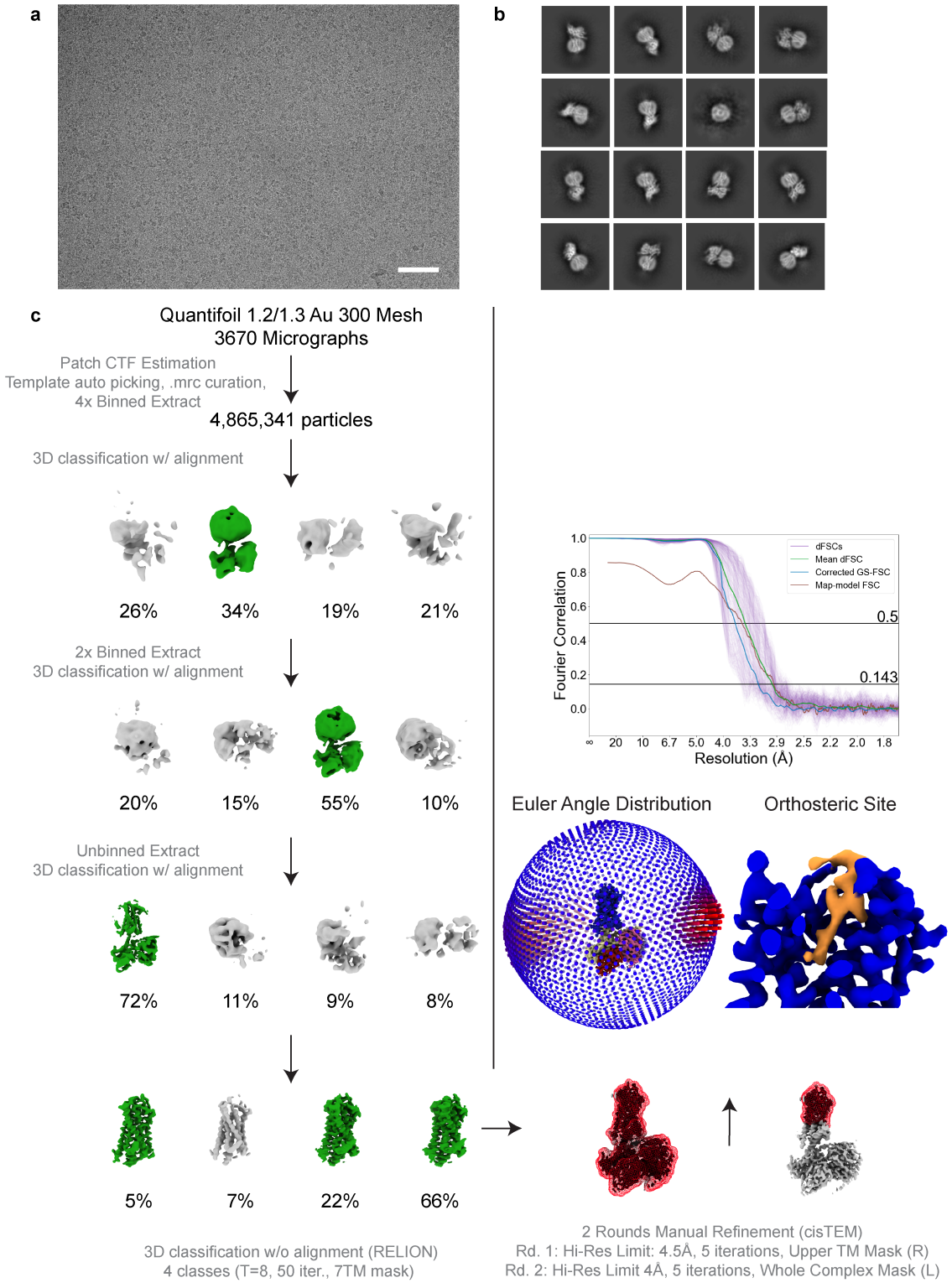

Extended Data Figure 1.7 Cryo-EM data processing for SP-NK1R-miniG$_{s399}$ complex
(See next page for caption)

Extended Data Figure 1.7 Cryo-EM data processing for SP-NK1R-miniG_{s399} complex
Representative micrograph. Scale bar, 50 nm. (a) and 2D-class averages (b) for SP-NK1R-miniG_{s399} complex. (c) A flowchart representation of the processing pipeline used for structural determination of the SP-NK1R-miniG_{s399} complex. CTF Estimation, 2D classification and all 3D classification jobs with alignment were performed with cryoSPARC. 3D classification without alignment was performed with RELION using a mask encompassing only the receptor transmembrane and final focused refinements were performed with cisTEM. Focused refinement masks are shown as red mesh. Gold-standard fourier shell correlation (GS-FSC) was calculated from a cryoSPARC Local Resolution job using the focused refinement mask encompassing the entire SP-NK1R-miniG_{s399} complex. A viewing distribution plot was generated using scripts from the pyEM software suite and visualized in ChimeraX. Directional FSC (dFSC) are shown as purple lines and were determined as previously described in Dang, S. *et al.* *Nature* 552, 426-429 (2017).

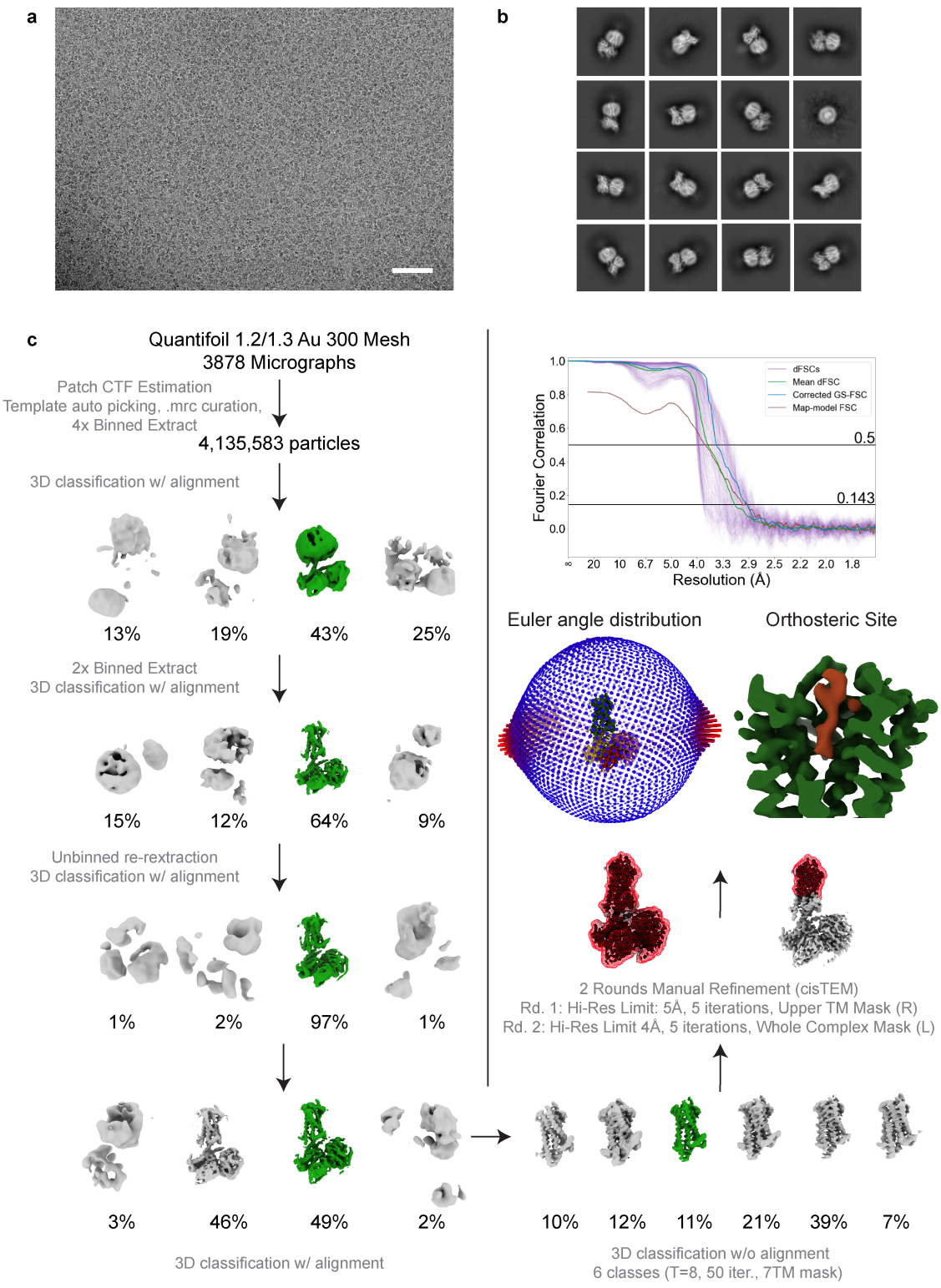

Extended Data Figure 1.8 Cryo-EM data processing for SP6-11-NK1R-miniG$_{s/q70}$ complex
(See next page for caption)

Extended Data Figure 1.8 Cryo-EM data processing for SP6-11-NK1R-mini$G_{s/q70}$ complex
Representative micrograph. Scale bar, 50 nm. (a) and 2D-class averages (b) for SP6-11-NK1R-mini$G_{s/q70}$ complex. (c) A flowchart representation of the processing pipeline used for structural determination of the SP6-11-NK1R-mini$G_{s/q70}$ complex. CTF Estimation, 2D classification and all 3D classification jobs with alignment were performed with cryoSPARC. 3D classification without alignment was performed with RELION using a mask encompassing only the receptor transmembrane and final focused refinements were performed with cisTEM. Focused refinement masks are shown as red mesh. GS-FSC was calculated from a cryoSPARC Local Resolution job using the focused refinement mask encompassing the entire SP6-11-NK1R-mini$G_{s/q70}$ complex. A viewing distribution plot was generated using scripts from the pyEM software suite and visualized in ChimeraX. Directional FSC curves (dFSC) are shown in purple lines and were determined as previously described in Dang, S. *et al. Nature* 552, 426-429 (2017).

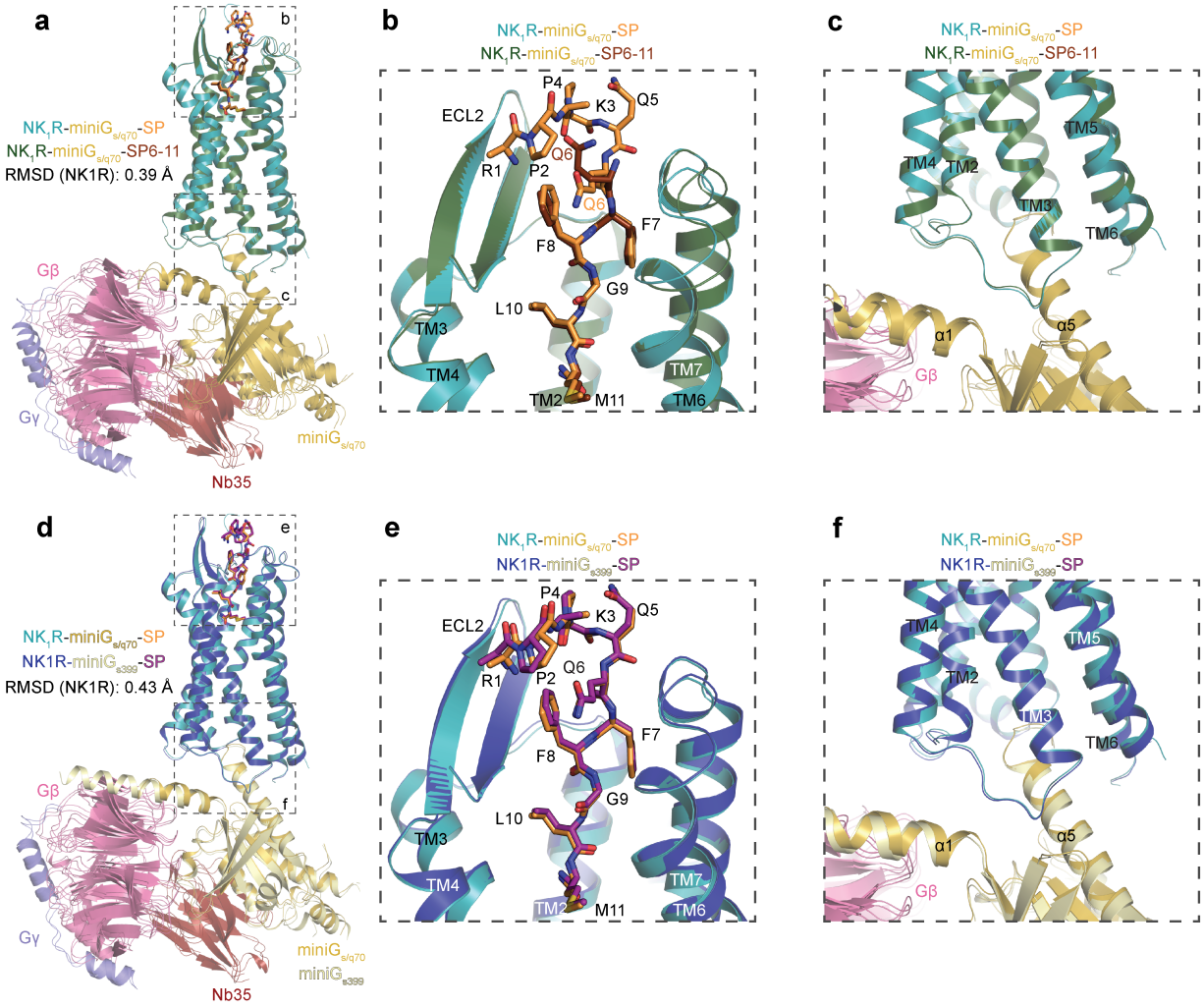

Extended Data Figure 1.9 Comparison of NK1R G protein-complexes
Alignment of SP-NK1R-miniG$_{s/q70}$ and SP6-11-NK1R-miniG$_{s/q70}$ through NK1R 7TM domain reveals minimal changes in (a) overall 7TM architecture, (b) overall peptide binding poses, and (c) insertion of miniG protein α5 helix in NK1R core. Alignment of SP-NK1R-miniG$_{s/q70}$ and SP-NK1R-miniG$_{s399}$ through NK1R 7TM domain reveals minimal changes in (d) overall 7TM architecture, (e) overall Substance P binding pose, and (f) insertion of miniG protein α5 helix in NK1R core.

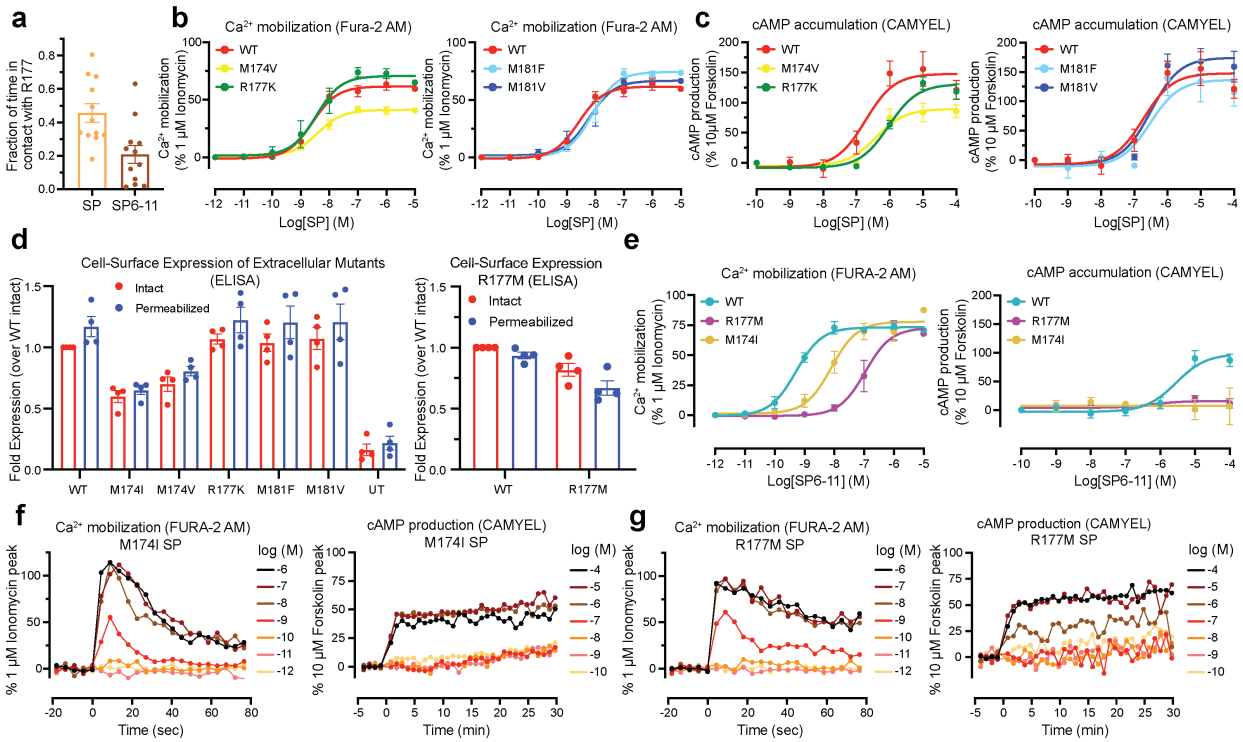

Extended Data Figure 1.10 Signaling studies for NK1R ECL2 mutations

(a) Fraction of time R177 is in contact with SP vs. SP6-11 in molecular dynamics simulations. Bar graphs show mean ± s.e.m from twelve independent molecular dynamics simulations under each condition. SP spent more time in contact with R177 than SP6-11 ($p<0.05$, two-sided Welch's t-test; see Methods). Our simulations are not sufficiently long to guarantee convergence of this quantity. (b) Ca^{2+} mobilization and (c) cAMP accumulation of wild-type and ECL2 NK1R mutants after stimulation with SP. Signaling graphs represent the global fit of grouped data ± s.e.m. from $n > 3$ independent biological replicates. Full quantitative parameters from this experiment are listed in Supplementary Table 1.1. (d) Cell-surface expression of ECL2 NK1R mutants as determined by ELISA. Untransfected (UT) control shows low ELISA signal. Bar graphs represent mean ± s.e.m. from $n = 4$ independent biological replicates. (e) Ca^{2+} mobilization and cAMP accumulation of wild-type, M174I, and R177M NK1R mutants after stimulation with SP6-11. Signaling graphs represent the global fit of grouped data ± s.e.m. from $n > 3$ independent biological replicates. Full quantitative parameters from this experiment are listed in Supplementary Table 1.1. Representative kinetic traces of SP-induced Ca^{2+} mobilization and cAMP accumulation for (f) NK1R M174I and (g) NK1R R177M from $n > 3$ independent biological replicates.

Supplementary Table 1.1 Summary of mutant NK1R signaling studies

Values are expressed as mean pEC_{50} or mean E_{max} ± s.e.m. from (n) independently fit biological replicates. Mean pEC_{50} and E_{max} values for NK1R mutants stimulated with SP are compared in a one-way analysis of variance (ANOVA) with Dunnett's multiple comparison–corrected post hoc test against wild-type NK1R stimulated with SP, (* = $p \leq 0.05$, ** = $p \leq 0.01$, *** = $p \leq 0.001$, **** = $p \leq 0.0001$). Mean pEC_{50} and E_{max} values for NK1R mutants stimulated with SP6-11 are compared in a one-way analysis of variance (ANOVA) with Dunnett's multiple comparison–corrected post hoc test against wild-type NK1R stimulated with SP6-11, (^ = $p \leq 0.05$, ^^ = $p \leq 0.01$, ^^^ = $p \leq 0.001$, ^^^^ = $p \leq 0.0001$). NR, no response. ND, not determined.

	Ligand	Ca^{2+} pEC_{50}	Ca^{2+} E_{max}	cAMP pEC_{50}	cAMP E_{max}	IP1 pEC_{50}	IP1 E_{max}
NK1R WT	SP	8.7 ± 0.1, (9)	72 ± 6, (9)	6.8 ± 0.1, (12)	184 ± 24, (12)	7.4 ± 0.1 (5)	100 ± 3 (5)
	SP6-11	9.4 ± 0.1, (8)	72 ± 4, (8)	5.4 ± 0.5, (12)	106 ± 15, (11)	7.2 ± 0.1 (4)	96 ± 3 (4)
N85D	SP	8.8 ± 0.1, (4)	76 ± 3, (4)	6.4 ± 0.2, (3)	84 ± 16, (3)	ND	ND
	SP6-11	8.0 ± 0.2, (3) ^^	84 ± 6, (3)	NR	NR	ND	ND
N85Q	SP	8.1 ± 0.4, (5)	70 ± 4, (5)	5.9 ± 0.2, (4) *	68 ± 12, (4) *	ND	ND
	SP6-11	7.2 ± 0.5, (4) ^^^^	66 ± 7, (4)	NR	NR	ND	ND
N89D	SP	8.5 ± 0.2, (5)	76 ± 2, (5)	5.0 ± 0.5, (4) ****	141 ± 38, (4)	ND	ND
	SP6-11	6.2 ± 0.2, (4) ^^^^	96 ± 18, (4)	NR	NR	ND	ND
H108A	SP	8.6 ± 0.1, (5)	78 ± 3, (5)	6.1 ± 0.1, (4)	44 ± 6, (4) **	ND	ND
	SP6-11	7.0 ± 0.1, (4) ^^^^	81 ± 3, (4)	NR	NR	ND	ND
H108Q	SP	8.7 ± 0.2, (5)	69 ± 3, (5)	5.3 ± 0.1, (3)	115 ± 14, (3)	ND	ND
	SP6-11	7.9 ± 0.2, (4) ^^^	75 ± 6, (4)	5.3 ± 0.1, (3)	49 ± 5, (3)	ND	ND
Y287F	SP	8.3 ± 0.3, (5)	58 ± 2, (5)	6.3 ± 0.1, (3)	68 ± 13, (3) *	ND	ND
	SP6-11	7.7 ± 0.3, (4) ^^^	61 ± 5, (4)	NR	NR	ND	ND
Y287H	SP	8.0 ± 0.2, (5)	77 ± 3, (5)	5.1 ± 0.2, (3) ****	138 ± 70, (3)	ND	ND
	SP6-11	6.3 ± 0.5, (3) ^^^^	82 ± 19, (3)	NR	NR	ND	ND
M174I	SP	8.2 ± 0.2, (5)	64 ± 7, (5)	6.4 ± 0.1, (3)	55 ± 6, (3) *	7.4 ± 0.1 (5)	101 ± 3 (5)
	SP6-11	8.2 ± 0.2, (4) ^	72 ± 8, (4)	NR	NR	6.7 ± 0.1 (4)	100 ± 3 (4)
M174V	SP	8.5 ± 0.2, (5)	41 ± 2, (5) ****	6.4 ± 0.1, (3)	91 ± 12, (3)	ND	ND
M181V	SP	8.4 ± 0.4, (5)	70 ± 5, (5)	6.5 ± 0.1, (4)	185 ± 21, (4)	ND	ND
M181F	SP	8.2 ± 0.2, (5)	76 ± 5, (5)	6.5 ± 0.1, (3)	150 ± 22, (3)	ND	ND
R177K	SP	8.7 ± 0.3, (6)	76 ± 4, (6)	6.0 ± 0.1, (4) *	149 ± 13, (4)	ND	ND
R177M	SP	8.5 ± 0.2, (9)	75 ± 3, (9)	5.5 ± 0.2, (8) ****	62 ± 22, (8) ***	7.0 ± 0.1 (5) *	97 ± 4 (5)
	SP6-11	6.7 ± 0.3, (4) ^^^^	90 ± 6, (4)	NR	NR	5.9 ± 0.1 (3) ***	104 ± 5 (3)

Supplementary Table 1.2 Summary of tachykinin signaling studies
Values are expressed as mean pEC_{50} or E_{max} ± s.e.m. from (n) independently fit biological replicates. Mean pEC_{50} and E_{max} values for NKA and SP6-11 are compared in a one-way analysis of variance (ANOVA) with Dunnett's multiple comparison–corrected post hoc test against SP represented by * = $p \leq 0.05$, ** = $p \leq 0.01$.

	Ligand	Ca^{2+} pEC_{50}	Ca^{2+} E_{max}	cAMP pEC_{50}	cAMP E_{max}	IP1 pEC_{50}	IP1 E_{max}
NK1R	SP	8.7 ± 0.2 (10)	97 ± 8 (10)	6.9 ± 0.2 (12)	122 ± 11 (12)	7.4 ± 0.1 (5)	100 ± 3 (5)
	NKA	8.7 ± 0.4 (6)	89 ± 10 (6)	6.1 ± 0.1 (7) *	111 ± 11 (7)	7.5 ± 0.2 (3)	100 ± 6 (3)
	SP6-11	8.9 ± 0.5 (4)	96 ± 8 (4)	5.7 ± 0.1 (4) **	129 ± 17 (4)	7.2 ± 0.1 (4)	96 ± 3 (4)

Supplementary Table 1.3 Summary of miniG protein BRET recruitment studies
Values are expressed as mean pEC_{50} or mean E_{max} ± s.e.m. from (n) independently fit biological replicates.

	Ligand	pEC_{50}	E_{max}
$MiniG_{s/q}$	SP	8.0 ± 0.1 (3)	110 ± 5 (3)
	NKA	7.0 ± 0.1 (3)	85 ± 1 (3)
	SP6-11	7.3 ± 0.2 (3)	80 ± 3 (3)
$MiniG_s$	SP	7.7 ± 0 (3)	103 ± 5 (3)
	NKA	5.9 ± 0.2 (3)	83 ± 5 (3)
	SP6-11	6.0 ± 0.2 (3)	89 ± 7 (3)

Supplementary Table 1.4 Cryo-EM data collection, refinement and validation statistics

	SP-NK1R-miniG$_{s/q70}$ (EMDB-24569) (PDB 7RMG)	SP6-11-NK1R-miniG$_{s/q70}$ (EMDB-24570) (PDB 7RMH)	SP-NK1R-miniG$_{s399}$ (EMDB-24572) (PDB 7RMI)
Data collection and processing			
Magnification	105,000	105,000	105,000
Voltage (kV)	300	300	300
Electron exposure (e–/Å^2)	67	67	49
Defocus range (μm)	-0.8 to -2.0	-0.8 to -2.0	-0.8 to -2.1
Pixel size (Å)	0.835 (physical)	0.835 (physical)	0.860 (physical)
Symmetry imposed	*C1*	*C1*	*C1*
Initial particle images (no.)	6,945,760	4,135,583	4,865,341
Final particle images (no.)	122,220	59,926	288,659
Map resolution (Å)	3.0 (masked)	3.2 (masked)	3.1 (masked)
FSC threshold	0.143	0.143	0.143
Map resolution range (Å)	2.5-3.5	2.7-3.8	2.6-4.4
Refinement			
Initial model used (PDB code)	6HLP, 6GDG, 3SN6	SP-NK1R-miniG$_{s/q70}$	SP-NK1R-miniG$_{s/q70}$
Model resolution (Å)	3.4/3.2 (unmasked/masked)	3.9/3.7 (unmasked/masked)	3.6/3.3 (unmasked/masked)
FSC threshold	0.5	0.5	0.5
Model resolution range (Å)	3.2-50	3.7-50	3.3-50
Map sharpening *B* factor (Å^2)	Unsharpened or -87	Unsharpened or -80	Unsharpened or -120
Model composition			
Non-hydrogen atoms	7316	7202	7434
Protein residues	968	960	986
Ligands	N: 1	N: 1	N: 1
B factors (Å^2)			
Protein	35.99	50.1	74.3
Ligand	30.0	29.3	57.3
R.m.s. deviations			
Bond lengths (Å)	0.004	0.004	0.004
Bond angles (°)	0.815	0.842	0.746
Validation			
MolProbity score	1.27	1.43	1.31
Clashscore	3.58	4.29	2.49
Poor rotamers (%)	0	0	0
EM ringer score	4.52	2.73	3.42
CaBLAM outliers (%)	1.31	1.87	1.72
Ramachandran plot			
Favored (%)	97.35	96.57	95.93
Allowed (%)	2.65	3.43	4.07
Disallowed (%)	0	0	0

Chapter 2: Leveraging conformation heterogeneity in oncogenic $G\alpha_q$ isoforms for uveal melanoma therapy

This chapter contains unpublished results from a manuscript in preparation for submission written by Harris, J.A., Born, A., Kenanova, D., Powers, A.S., Jaimes Santiago, L., Olivares Rojas, A., Dror, R.O., Arkin, M., and Manglik, A.

Harris, J.A., Born, A. and Kenanova, D. contributed equally to this work.

Author contributions: Harris, J.A. generated all $G\alpha_q$ DNA constructs, created all $G\alpha_q$ Expi293 stable cell lines, established biochemical approaches to reconstitute wild-type and oncogenic $G\alpha_q$ mutants, purified wild-type and oncogenic $G\alpha_q$ mutants, and performed fluorescence polarization experiments. Born, A.B. purified wild-type and oncogenic $G\alpha_q$ mutants, acquired NMR spectra and analyzed NMR spectra. Kenanova, D. performed all disulfide tethering screens and follow-up compound validation LC/MS assays under the guidance of Arkin, M. Harris, J.A. and Olivares Rojas, A. assisted with follow-up compound validation LC/MS assays. Jaimes Santiago, L. and Born, A.B. assisted with fluorescence polarization experiments. Powers, A.S. performed and analyzed molecular dynamics simulations under the guidance of Dror, R.O. The text was written by Harris, J.A., Born, A., Kenanova, D. and Manglik, A. The overall project was supervised by Manglik, A.

2.1 Abstract

Uveal melanoma is a rare and intractable cancer driven by acquired somatic mutations in $G\alpha_{q/11}$. Q209 mutations cause deficient $G\alpha_{q/11}$-mediated GTP hydrolysis and promote oncogenic signaling. No therapeutics directly target $G\alpha_{q/11}$ mutants in cancer. Using NMR and molecular dynamics simulations, we show oncogenic Q209 mutations increase SwII flexibility and conformational heterogeneity. SwII conformational differences enable discovery of oncogene-selective disulfide-containing fragments. Covalent fragment tethering to SwII prevents binding of $G\alpha_{q/11}$ effector-derived peptides. Directly targeting oncogenic Q209 mutants shows promise for treatment of uveal melanoma and may be broadly generalizable for mutant Gα proteins in cancer.

2.2 Introduction

Uveal melanoma is a rare but deadly intraocular cancer, accounting for ~5% of all diagnosed melanomas and affecting ~7,000 individuals each year[1–3]. Primary uveal melanoma is well-controlled with surgery or radiation therapy and the five-year survival rate (80%) is favorable[4]. However, 50% of primary uveal melanomas metastasize[5]. There is no proven standard of care treatment for metastatic uveal melanoma and overall survival rates (4-15 months) have not improved in the past forty years [4–7]. Systemic and metastasis-directed chemotherapies do not offer long-term control of disease progression[6,7]. Immunotherapy has shown great success in improving survival rates in metastatic cutaneous melanomas; yet, these approaches have shown minimal efficacy in treating metastatic uveal melanoma[7]. A notable exception to this trend is tebentafusp, a T-cell-redirecting bi-specific immunologic that was recently shown to improve overall survival rates in metastatic uveal melanoma[8]. Nevertheless, uveal melanoma is a rare and devastating disease with clear unmet clinical need.

The molecular pathology of uveal melanoma is distinct from cutaneous melanomas, which are primarily driven by acquired somatic mutations in BRAF and NRAS[9,10]. In contrast, ~85% of all uveal melanomas contain oncogenic driver mutations in the $G\alpha_{q/11}$ family of Gα proteins[11,12]. Gα proteins contain a Ras-like GTPase domain that couples guanine nucleotide exchange to orchestrated signal transduction after activation by G protein-coupled receptors (GPCRs)[13]. More than 90% of acquired somatic mutations in $G\alpha_{q/11}$ occur at Q209[2], a key residue in Gα-mediated GTP hydrolysis[14,15]. Oncogenic Q209 $G\alpha_{q/11}$ mutants possess diminished capacity to hydrolyze GTP[16], thereby preventing inactivation of $G\alpha_{q/11}$ and constitutively activating $G\alpha_{q/11}$ signaling in a GPCR-independent mechanism[1,2]. Prolonged GTP occupancy of oncogenic $G\alpha_{q/11}$ mutants drives sustained interactions with $G\alpha_{q/11}$ effector proteins, leading to oncogenic signaling via mitogen activated protein kinase[11,12,16] (MAPK) and yes-associated protein[17–19] (YAP) pathways. Indeed, the relatively small number of uveal melanomas that do not harbor

oncogenic $G\alpha_{q/11}$ mutations possess mutually exclusive mutations in cysteinyl leukotriene receptor 2[20], a $G\alpha_{q/11}$-coupled GPCR in melanocytes, or phospholipase C β_4[21], a downstream $G\alpha_{q/11}$ effector. Mutational burdens in uveal melanoma clearly demonstrate that oncogenic transformation requires activation of $G\alpha_{q/11}$-mediated signaling pathways. Yet, there are currently no therapeutics that directly target oncogenic Q209 $G\alpha_{q/11}$ mutants in cancer, owing to the presumed structural similarity between wild-type and oncogenic GTP-bound $G\alpha_{q/11}$[1,2].

Intriguingly, recent biochemical efforts to characterize mutant $G\alpha_q$ function revealed that oncogenic Q209 $G\alpha_q$ mutants show differential patterns of $G\alpha_q$ effector protein engagement[16]. This observation implies that oncogenic Q209 $G\alpha_q$ mutants may access novel protein conformations compared to wild-type $G\alpha_q$. Exploiting conformational differences to selectively target oncogenic Q209 $G\alpha_q$ mutants is a promising therapeutic strategy, as direct inhibition of oncogenic $G\alpha_q$ signaling powerfully arrests uveal melanoma progression. Indeed, genetic knockdown of Q209L $G\alpha_q$ reduces MAPK signaling in uveal melanoma-derived cell lines[11,17] and inhibits tumor formation in mouse xenograft models[19] Similarly, YM-254890[22,23] and FR900359[24], two cyclic depsipeptides that directly inhibit $G\alpha_{q/11}$, diminish pro-tumorigenic signaling in uveal melanoma-derived cell lines[25] and halt tumor progression mouse xenograft models[26,27]. The cross-reactivity of YM-254890 and FR900359 with wild-type $G\alpha_{q/11}$ proteins, however, poses significant cardiovascular and hemostatic concerns and limits their clinical utility. Nevertheless, direct inhibition of oncogenic Q209 $G\alpha_q$ mutants—either by genetic knockdown or small molecule perturbation—shows promise in blunting uveal melanoma progression.

Here, we report our efforts to characterize the conformational landscape of oncogenic Q209 $G\alpha_q$ mutants using NMR and molecular dynamics simulations. Key insights gained from dynamic structure–function analysis of oncogenic Q209 $G\alpha_q$ mutants enabled the discovery of wild-type

sparing small molecule $G\alpha_q$ inhibitors. While preliminary, these molecules are leads towards the development of oncogene-selective $G\alpha_q$ inhibitors as uveal melanoma therapeutics.

2.3 Results

SwII conformational heterogeneity in oncogenic $G\alpha_q$ isoforms

Oncogenic Q209 mutations are found at the base SwII, a conformationally flexible α-helix that forms a key binding interface with $G\alpha_q$ effector proteins (Figure 2.1a). We hypothesized that differences in the SwII conformational landscape between wild-type (WT) and oncogenic Q209 $G\alpha_q$ mutants may explain their differential engagement of $G\alpha_q$ effector proteins[16]. To test this hypothesis, we first engineered a lipidation-free $G\alpha_q$ construct by mutagenizing two endogenously palmitoylated cysteines in the N-terminal α-helix to alanine (C9A, C10A). This enabled monodisperse reconstitution of GDP-bound WT, Q209L and Q209P $G\alpha_q$ ($G\alpha_q$-GDP) without detergent (Extended Data Figure 2.1). We then used a site-specific ^{13}C-labeling approach[28] to study conformational differences in SwII between WT and oncogenic $G\alpha_q$ isoforms with NMR.

Purified $G\alpha_q$-GDP was incubated with a cysteine-reactive s-methyl-^{13}C methanethiosulfonate (^{13}C-MMTS) probe and excess unreacted label was removed with size-exclusion chromatography (Figure 2.1b, Extended Data Figure 2.1). We then collected ^{1}H–^{13}C-heteronuclear single quantum coherence (HSQC) NMR spectra of WT, Q209L, and Q209P $G\alpha_q$-GDP. We observed two HSQC peaks corresponding to ^{13}C-labeled $G\alpha_q$-GDP and we assigned the C219 peak in SwII ($\omega^{13}C$, $\omega^{1}H$) = (2.22 ppm, 25.3 ppm) via mutagenesis (Figure 2.1c,d,e, Extended Data Figure 2.1). The SwII C219 peak between WT, Q209L, and Q209P $G\alpha_q$-GDP spectra appeared largely similar and overlapping. Notably, we did observe peak broadening of the Q209L $G\alpha_q$-GDP C219 peak, likely indicative of the presence of two GDP-bound Q209L populations.

As the $G\alpha_q$-GTP state is the physiologically relevant conformation for interacting with effector proteins, we sought to characterize the conformational landscape of SwII when bound to GTP.

$G\alpha_q$ undergoes atypically slow nucleotide exchange[29], allowing us to visualize GDP dissociation and association of a slowly hydrolyzable GTP mimetic, guanosine 5'-O-[gamma-thio]triphosphate (GTPγS), with NMR. We collected HSQC spectra every hour for 14 hours after addition of Mg^{2+} and excess GTPγS. In the WT $G\alpha_q$ spectra, we observed our C219 peak in slow-exchange with a new downfield peak ($\omega^{13}C$, $\omega^{1}H$) = (2.35 ppm, 26.1 ppm) after addition of GTPγS (Figure 2.1b). After 8 hours, we saw full conversion of the C219 signal to the downfield peak. We assigned these two C219 peaks ($\omega^{13}C$, $\omega^{1}H$) = (2.22 ppm, 25.3 ppm) and ($\omega^{13}C$, $\omega^{1}H$) = (2.35 ppm, 26.1 ppm) as $G\alpha_q$-GDP and $G\alpha_q$-GTPγS states, respectively. Prior structures of $G\alpha_q$ show large-scale conformational change of SwII and C219 between GDP- and GTP-bound conformations[23,30] (Figure 2.1a). This is in good agreement with our NMR spectra, which show the SwII C219 chemical environment changing upon guanine nucleotide exchange.

In sharp contrast to the WT $G\alpha_q$-GTPγS spectra, the Q209L and Q209P spectra showed greater conformational heterogeneity of SwII after addition of GTPγS. For Q209L, we observed a full transition of the C219 peak to a downfield $G\alpha_q$-GTPγS state ($\omega^{13}C$, $\omega^{1}H$) = (2.35 ppm, 26.0 ppm) after 8 hours (Figure 2.1d). However, we observed peak broadening of the Q209L $G\alpha_q$-GTPγS C219 peak likely indicative of two GTPγS-bound populations and similar to what we observed in the Q209L $G\alpha_q$-GDP spectra. We were unable to observe a full transition of the Q209P C219 peak to a downfield $G\alpha_q$-GTPγS state ($\omega^{13}C$, $\omega^{1}H$) = (2.32 ppm, 25.6 ppm) even after 14 hours (Figure 2.1e, Extended Data Figure 2.1). Instead, we observed several weak peaks, likely corresponding to a mixture of $G\alpha_q$-GDP and $G\alpha_q$-GTPγS states. Similarly to Q209L, we observed significant peak broadening of the Q209P C219 signal after addition of GTPγS, likely reflecting the presence of multiple populations within both GDP- and GTPγS-bound states. Overall, SwII of Q209L and Q209P $G\alpha_q$-GTPγS experiences greater conformational heterogeneity than WT $G\alpha_q$-GTPγS.

Prior crystal structures of $G\alpha_q$ bound to a GTP mimetic, guanosine diphosphate aluminum (IV) fluoride (GDP-AlF_4) show direct, stabilizing contacts between SwII Q209 and the phosphate tail of the guanine nucleotide[31–33]. Further, oncogenic Q209 $G\alpha_q$ mutants cannot hydrolyze GTP as efficiently as WT $G\alpha_q$ *in vitro*[16]. We therefore hypothesized that oncogenic Q209 $G\alpha_q$ mutants cannot form stabilizing interactions between Q209 and GTP, likely contributing to increased conformational heterogeneity of SwII we observed in our Q209L and Q209P $G\alpha_q$-GTPγS NMR spectra.

To understand the mechanism by which oncogenic $G\alpha_q$ isoforms display greater SwII conformational heterogeneity when bound to GTP, we turned to all-atom molecular dynamics (MD) simulations. To this end, we performed 6 independent 2-μs simulations for each $G\alpha_q$-GTP isoform (WT, Q209L, and Q209P). In our simulations of WT $G\alpha_q$-GTP, the Q209 sidechain forms a hydrogen-bonding network with the γ-phosphate of GTP and the backbone amide of Q209 (Figure 2.2a). This hydrogen-bonding network was stable and long-lived; we found Q209 directly interacting with GTP for ~40-50% of our independent 2-μs simulation trajectories. We hypothesized that disrupting this hydrogen-bonding network by introducing oncogenic Q209 mutations would substantially increase SwII conformational heterogeneity.

In our WT $G\alpha_q$-GTP simulations, SwII (residues 210-220) is highly flexible and explores multiple backbone conformations (Figure 2.2a). As expected, introduction of oncogenic Q209 $G\alpha_q$ mutations (Q209L and Q209P) disrupts the hydrogen-bonding network between Q209 and the γ-phosphate of GTP and significantly increases SwII flexibility (Figure 2.2b,c). We observe a statistically significant increase in the root mean square deviation (r.m.s.d.) of backbone SwII atoms in both Q209L-GTP and Q209P-GTP simulations compared to WT-GTP (Figure 2.2d). Disruption of the Q209-GTP interaction and increased flexibility of SwII likely explains the impaired GTPase activity of these mutants[16]. Altogether, we conclude that SwII in oncogenic

Q209 $G\alpha_q$ mutants is significantly more flexible and conformationally heterogeneous than WT $G\alpha_q$. Increased SwII conformational heterogeneity likely explains mutant-specific patterns of $G\alpha_q$ effector protein engagement and diminished GTP hydrolysis activity.

Discovery of mutant-selective disulfide-containing chemical probes

We next sought to develop oncogene-selective chemical probes by exploiting conformational differences between WT and oncogenic Q209 $G\alpha_q$ mutants. Small molecules that selectively bind to and inhibit oncogenic $G\alpha_q$ would be promising leads for directed uveal melanoma therapies. We chose to target SwII of oncogenic Q209 $G\alpha_q$ mutants because we observed differences in SwII conformation between oncogenic Q209 mutants and WT $G\alpha_q$-GTP (Figure 2.1c,d,e, Figure 2.2a,b,c,d). Further, SwII forms a direct binding interface with $G\alpha_q$ effector proteins[30–32], making it an ideal target for small molecule-mediated disruption of oncogenic $G\alpha_q$ signaling.

We performed a disulfide-containing fragment screen against Q209L and Q209P $G\alpha_q$-GTPγS to identify covalent, oncogene-selective chemical binders (Figure 2.3a). Purified $G\alpha_q$-GTPγS was mixed with a library of 1,850 disulfide-containing fragments. Covalent $G\alpha_q$–fragment disulfide bond formation was then measured with a liquid chromatography/mass spectrometry (LC/MS) assay[34] (Figure 2.3b). Fragments that form non-specific disulfide bonds with $G\alpha_q$ are outcompeted by the presence of 2-mercaptoethanol, a thiol-containing reducing agent. We predicted that disulfide-containing fragments would form covalent bonds with C219 on SwII, as we previously saw covalent modification of this residue with our disulfide NMR probe (Figure 2.1c,d,e, Extended Data Figure 2.1). We calculated the average labeling of Q209L and Q209P $G\alpha_q$-GTPγS by disulfide-containing fragments across the library of 1,850 compounds to be 17.5 and 10.1%, respectively. Disulfide-containing fragments that bound Q209L or Q209P $G\alpha_q$-GTPγS three standard deviations above average labeling (59.5 and 40.1%, respectively) were

defined as hits (Figure 2.3b) and prioritized for further characterization. From our initial screen, we identified 19 Q209L $G\alpha_q$-GTPγS hits, 30 Q209P $G\alpha_q$-GTPγS hits, and 5 Q209L and Q209P $G\alpha_q$-GTPγS hits.

We next validated 51 of these disulfide-containing fragments hits in a limited 8-point dose-response LC/MS assay. Disulfide-containing fragments were serially diluted from 2.0 mM to 910 nM and mixed with either Q209L or Q209P $G\alpha_q$-GTPγS. To identify compounds that show oncogene-selective labeling, we simultaneously counter-screened these disulfide-containing fragments against WT $G\alpha_q$-GTPγS in the same dose-response assay. We observed 32 of our compounds labeled oncogenic Q209 $G\alpha_q$-GTPγS mutants with greater potency or efficacy than WT $G\alpha_q$-GTPγS (Extended Data Figure 2.2, Extended Data Figure 2.3). The high potency of many of these compounds for binding to oncogenic Q209 $G\alpha_q$-GTPγS mutants precluded us from seeing a dose-dependent titration of compound labeling in this limited fragment dilution series. We next performed an extended 20-point dose-response LC/MS assay for 10 of these mutant-selective compounds. Disulfide-containing fragments were serially diluted from 2.0 mM to 5.2 pM, mixed with WT, Q209L and Q209P $G\alpha_q$-GTPγS, and disulfide bond formation was assessed with LC/MS.

Almost all (8 of 10) compounds we tested in the extended dose-response assay showed greater potency (DR_{50}) for binding to Q209P $G\alpha_q$-GTPγS than WT $G\alpha_q$-GTPγS (Figure 2.3c, Extended Data Figure 2.3). Selective binding to Q209P $G\alpha_q$-GTPγS varies widely over the compound series: 993912 shows a modest 21-fold increase in binding potency, whereas 993803 shows a significant 1,300-fold increase in binding potency over WT $G\alpha_q$-GTPγS (Figure 2.3c). Most (7 of 10) fragments we tested in the extended dose-response assay also showed increased binding to Q209L $G\alpha_q$-GTPγS compared to WT $G\alpha_q$-GTPγS. The increase in potency for binding to Q209L $G\alpha_q$-GTPγS, however, was less substantial than what we observed for Q209P $G\alpha_q$-

GTPγS; 993803 showed a small 2.6-fold increase in binding potency, whereas 993912 showed a modest 20-fold increase in binding potency over WT $G\alpha_q$-GTPγS (Figure 2.3c).

Many of the oncogene-selective disulfide-containing fragments we characterized in the extended dose-response LC/MS assay share similar chemical structures and derive from a shared parent scaffold, 993695 (Figure 2.3d, Extended Data Figure 2.4). Compounds in the 993-class share a central pyrrolidine or piperidine ring. The nitrogen atom in the five- or six-membered ring is conjugated to an invariable 3,5-dichloro-4-hydroxyphenyl ring by either an amide or sulfonamide linker. The central pyrrolidine and piperidine scaffolds can be derivatized by appending phenyl substituents at the 3-, or 4-position, respectively. These phenyl substituents tolerate methyl and methyl ether substituents in the para-position or fluorines in the meta-positions. Interestingly, aliphatic substituents of the central pyrrolidine or piperidine do not bind Q209L or Q209P $G\alpha_q$-GTPγS with high affinity. The central pyrrolidine or piperidine scaffold has an invariable amide substitution at the 2-position, connecting the fragment portion of the molecule to the disulfide-containing dimethyl amine cap. The 4-phenyl and 2-amide substituents of the central pyrrolidine or piperidine ring are most often found in a trans racemic conformation.

As SwII is more conformationally heterogeneous in oncogenic Q209 $G\alpha_q$ mutants, we hypothesized that increased solvent accessibility of C219, the likely target of our disulfide-containing fragments, may explain the preferential oncogene-selectivity of these compounds. To test this hypothesis, we again turned to all-atom MD simulations. We calculated the root mean square fluctuation (r.m.s.f.) of C219 across all atoms in our WT, Q209L, and Q209P $G\alpha_q$-GTP simulations. We observed a statistically significant increase in the mobility of C219 in Q209L and Q209P $G\alpha_q$-GTP simulations compared to WT $G\alpha_q$-GTP simulations (Figure 2.2b,c,d, Extended Data Figure 2.5). These data suggest that C219 in Q209L and Q209P $G\alpha_q$-GTPγS is

more accessible to react with disulfide-containing fragments and may explain the oncogene-selective binding we observe in our LC/MS assays. We cannot rule out the possibility, however, that inherent differences in the ionization of WT, Q209L, and Q209P $G\alpha_q$-GTPγS during mass spectrometry may partially contribute to the selectivity differences we observe in our fragment binding assays.

Disulfide-containing fragments disrupt $G\alpha_q$-effector protein interactions

Covalent small molecules that selectively bind to and inhibit oncogenic Q209 $G\alpha_q$ signaling would be promising leads for targeted uveal melanoma therapies. Both WT and oncogenic Q209 $G\alpha_q$ mutants activate phospholipase C β_3 (PLCβ_3), a key downstream effector that converts PtdIns(4,5)*P*2 in the plasma membrane to diacylglycerol (DAG) and cytosolic InsP3[35]. Accumulation of DAG activates protein kinase C (PKC), resulting in proliferative cellular signaling via the CRAF/MEK/ERK mitogen activated protein kinase (MAPK) pathway[36]. Primary human melanocytes transfected with Q209L $G\alpha_q$ show increased levels of ERK phosphorylation—a downstream readout of MAPK pathway activity—when compared to melanocytes transfected with WT $G\alpha_q$[11,12]. Oncogenic Q209 $G\alpha_q$ mutants therefore constitutively activate the MAPK pathway in a PLCβ_3-dependent manner to mediate pro-tumorigenic proliferative cellular signaling[1,2,11,12]. Structures of the GDP-AlF_4-activated $G\alpha_q$-PLCβ_3 signaling complex show a key SwII-mediated binding interface[30] (Figure 2.4a). As SwII is the likely target of our mutant-selective disulfide-containing fragments, we hypothesized that covalent fragment tethering may selectively disrupt oncogenic Q209 mutant $G\alpha_q$–PLCβ_3 interactions and inhibit pro-tumorigenic MAPK signaling.

To determine whether our disulfide-containing fragments inhibit the binding of PLCβ_3, we developed a fluorescence anisotropy assay by using a previously characterized[37] TAMRA-labeled 27-mer peptide derived from PLCβ_3 (residues 852-878, PLCβ_3-TMR). Disulfide-

containing fragments that selectively inhibit binding of PLCβ$_3$-TMR to Q209 Gα$_q$ mutants would be promising leads to disrupt full-length oncogenic Q209 Gα$_q$–PLCβ$_3$ interactions. We first determined the empirical affinity (K_D) for PLCβ$_3$-TMR binding to WT, Q209L, and Q209P Gα$_q$-GTPγS as 2.4, 2.5, and 6.9 μM, respectively (Extended Data Figure 2.5). WT and Q209L Gα$_q$-GTPγS bind PLCβ$_3$-TMR with nearly identical K_D values, whereas Q209P Gα$_q$-GTPγS binds with a ~2.8-fold reduction in affinity. We speculate the reduction in PLCβ$_3$-TMR affinity arises from increased conformational heterogeneity of the Q209P-GTPγS SwII binding interface compared to WT and Q209L Gα$_q$-GTPγS (Figure 2.1c,d,e). We then incubated WT, Q209L and Q209P Gα$_q$-GTPγS with 30 of our 32 compounds that possessed either increased potency or efficacy of binding to oncogenic Q209 Gα$_q$-GTPγS mutants (Extended Data Figure 2.3, Extended Data Figure 2.4) and assessed binding of PLCβ$_3$-TMR with fluorescence anisotropy (Figure 2.4c, Extended Data Figure 2.5).

We separately normalized PLCβ$_3$-TMR binding to WT, Q209L, and Q209P Gα$_q$-GTPγS to vehicle (DMSO) and no Gα$_q$-GTPγS controls as 100% and 0% binding, respectively (Figure 2.4c). Disulfide-containing fragments that fully inhibit PLCβ$_3$-TMR binding to Gα$_q$-GTPγS show values close to 0%; whereas, fragments that cannot inhibit PLCβ$_3$-TMR binding to Gα$_q$-GTPγS show values close to 100% (Figure 2.4b). We observed a wide range of compound activity within the 30 disulfide-containing fragments we tested (Figure 2.4c, Extended Data Figure 2.5). All 10 of the oncogene-selective compounds we tested in our extended 20-point dose-response LC/MS assay were successful in inhibiting ~50% of PLCβ$_3$-TMR binding to Q209P Gα$_q$-GTPγS (Figure 2.4c). These disulfide-containing fragments were less potent against Q209L Gα$_q$-GTPγS, inhibiting only 30-40% of total PLCβ$_3$-TMR binding. In general, our disulfide-fragments showed greater selectivity in inhibiting PLCβ$_3$-TMR binding to Q209P Gα$_q$-GTPγS. Fragment-mediated inhibition of PLCβ$_3$-TMR binding to Q209L Gα$_q$-GTPγS, however, closely mirrored inhibition of PLCβ$_3$-TMR binding to WT Gα$_q$-GTPγS.

Overall, the 993-class of disulfide-containing fragments demonstrated the greatest inhibition of PLCβ$_3$-TMR binding to WT, Q209L, and Q209P Gα$_q$-GTPγS (Extended Data Figure 2.5). Compound 993695, the parent scaffold of many 993-class fragments, showed exceptional potency against WT and Q209L Gα$_q$-GTPγS, preventing 80 and 65% of PLCβ$_3$-TMR binding, respectively. Interestingly, compounds 993799 and 993804 are diastereomers that show differential activity in our PLCβ$_3$-TMR binding assay (Figure 2.4c,d). The 2-amide and 4-phenyl substituents of the central piperidine ring must be in a *trans* racemic conformation to inhibit PLCβ$_3$-TMR binding to WT and Q209L Gα$_q$-GTPγS. This suggests that 993-compound mediated inhibition of PLCβ$_3$-TMR binding occurs in a specific and geometrically precise manner (Figure 2.4c). Compounds in the 917- and 1075-class of disulfide-containing fragments were weakly active in preventing PLCβ$_3$-TMR binding to Q209P Gα$_q$-GTPγS, but were poor inhibitors of PLCβ$_3$-TMR binding to Q209L and WT Gα$_q$-GTPγS (Extended Data Figure 2.5).

We previously hypothesized that our disulfide-containing fragments were binding to Gα$_q$ via covalent tethering to SwII C219, as we observed robust labeling of this residue with our cysteine-reactive disulfide NMR probe (Figure 2.1c,d,e, Extended Data Figure 2.1). Our hypothesis was further bolstered by the proximity of C219 to the PLCβ$_3$ binding interface (Figure 2.4a) and the observation that disulfide-containing fragments could inhibit the binding of PLCβ$_3$-TMR. To test this hypothesis, we created a mutant Gα$_q$ construct in which we replaced the SwII cysteine with alanine. We then purified C219A Gα$_q$-GTPγS, mixed it with our panel of 30 putatively oncogene-selective disulfide-containing fragments, and measured binding of PLCβ$_3$-TMR with fluorescence anisotropy. The C219A Gα$_q$ construct contains the WT Q209 residue; as such, we directly looked for differences in fragment-mediated inhibition of PLCβ$_3$-TMR binding between WT and C219A Gα$_q$-GTPγS. Happily, we observed that almost all disulfide-containing fragments showed very weak or negligible inhibition of PLCβ$_3$-TMR binding to C219A Gα$_q$-GTPγS (Figure 2.4c, Extended Data Figure 2.5). Notably, almost all disulfide-containing

fragments from the 993-class completely lost their ability to inhibit PLCβ$_3$-TMR binding to C219A Gα$_q$-GTPγS. These data support our initial hypothesis that SwII C219 is the site of covalent modification by our oncogene-selective disulfide-containing fragments.

In sum, we aimed to develop covalent small molecules that would selectively bind to and inhibit oncogenic Q209 Gα$_q$ mutants. We identified 30 disulfide-containing fragments that bind to Gα$_q$ with variable degrees of oncogene-selectivity (Figure 2.3, Extended Data Figure 2.2, Extended Data Figure 2.3). Some compounds bind WT and oncogenic Q209 Gα$_q$-GTPγS mutants equally well (993799 and 993948, Extended Data Figure 2.3), while others bind Q209P Gα$_q$-GTPγS 1000-fold more potently than WT Gα$_q$-GTPγS (993803 and 993805, Figure 2.3, Extended Data Figure 2.3). We showed many of these disulfide-containing fragments prevent binding of a fluorescently-labeled PLCβ$_3$ peptide, and that inhibition of PLCβ$_3$ peptide binding was specific to covalent modification of SwII C219 on Gα$_q$ (Figure 2.4c).

We did not observe fragment-mediated inhibition of PLCβ$_3$-TMR binding to Gα$_q$ in an oncogene-selective manner, despite observing favorable selectivity profiles of these compounds in our binding assay. There are two important caveats to this interpretation. First, we cannot rule out the possibility that inherent differences in the ionization of WT, Q209L, and Q209P Gα$_q$-GTPγS during LC/MS could partially contribute to the mutant-selective binding profiles we observe. Second, the PLCβ$_3$ binding assay is conducted in the absence of a reducing agent, while our LC/MS samples are supplemented with 500 μM 2-mercaptoethanol. Selectivity differences between WT, Q209L, and Q209P Gα$_q$-GTPγS may be bolstered by the presence of strong reducing agent, which can effectively compete weaker disulfide-containing fragments for binding to WT Gα$_q$-GTPγS. Nevertheless, we have discovered a new class of covalent small molecules that bind Gα$_q$-GTPγS and prevent binding of a PLCβ$_3$-derived peptide, serving as promising leads for future targeted uveal melanoma therapies.

One limitation of the present study, however, is that we did not assess whether our disulfide-containing fragments could inhibit interactions between $G\alpha_q$-GTP and TrioC, the downstream initiator of oncogenic $G\alpha_q$-mediated YAP signaling[18]. Structures of GDP-AlF_4-activated $G\alpha_q$ in complex with p63RhoGEF[32], a closely related TrioC homolog[38], show p63RhoGEF binding the same SwII interface as $PLC\beta_3$ (Extended Data Figure 2.5). There is high sequence homology (86% similarity) between p63RhoGEF and TrioC in the 21 amino acid stretch of p63RhoGEF that forms the SwII binding interface (Extended Data Figure 2.5). We therefore speculate that TrioC may bind $G\alpha_q$-GTP SwII in a similar orientation as p63RhoGEF. As such, we envision that our SwII-targeting disulfide-containing fragments may be able to inhibit both $G\alpha_q$-$PLC\beta_3$ and $G\alpha_q$-TrioC interactions, effectively targeting oncogenic MAPK and YAP signaling in uveal melanoma.

2.4 Discussion

Uveal melanomas are almost exclusively driven by acquired somatic mutations at Q209 in the $G\alpha_{q/11}$ family of heterotrimeric G proteins[11,12]. To elaborate the mechanism of oncogenic $G\alpha_{q/11}$ signaling, we first characterized the conformational landscape of Q209 $G\alpha_q$ mutants using NMR and molecular dynamics simulations. We discovered that SwII in oncogenic Q209 $G\alpha_q$-GTP mutants displays greater dynamic flexibility than SwII in WT $G\alpha_q$-GTP. We then employed a disulfide-containing fragment screen to target these apparent conformational differences and discovered oncogene-selective covalent small molecules. Our fragments bind to C219 on SwII and show greater apparent affinity for oncogenic Q209 $G\alpha_q$ mutants than WT $G\alpha_q$. Covalent tethering to SwII prevents binding of a PLCβ_3-derived peptide, a key $G\alpha_q$ effector protein that is hijacked in oncogenic signaling[2,11,12,16]. While the current study is limited to *in vitro* characterization of our disulfide-containing fragments, these compounds show the promise of leveraging conformational differences in oncogenic Q209 $G\alpha_q$ mutants to develop oncogene-selective uveal melanoma therapies. Future work will establish the *in vivo* efficacy of our disulfide-containing fragments and improve their functional oncogene-selectivity.

Our work revises canonical mechanisms of oncogenic $G\alpha_q$ function in uveal melanoma. Prevailing hypotheses postulate that loss of Q209 causes impaired guanine nucleotide hydrolysis, leading oncogenic Q209 $G\alpha_q$ mutants to adopt a constitutive GTP-bound conformation in the cell[1,2]. While oncogenic Q209 $G\alpha_q$ mutants are indeed deficient in exercising hydrolysis of GTP[16], our work adds significant and important nuance to this model. We show that oncogenic Q209 $G\alpha_q$ mutants explore novel conformational landscapes compared to WT $G\alpha_q$, enabling development of oncogene-selective covalent small molecules. These findings suggest that the function of oncogenic Gα mutants is likely more complicated than a simple guanine nucleotide exchange activation model can explain. Indeed, our work aligns well with recent biochemical characterization of cancer-associated $G\alpha_q$[16] and $G\alpha_s$[39] mutants, which show

atypical models of oncogenic Gα signaling. Altogether, the emerging therapeutic window between WT and oncogenic $G\alpha_q$ function motivates new efforts to develop mutant-selective and targeted G protein therapies.

Uveal melanoma is a devastating and intractable form of cancer. Half of all patients diagnosed with primary disease will progress to metastasis, carrying a ~1 year terminal prognosis[4–6]. More than 80% of all uveal melanomas arise from acquired somatic mutations at Q209 in the $G\alpha_{q/11}$ family of heterotrimeric G proteins[11]. Yet, there are no currently available treatments that directly target oncogenic $G\alpha_{q/11}$ driver mutations in uveal melanoma. Emerging immunotherapies have shown great promise in treating cutaneous melanomas, which primarily arise from acquired V600E BRAF mutations[7,9,10]. Targeting uveal melanomas with similar immunotherapeutic approaches, however, has largely been unsuccessful[5]. Our work further demystifies the mechanism of oncogenic $G\alpha_q$ signaling in cancer. While preliminary, our characterization of $G\alpha_q$ targeted disulfide-containing fragments shows a promising future for small molecule-mediated inhibition of oncogenic $G\alpha_q$ signaling in uveal melanoma.

2.5 Materials & Methods

Generation of $G\alpha_q$ Expi293 stable cells

For biochemical characterization of $G\alpha_q$ function, human *GNAQ* with an N-terminal Protein C epitope tag followed by a flexible glycine/serine linker was cloned into a pcDNA^{TM}3.1/Zeo$^{(+)}$ vector containing a tetracycline-inducible expression cassette. To enable detergent-free reconstitution of $G\alpha_q$, endogenously palmitoylated cysteines (C9 and C10) were mutated to alanine with site-directed mutagenesis. The resulting ProC-C9A-C10A-GNAQ-WT construct was mutated to the corresponding oncogenic $G\alpha_q$ isoforms (Q209L and Q209P) using site-directed mutagenesis.

All three $G\alpha_q$ constructs (WT, Q209L, and Q209P) were separately transfected into adherent Expi293F^{TM} Inducible Human Embryonic Kidney Cells (unauthenticated and untested for mycoplasma contamination, Life Technologies) using Lipofectamine 2000© and cells were maintained in DMEM (Gibco, 11995-065), 10% FBS (Gibco), 100 U/mL penicillin and 100 µg/mL streptomycin at 37 °C and 5% CO_2 in a standing incubator. Cells stably incorporating the $G\alpha_q$ plasmids were selected under antibiotic pressure with zeocin (1 mg/mL, InvivoGen) and blasticidin (10 µg/mL, InvivoGen). The resulting polyclonal ProC-C9A-C10A-GNAQ stable cell lines were adapted to suspension culture and maintained in Expi293^{TM} Expression Medium (Gibco) supplemented with zeocin (5 µg/mL) and blasticidin (5 µg/mL) at 37 °C and 8 % CO_2 on a shaking platform at 125 rpm. Expression of $G\alpha_q$ was induced with addition of doxycycline hyclate (1 µg/mL, Sigma Aldrich) and enhanced with sodium butyrate (5 mM, Sigma Aldrich). Induced Expi293F^{TM} $G\alpha_q$ stable cells were harvested 72 hours after induction and stored at -80 °C until further use.

Expression and purification of $G\alpha_q$-GDP

For purification, cells were thawed and resuspended in detergent lysis buffer (20 mM HEPES pH 8.0, 150 mM NaCl, 1 mM EDTA, 11 mM CHAPS hydrate) supplemented with protease inhibitors (20 µg/mL leupeptin, 160 µg/mL benzamidine), reducing agent (100 µM TCEP) and guanosine diphosphate (GDP, 20 µM, Sigma Aldrich). Resuspended cells were disrupted by dounce homogenization and solubilized for 1 hour at 4 °C. After high-speed centrifugation, the supernatant was subjected to affinity purification using homemade anti-Protein C antibody coupled to Sepharose beads. GDP-bound $G\alpha_q$ ($G\alpha_q$-GDP) immobilized on Protein C-beads was washed extensively to remove detergent and lower salt concentration while maintaining GDP (20 µM) in all wash buffers. $G\alpha_q$-GDP was eluted in 20 mM HEPES pH 8.0, 100 mM NaCl, 100 µM TCEP, 5 mM EDTA, 20 µM GDP, and 0.2 mg/mL Protein C peptide (Genscript). Eluted $G\alpha_q$-GDP was concentrated with a 10 kDa MWCO spin concentrator (Millipore) and purified to homogeneity with size-exclusion chromatography, using a Superdex S200 Increase 10/300 GL column (GE Healthcare) equilibrated in 20 mM HEPES pH 8.0, 100 mM NaCl. Fractions containing monodisperse $G\alpha_q$-GDP protein were pooled, concentrated, and flash frozen for future use.

Expression and purification of $G\alpha_q$-GTPγS

GTPγS-bound $G\alpha_q$ ($G\alpha_q$-GTPγS) was expressed and purified exactly as described above for $G\alpha_q$-GDP until affinity purification. $G\alpha_q$ immobilized on Protein C-beads was washed extensively to remove detergent and GDP, and lower salt concentration. $G\alpha_q$ was eluted in 20 mM HEPES pH 8.0, 100 mM NaCl, 100 µM TCEP, 5 mM EDTA and 0.2 mg/mL Protein C peptide (Genscript). Eluted $G\alpha_q$ was concentrated with a 10 kDa MWCO spin concentrator (Millipore) and buffer exchanged into 20 mM HEPES pH 8.0, 100 mM NaCl, 100 µM TCEP, and 5 mM $MgCl_2$ to remove residual EDTA. Excess GTPγS (10x molar equivalent) was added to eluted $G\alpha_q$ and incubated at room temperature for 18 hours to facilitate guanine nucleotide exchange.

$G\alpha_q$-GTPγS was purified to homogeneity with size-exclusion chromatography, using a Superdex S200 Increase 10/300 GL column (GE Healthcare) equilibrated in 20 mM HEPES pH 8.0, 100 mM NaCl. Fractions containing monodisperse $G\alpha_q$-GTPγS protein were pooled, concentrated, and flash frozen for future use.

Expression and purification of S-Methyl-^{13}C methanethiosulfonate-labeled $G\alpha_q$-GDP

S-Methyl-^{13}C methanethiosulfonate-labeled $G\alpha_q$-GDP (^{13}C-MMTS-$G\alpha_q$-GDP) was expressed and purified exactly as described above for $G\alpha_q$-GDP until affinity purification. $G\alpha_q$-GDP immobilized on Protein C-beads was washed extensively to remove detergent and TCEP, and lower salt concentration while maintaining GDP (20 μM) in all wash buffers. $G\alpha_q$-GDP was eluted in 20 mM HEPES pH 8.0, 100 mM NaCl, 5 mM EDTA, 20 μM GDP, and 0.2 mg/mL Protein C peptide (Genscript). Excess S-Methyl-^{13}C methanethiosulfonate (^{13}C-MMTS, 10x molar equivalent, Sigma Aldrich) was added to eluted $G\alpha_q$-GDP and incubated at room temperature for 18 hours to facilitate labeling. ^{13}C-MMTS-$G\alpha_q$-GDP was purified to homogeneity with size-exclusion chromatography, using a Superdex S200 Increase 10/300 GL column (GE Healthcare) equilibrated in 20 mM HEPES pH 8.0, 100 mM NaCl. Fractions containing monodisperse ^{13}C-MMTS-$G\alpha_q$-GDP were pooled, concentrated, and serially buffer exchanged into an H_2O-free NMR buffer, containing 10 mM sodium phosphate, 100 mM NaCl and 1 μM GDP solvated in D_2O (Sigma Aldrich) at pD 7.3 (adjusted with concentrated DCl, Sigma Aldrich).

NMR Spectroscopy

For the initial GDP-bound measurement, each ^{13}C-MMTS-$G\alpha_q$-GDP sample (WT, Q209L, and Q209P) was diluted to 20 μM in the D_2O NMR buffer described above. Sodium trimethylsilylpropanesulfate (DSS) was added at 500 μM to the samples as a chemical shift referencing standard for NMR spectra. For the GTPγS-bound samples, 100 μM GTPγS and

5mM $MgCl_2$ were added to the initial sample. Upon addition of GTPγS, a time-course was measured over 16 hours to evaluate nucleotide exchange. Samples were measured using a $^{1}H–^{13}C$-HSQC experiment measured at 298K on a triple-resonance Bruker Avance Neo 800 Hz spectrometer equipped with a cryoprobe. Data were processed with NMRPipe[40] and analyzed using CcpNmr[41]. The peak corresponding to residue C219 in Switch II was assigned by measuring a C219A mutant $G\alpha_q$ (Extended Data Fig. 1).

Disulfide tethering screen and data processing

The primary disulfide tethering screen was performed by incubating GTPγS-bound oncogenic $G\alpha_q$ isoforms (Q209L or Q209P) with disulfide-containing fragment molecules in a 384-well plate format. The UCSF Small Molecule Discovery Center (SMDC) custom 1600 disulfide-containing fragment library was available as 50 mM stock solutions in DMSO. $G\alpha_q$-GTPγS (Q209L or Q209P) was diluted in assay buffer (10 mM Tris pH 8.0, 500 μM betamercaptoethanol) to a final concentration of 200 nM and plated in 384-well plates (25 μL/well). Each disulfide-containing fragment molecule (100 nL) was pinned from library master plates using non-sterile disposable 384 polypropylene pin tools (V & P Scientific), giving a final fragment concentration of 200 μM in each well. The $G\alpha_q$-fragment reactions were incubated at room temperature for 3 hours before being measured by LC/MS (I-class Acquity UPLC/ Xevo G2-XS Quadrupole Time of Flight mass spectrometer, Waters). Data collection and automated processing followed a custom workflow, as previously described[34]. Compound resynthesis was performed following published procedures[42,43].

Initial hit validation and oncogene selectivity LC/MS Experiments

Disulfide-containing fragment molecules from our initial tethering screen that labeled oncogenic $G\alpha_q$-GTPγS isoforms (Q209L or Q209P) three standard deviations above average were retested in an 8-point dose-response LC/MS assay. Of the 54 compounds that bound three

standard deviations above average, there were 19 Q209L hits, 30 Q209L hits, and 5 hits that bound both Q209L and Q209P. To probe the oncogene-selectivity of these compounds, fragments were counter-screened against WT $G\alpha_q$-GTPγS in the same dose-response series. Compounds were titrated from 50 mM to 23 μM in a 3-fold dilution series in DMSO. Then, each compound (1 μL) was transferred into 24 μL of $G\alpha_q$-GTPγS (200 nM) diluted in assay buffer. The concentration range for each tested compound was 2.0 mM – 910 nM with a final concentration of 4% DMSO in each reaction. A final well of DMSO without compound was used as a control at the end of every dilution series. The $G\alpha_q$-fragment reactions were incubated at room temperature for 3 hours before being measured by LC/MS as described above. The percentage of labeled $G\alpha_q$-GTPγS by disulfide-containing fragments was extracted and DR_{50} curves were fit in GraphPad Prism (v9.0) using a log(agonist) vs. response – fixed slope, three parameter fit.

Extended Dose Response LC/MS Experiments

The binding of oncogene-selective disulfide-containing fragments to $G\alpha_q$-GTPγS (WT, Q209L, and Q209P) was probed using an extended 20-point dose response LC/MS assay. The mass spectrometry dose response assay was performed using the same assay buffer (10 mM Tris pH 8.0, 500 μM betamercaptoethanol) as the primary screen. Compounds were titrated from 50 mM to 0.129 nM in a 3-fold dilution series in DMSO. Then, each compound (1 μL) was transferred into 24 μL of $G\alpha_q$-GTPγS (200 nM) diluted in assay buffer. The concentration range for each tested compounds was 2.0 mM – 5.2 pM with a final concentration of 4% DMSO in each reaction. The binding of each compound concentration and $G\alpha_q$-GTPγS was collected in technical triplicates. A final well of DMSO without compound was used as a control at the end of every dilution series. The $G\alpha_q$-fragment reactions were incubated at room temperature for 3 hours before being measured by LC/MS as described above. The percentage of labeled $G\alpha_q$-

GTPγS by disulfide-containing fragments was extracted and DR_{50} curves were fit in GraphPad Prism (v9.0) using a log(agonist) vs. response – fixed slope, three parameter fit.

Fluorescence polarization (saturation binding of PLCβ$_3$-TMR to Gα$_q$)

Gα$_q$-GTPγS (WT, Q209L, Q209P) was reconstituted at a high concentration (WT & Q209L = 26.7 μM, Q209P = 93.3 μM) in assay buffer (20 mM HEPES pH 8.0, 100 mM NaCl, 5 mM $MgCl_2$) supplemented with excess GTPγS (500 μM). Gα$_q$-GTPγS was serially diluted in 3-fold dilution steps to create a 7-point protein dilution curve. A zero-concentration point (no added Gα$_q$-GTPγS) was included as a normalization control. The serial dilution of Gα$_q$-GTPγS was plated in triplicate (15 μL per well) in black, non-binding surface, low-volume, 384-well plates (Corning ref. 3820). An N-terminally tetramethylrhodamine-labeled 27-mer peptide derived from phospholipase C β$_3$[37] (PLCβ$_3$-TMR, residues 852-878) with two point mutations (I860A, M869Nle) and C-terminal amidation was synthesized (Genscript) and reconstituted in 10 mM K_2HPO_4. PLCβ$_3$-TMR was sequentially diluted in assay buffer to 100 nM and 5 μL was added to each well containing Gα$_q$-GTPγS. The 384-well plate was covered with an aluminum plate seal, centrifuged, and incubated at room-temperature for 3 hours. To probe PLCβ$_3$-TMR binding to Gα$_q$-GTPγS, the fluorescence polarization at an excitation wavelength of 540 nm and an emission wavelength of 590 nm was recorded and calculated using a CLARIOstar^{Plus} (BMG LABTECH) microplate reader. Slit width for emission and excitation filters was 20 nm and acquisition setting time was 0.2 seconds with 200 flashes. The gain for emission and excitation filters was adjusted to PLCβ$_3$-TMR alone wells and set to 100 mP units using the CLARIOstar^{Plus} automatic adjustment feature. Saturation binding data were fit in GraphPad Prism software (v9.0) using a one-site total binding equation, constraining background signal to 100 mP units and non-specific binding to 0 mP units.

Fluorescence polarization (disulfide fragment activity assay)

$G\alpha_q$-GTPγS was reconstituted at empirically determined concentrations (WT & Q209L = 1 μM, Q209P = 7 μM) in assay buffer (20 mM HEPES pH 8.0, 100 mM NaCl, 5 mM $MgCl_2$) supplemented with excess GTPγS (100 μM) . These concentrations were chosen as they represent an equal number of $G\alpha_q$-$PLC\beta_3$ peptide binding events for each $G\alpha_q$ isoform, as determined in our $PLC\beta_3$-TMR saturation binding experiments. Disulfide-containing fragment molecules from our initial validation screen that demonstrated oncogene selective labeling were tested for their ability to prevent the $G\alpha_q$-$PLC\beta_3$ peptide binding interaction. We tested 30 compounds, which represented 8 Q209L hits, 18 Q209P hits, and 4 hits that bound both Q209L and Q209P. Compounds were first diluted to 5 mM in DMSO. Next, compounds (1.1 μL) were transferred into 54 μL of $G\alpha_q$-GTPγS, giving a final compound concentration of 100 μM. The reactions of $G\alpha_q$-GTPγS with the disulfide fragments were plated in duplicate (Q209L,15 μL per well) or triplicate (WT & Q209P, 15 μL per well) in a black, non-binding surface, low-volume, 384-well plates (Corning ref. 3820).The 384-well plate was covered with an aluminum plate seal, centrifuged, and incubated at room-temperature for 3 hours. Next, 5 μL of $PLC\beta_3$-TMR (100 nM) was added to each well containing a $G\alpha_q$-GTPγS-compound mixture, giving a final $PLC\beta_3$-TMR concentration of 25 nM. Two important control conditions were prepared. Triplicate wells containing $G\alpha_q$-GTPγS alone (no compound) were included as a 100% peptide binding, DMSO vehicle control. Triplicate wells containing $PLC\beta_3$-TMR alone (no $G\alpha_q$-GTPγS) served as a 0% peptide binding normalization control. After addition of $PLC\beta_3$-TMR, the 384-well plate was covered with an aluminum plate seal, centrifuged, and incubated at room-temperature for 30 minutes. To test the ability of the disulfide-containing fragments to block $G\alpha_q$-$PLC\beta_3$ peptide binding interactions, the the fluorescence polarization was calculated as described above. The gain for emission and excitation filters was adjusted to $PLC\beta_3$-TMR alone wells and set to 100 mP units using the CLARIOstar^{Plus} automatic adjustment feature. Data represent one biological replicate of duplicate (Q209L) or triplicate (WT, Q209P) technical replicates. Raw fluorescent

polarization values (mP units) were normalized to vehicle (DMSO) and no $G\alpha_q$-GTPγS controls as 100% and 0% binding, respectively.

2.6 References

1. O'Hayre, M. *et al.* The emerging mutational landscape of G proteins and G-protein-coupled receptors in cancer. *Nat. Rev. Cancer* **13**, 412–424 (2013).
2. Arang, N. & Gutkind, J. S. G Protein-Coupled receptors and heterotrimeric G proteins as cancer drivers. *FEBS Lett.* **594**, 4201–4232 (2020).
3. Helgadottir, H. & Höiom, V. The genetics of uveal melanoma: current insights. *Appl. Clin. Genet.* **9**, 147–155 (2016).
4. Singh, A. D., Turell, M. E. & Topham, A. K. Uveal melanoma: trends in incidence, treatment, and survival. *Ophthalmology* **118**, 1881–1885 (2011).
5. Buder, K., Gesierich, A., Gelbrich, G. & Goebeler, M. Systemic treatment of metastatic uveal melanoma: review of literature and future perspectives. *Cancer Med.* **2**, 674–686 (2013).
6. Carvajal, R. D. *et al.* Metastatic disease from uveal melanoma: treatment options and future prospects. *Br. J. Ophthalmol.* **101**, 38–44 (2017).
7. Schank, T. E. & Hassel, J. C. Immunotherapies for the Treatment of Uveal Melanoma-History and Future. *Cancers* **11**, (2019).
8. Nathan, P. *et al.* Overall Survival Benefit with Tebentafusp in Metastatic Uveal Melanoma. *N. Engl. J. Med.* **385**, 1196–1206 (2021).
9. Davies, H. *et al.* Mutations of the BRAF gene in human cancer. *Nature* **417**, 949–954 (2002).
10. Pollock, P. M. *et al.* High frequency of BRAF mutations in nevi. *Nat. Genet.* **33**, 19–20 (2003).
11. Van Raamsdonk, C. D. *et al.* Frequent somatic mutations of GNAQ in uveal melanoma and blue naevi. *Nature* **457**, 599–602 (2009).
12. Van Raamsdonk, C. D. *et al.* Mutations in GNA11 in uveal melanoma. *N. Engl. J. Med.* **363**, 2191–2199 (2010).

13. Hilger, D., Masureel, M. & Kobilka, B. K. Structure and dynamics of GPCR signaling complexes. *Nat. Struct. Mol. Biol.* **25**, 4–12 (2018).
14. Sondek, J., Lambright, D. G., Noel, J. P., Hamm, H. E. & Sigler., P. B. GTPase mechanism of Gproteins from the 1.7-A crystal structure of transducin α-GDP–AlF4. *Nature* **372**, 276–279 (1994).
15. Sprang, S. R. Activation of G proteins by GTP and the mechanism of Gα-catalyzed GTP hydrolysis. *Biopolymers* **105**, 449–462 (2016).
16. Maziarz, M. *et al.* Atypical activation of the G protein Gαq by the oncogenic mutation Q209P. *J. Biol. Chem.* **293**, 19586–19599 (2018).
17. Vaqué, J. P. *et al.* A genome-wide RNAi screen reveals a Trio-regulated Rho GTPase circuitry transducing mitogenic signals initiated by G protein-coupled receptors. *Mol. Cell* **49**, 94–108 (2013).
18. Feng, X. *et al.* Hippo-independent activation of YAP by the GNAQ uveal melanoma oncogene through a trio-regulated rho GTPase signaling circuitry. *Cancer Cell* **25**, 831–845 (2014).
19. Yu, F.-X. *et al.* Mutant Gq/11 promote uveal melanoma tumorigenesis by activating YAP. *Cancer Cell* **25**, 822–830 (2014).
20. Moore, A. R. *et al.* Recurrent activating mutations of G-protein-coupled receptor CYSLTR2 in uveal melanoma. *Nat. Genet.* **48**, 675–680 (2016).
21. Johansson, P. *et al.* Deep sequencing of uveal melanoma identifies a recurrent mutation in PLCB4. *Oncotarget* **7**, 4624–4631 (2015).
22. Taniguchi, M. *et al.* YM-254890, a novel platelet aggregation inhibitor produced by Chromobacterium sp. QS3666. *J. Antibiot.* **56**, 358–363 (2003).
23. Nishimura, A. *et al.* Structural basis for the specific inhibition of heterotrimeric Gq protein by a small molecule. *Proc. Natl. Acad. Sci. U. S. A.* **107**, 13666–13671 (2010).

24. Fujioka, M., Koda, S., Morimoto, Y. & Biemann, K. Structure of FR900359, a cyclic depsipeptide from Ardisia crenata sims. *J. Org. Chem.* **53**, 2820–2825 (1988).
25. Lapadula, D. *et al.* Effects of Oncogenic Gαq and Gα11 Inhibition by FR900359 in Uveal MelanomaOncogenic Gαq/11 Inhibition by FR900359 in Uveal Melanoma. *Mol. Cancer Res.* **17**, 963–973 (2019).
26. Annala, S. *et al.* Direct targeting of Gαq and Gα11 oncoproteins in cancer cells. *Sci. Signal.* **12**, (2019).
27. Onken, M. D. *et al.* Targeting primary and metastatic uveal melanoma with a G protein inhibitor. *J. Biol. Chem.* **296**, 100403 (2021).
28. Religa, T. L., Ruschak, A. M., Rosenzweig, R. & Kay, L. E. Site-directed methyl group labeling as an NMR probe of structure and dynamics in supramolecular protein systems: applications to the proteasome and to the ClpP protease. *J. Am. Chem. Soc.* **133**, 9063–9068 (2011).
29. Chidiac, P., Markin, V. S. & Ross, E. M. Kinetic control of guanine nucleotide binding to soluble Galpha(q). *Biochem. Pharmacol.* **58**, 39–48 (1999).
30. Waldo, G. L. *et al.* Kinetic scaffolding mediated by a phospholipase C-beta and Gq signaling complex. *Science* **330**, 974–980 (2010).
31. Tesmer, V. M., Kawano, T., Shankaranarayanan, A., Kozasa, T. & Tesmer, J. J. G. Snapshot of activated G proteins at the membrane: the Galphaq-GRK2-Gbetagamma complex. *Science* **310**, 1686–1690 (2005).
32. Lutz, S. *et al.* Structure of Galphaq-p63RhoGEF-RhoA complex reveals a pathway for the activation of RhoA by GPCRs. *Science* **318**, 1923–1927 (2007).
33. Taylor, V. G., Bommarito, P. A. & Tesmer, J. J. G. Structure of the Regulator of G Protein Signaling 8 (RGS8)-Gαq Complex: MOLECULAR BASIS FOR Gα SELECTIVITY*. *J. Biol. Chem.* **291**, 5138–5145 (2016).

34. Hallenbeck, K. K. *et al.* A Liquid Chromatography/Mass Spectrometry Method for Screening Disulfide Tethering Fragments. *SLAS Discov* **23**, 183–192 (2018).
35. Hubbard, K. B. & Hepler, J. R. Cell signalling diversity of the Gqalpha family of heterotrimeric G proteins. *Cell. Signal.* **18**, 135–150 (2006).
36. Rozengurt, E. Mitogenic signaling pathways induced by G protein-coupled receptors. *J. Cell. Physiol.* **213**, 589–602 (2007).
37. Charpentier, T. H. *et al.* Potent and Selective Peptide-based Inhibition of the G Protein Gαq*. *J. Biol. Chem.* **291**, 25608–25616 (2016).
38. Bandekar, S. J. *et al.* Structure of the C-terminal guanine nucleotide exchange factor module of Trio in an autoinhibited conformation reveals its oncogenic potential. *Sci. Signal.* **12**, (2019).
39. Hu, Q. & Shokat, K. M. Disease-Causing Mutations in the G Protein Gαs Subvert the Roles of GDP and GTP. *Cell* **173**, 1254–1264.e11 (2018).
40. Delaglio, F. *et al.* NMRPipe: a multidimensional spectral processing system based on UNIX pipes. *J. Biomol. NMR* **6**, 277–293 (1995).
41. Vranken, W. F. *et al.* The CCPN data model for NMR spectroscopy: development of a software pipeline. *Proteins* **59**, 687–696 (2005).
42. Burlingame, M. A., Tom, C. T. M. B. & Renslo, A. R. Simple one-pot synthesis of disulfide fragments for use in disulfide-exchange screening. *ACS Comb. Sci.* **13**, 205–208 (2011).
43. Turner, D. M., Tom, C. T. M. B. & Renslo, A. R. Simple plate-based, parallel synthesis of disulfide fragments using the CuAAC click reaction. *ACS Comb. Sci.* **16**, 661–664 (2014).

2.7 Figures

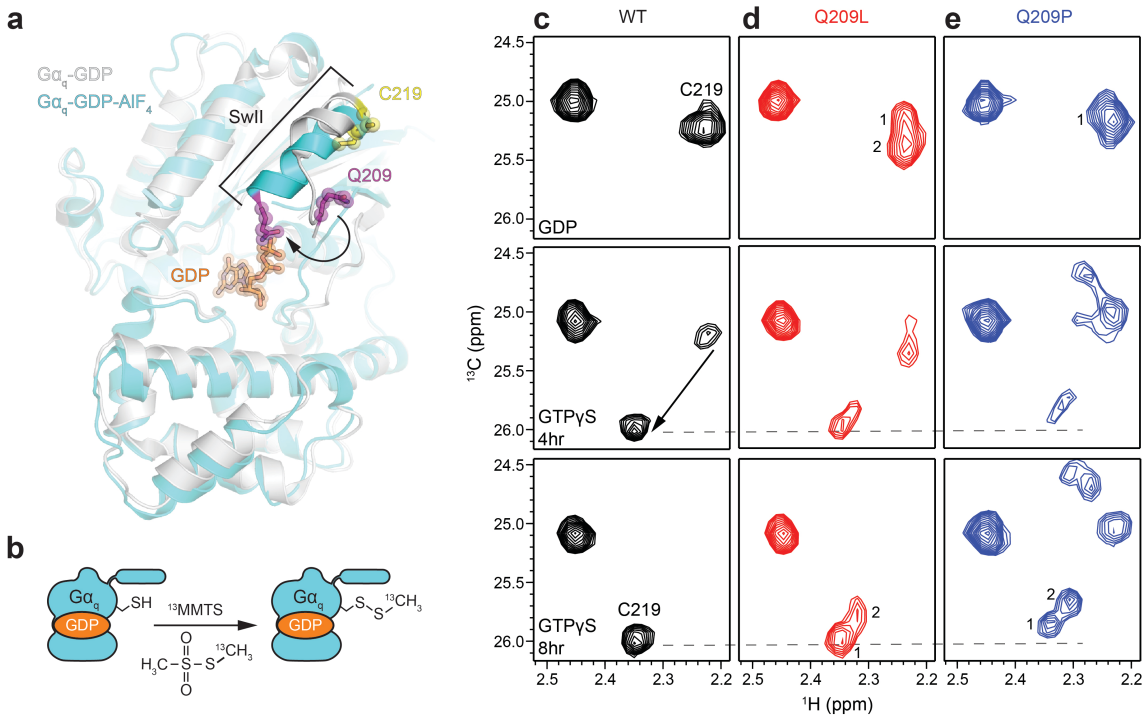

Figure 2.1 Oncogenic $G\alpha_q$ isoforms show enhanced conformational heterogeneity of SwII
(a) Rearrangement and local ordering of SwII α-helix between $G\alpha_q$-GDP (PDB 3AH8 ref[23]) and $G\alpha_q$-GDP-AlF_4 (PDB 7SQ2 ref[30]) conformations.(b) Cartoon depiction of site-specific incorporation of S-methyl-^{13}C methanethiosulfonate (^{13}C-MMTS) NMR probe[28] to study SwII dynamics.^{1}H–^{13}C heteronuclear single quantum coherence (HSQC) NMR spectra of ^{13}C-MMTS (c) WT (d) Q209L and (e) Q209P $G\alpha_q$-GDP at 0, 4, and 8 hours post-addition of Mg^{2+} and GTPγS, recorded at 25 °C, 800 MHz. Spectra are representative images from one biological replicate.

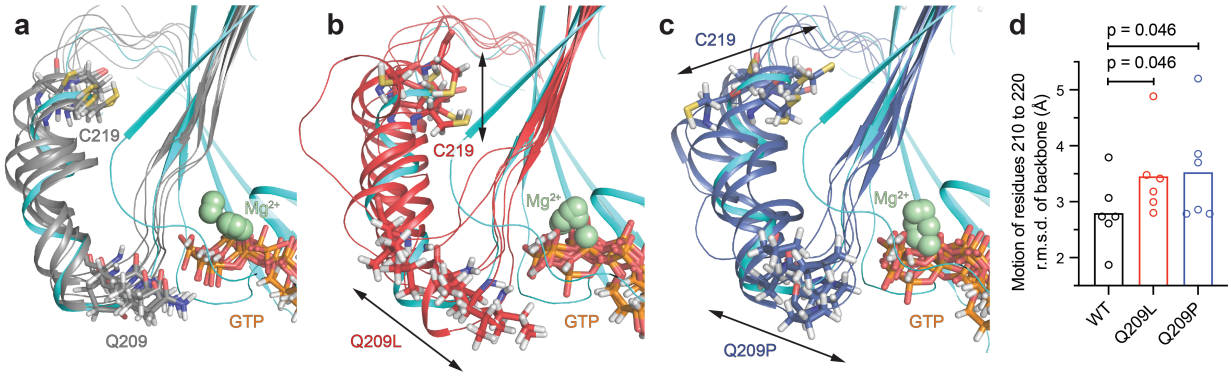

Figure 2.2 Molecular dynamics simulations show increased mobility of SwII in oncogenic $G\alpha_q$ isoforms

Molecular dynamics simulation snapshots for (a) WT (b) Q209L and (c) Q209P $G\alpha_q$-GTP. The starting structure (PDB 5DO9 ref[33]) is shown in cyan. Residues 209 and C219 are shown for clarity. (d) Quantitation of SwII backbone mobility in molecular dynamics simulations as measured by root mean square deviation (r.m.s.d.) of backbone atoms (residues 210 to 220) from the starting structure. Bar graphs show mean r.m.s.d. computed across six independent molecular dynamics simulations. Individual r.m.s.d. values that were averaged across each independent 2-μs simulation are shown. There is a significant increase in SwII backbone mobility in Q209L (P = 0.046) and Q209P (P = 0.046) $G\alpha_q$-GTP simulations compared to WT $G\alpha_q$-GTP simulations (Mann-Whitney U-test).

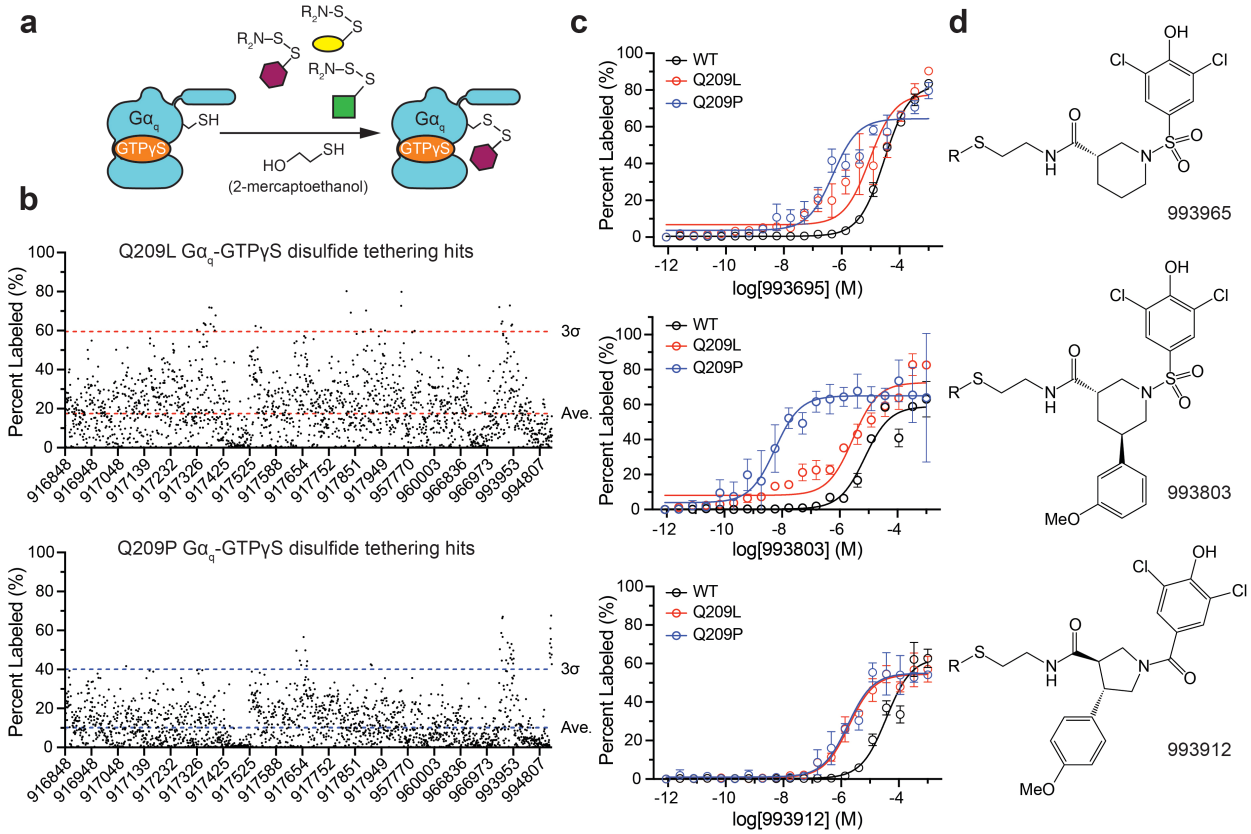

Figure 2.3 Identification of mutant-selective disulfide-containing fragments
(a) Cartoon depiction of disulfide-containing fragment screening[34] against $G\alpha_q$-GTPγS. (b) Global covalent modification of Q209L and Q209P $G\alpha_q$-GTPγS by disulfide-containing fragment library (~1850 compounds) as determined by LC/MS. Average covalent labeling across all compounds was calculated. Hits were defined as compounds labeling greater than three standard deviations (3σ) above average. Data were collected with one technical replicate per compound.(c) LC/MS dose-response of mutant-selective disulfide-containing fragments binding to WT, Q209L, and Q209P $G\alpha_q$-GTPγS. Individual data points represent mean compound labeling from three technical replicates in one biological replicate. Error bars represent standard deviation among technical replicates. (d) Chemical structures of lead, mutant-selective disulfide-containing fragments.

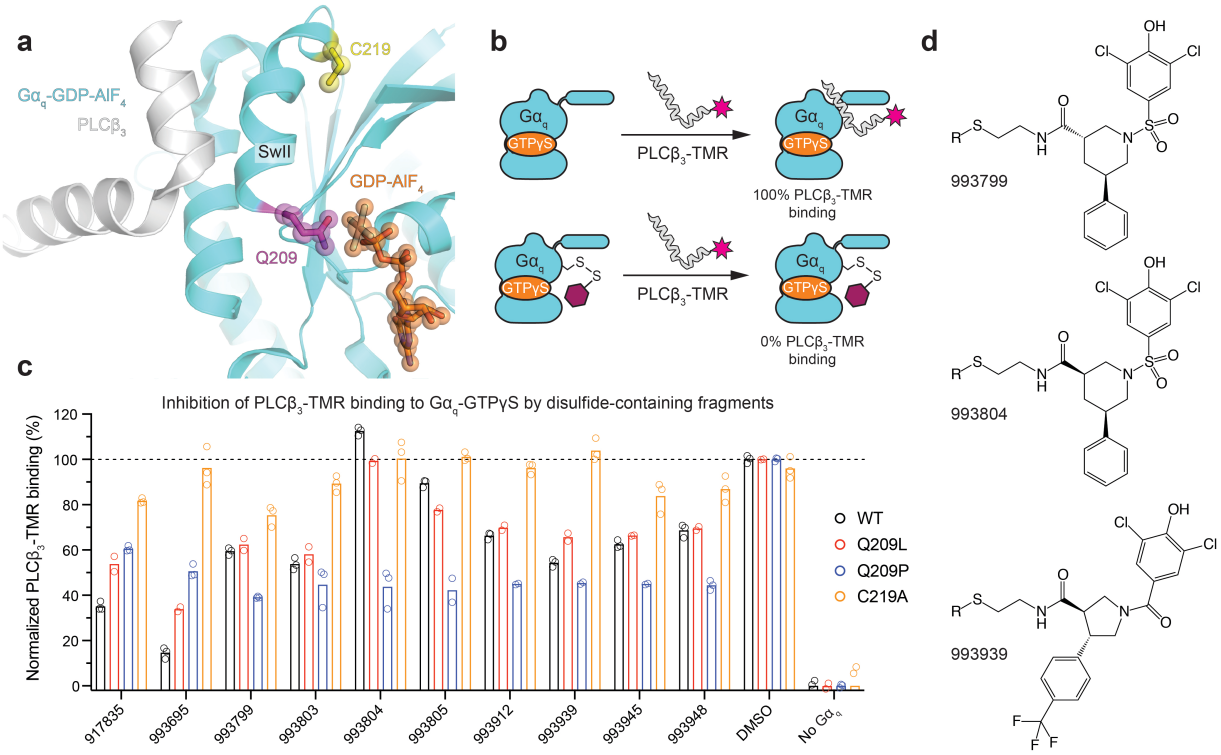

Figure 2.4 Disulfide-containing fragments non-selectively inhibit binding of $G\alpha_q$ effector derived peptides

(a) $PLC\beta_3$-$G\alpha_q$-GDP-AlF_4 SwII binding interface (PDB 7SQ2 ref[30]), showing proximity of C219, the anticipated site of covalent modification by disulfide-containing fragments. (b) Cartoon depiction of $PLC\beta_3$-derived peptide ($PLC\beta_3$-TMR) fluorescence polarization assay. Disulfide-containing fragments that prevent $PLC\beta_3$-TMR binding to $G\alpha_q$-GTPγS decrease fluorescence polarization of the peptide.(c) Inhibition of $PLC\beta_3$-TMR binding to WT, Q209L, Q209P, and C219A $G\alpha_q$-GTPγS. Individual technical replicates from one biological replicate are shown. Raw fluorescent polarization values (mP units) were normalized to vehicle (DMSO) and no $G\alpha_q$-GTPγS controls as 100% and 0% binding, respectively.

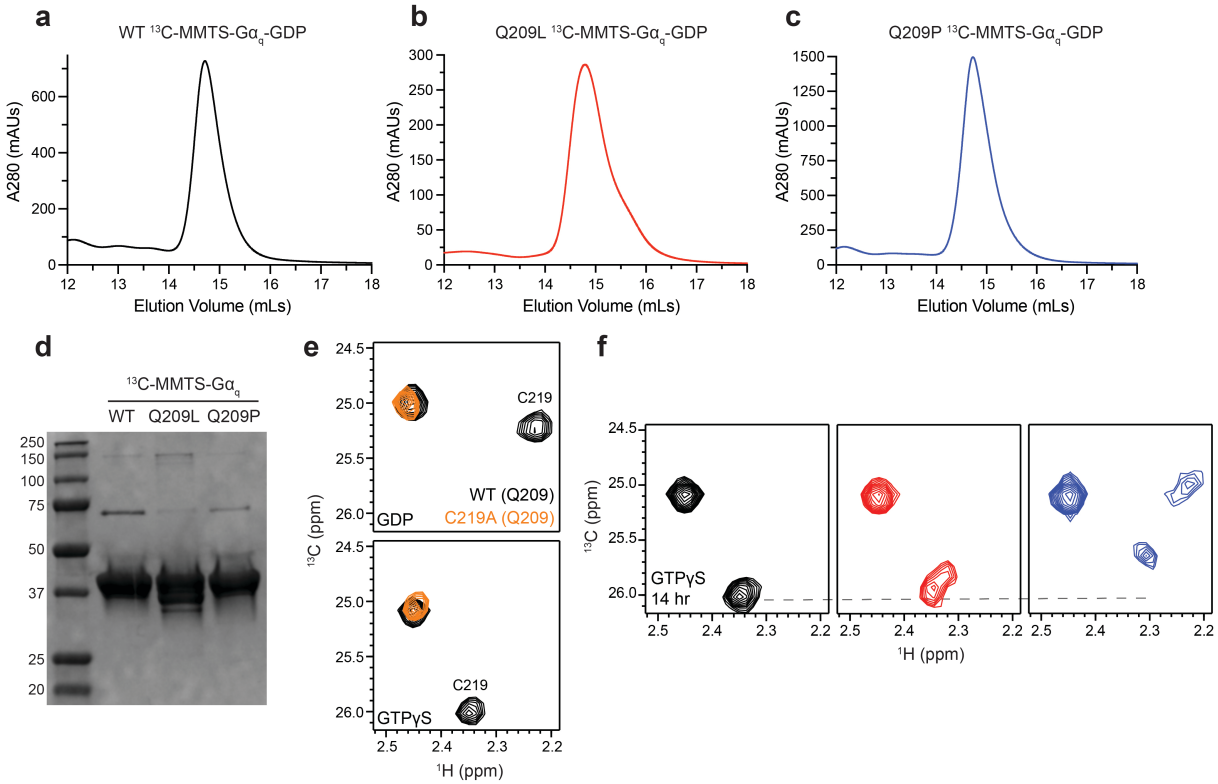

Extended Data Figure 2.1. Biochemistry and assignment of ^{13}C-MMTS-labeled Gα$_q$
Size-exclusion chromatography of ^{13}C-MMTS-labeled (A) WT (b) Q209L (c) Q209P Gα$_q$-GDP. Representative chromatograms from two independent biological replicates are shown.
(d) Coomassie stained SDS-PAGE of ^{13}C-MMTS-labeled WT, Q209L, and Q209P Gα$_q$. (e) Assignment of C219 SwII ^{1}H–^{13}C HSQC peak was obtained by measuring ^{13}C-MMTS-labeled C219A Gα$_q$-GDP and C219A Gα$_q$-GTPγS, recorded at 25 °C, 800 MHz. (f) ^{1}H–^{13}C HSQC NMR spectra of ^{13}C-MMTS WT, Q209L, and Q209P 14 hours after addition of Mg^{2+} and GTPγS, recorded at 25 °C, 800 MHz.

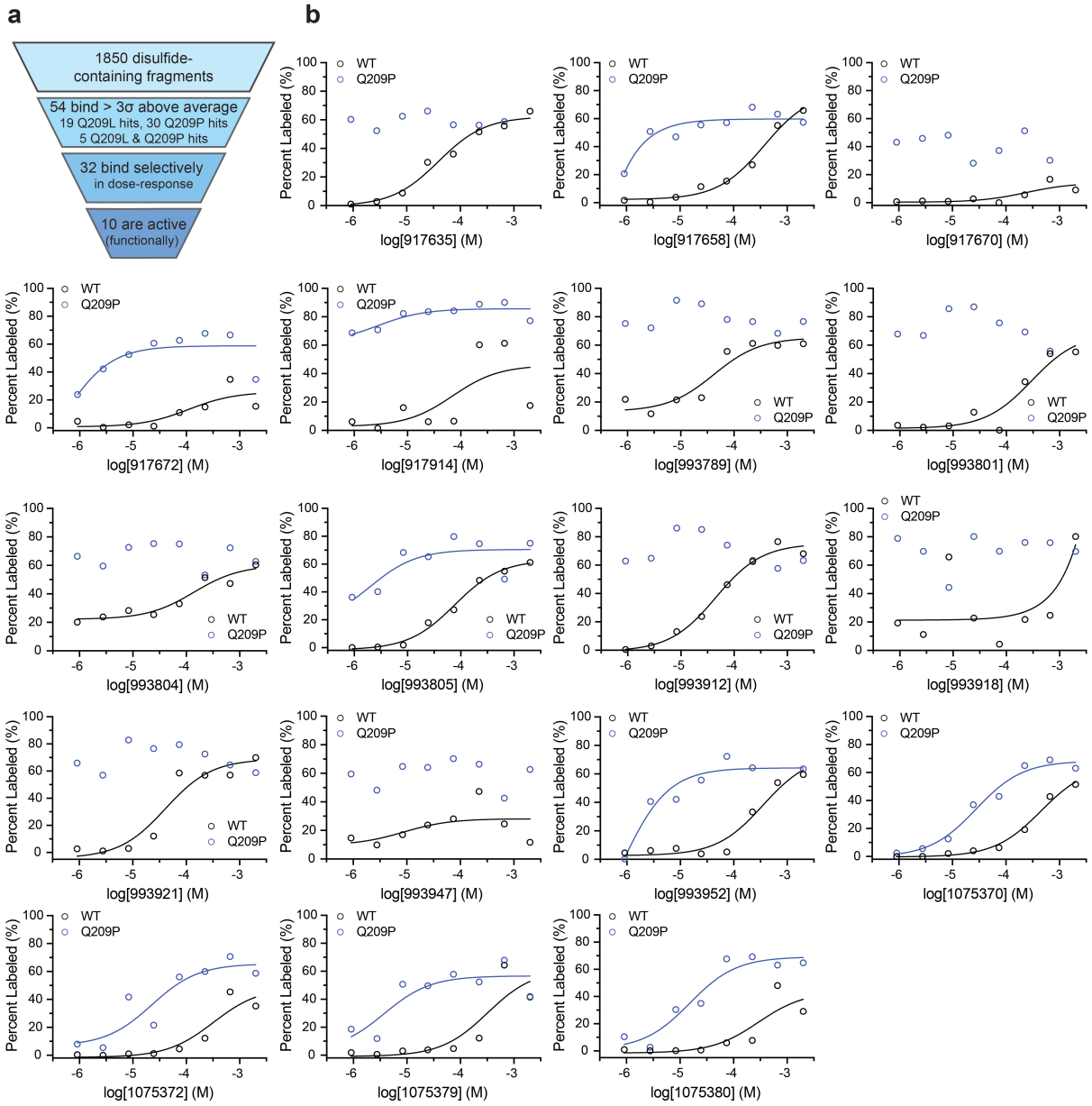

Extended Data Figure 2.2 Disulfide-containing fragment screening strategy and LC/MS dose-response labeling assay of lead molecules

(a) Disulfide-containing fragment screening strategy. A library of 1,850 disulfide-containing fragments were screened against Q209L and Q209P $G\alpha_q$-GTPγS in a liquid chromatography mass spectrometry (LC/MS) assay[34]. Hits were defined as compounds labeling Q209L or Q209P $G\alpha_q$-GTPγS three standard deviations (3σ) above average. Fifty-four hit compounds were counter-screened against WT $G\alpha_q$-GTPγS in a LC/MS dose-response labeling assay. Thirty-two compounds demonstrated putative oncogene-selective binding. Of the thirty available oncogene-selective fragments, ten compounds were functionally active in the $PLC\beta_3$-TMR fluorescence polarization assay. (b) LC/MS dose-response curves for disulfide-containing fragments against WT and Q209P $G\alpha_q$-GTPγS. Eighteen of the thirty tested Q209P hit compounds showed putative oncogene selectivity and are shown here. Data are unicate from one biological experiment.

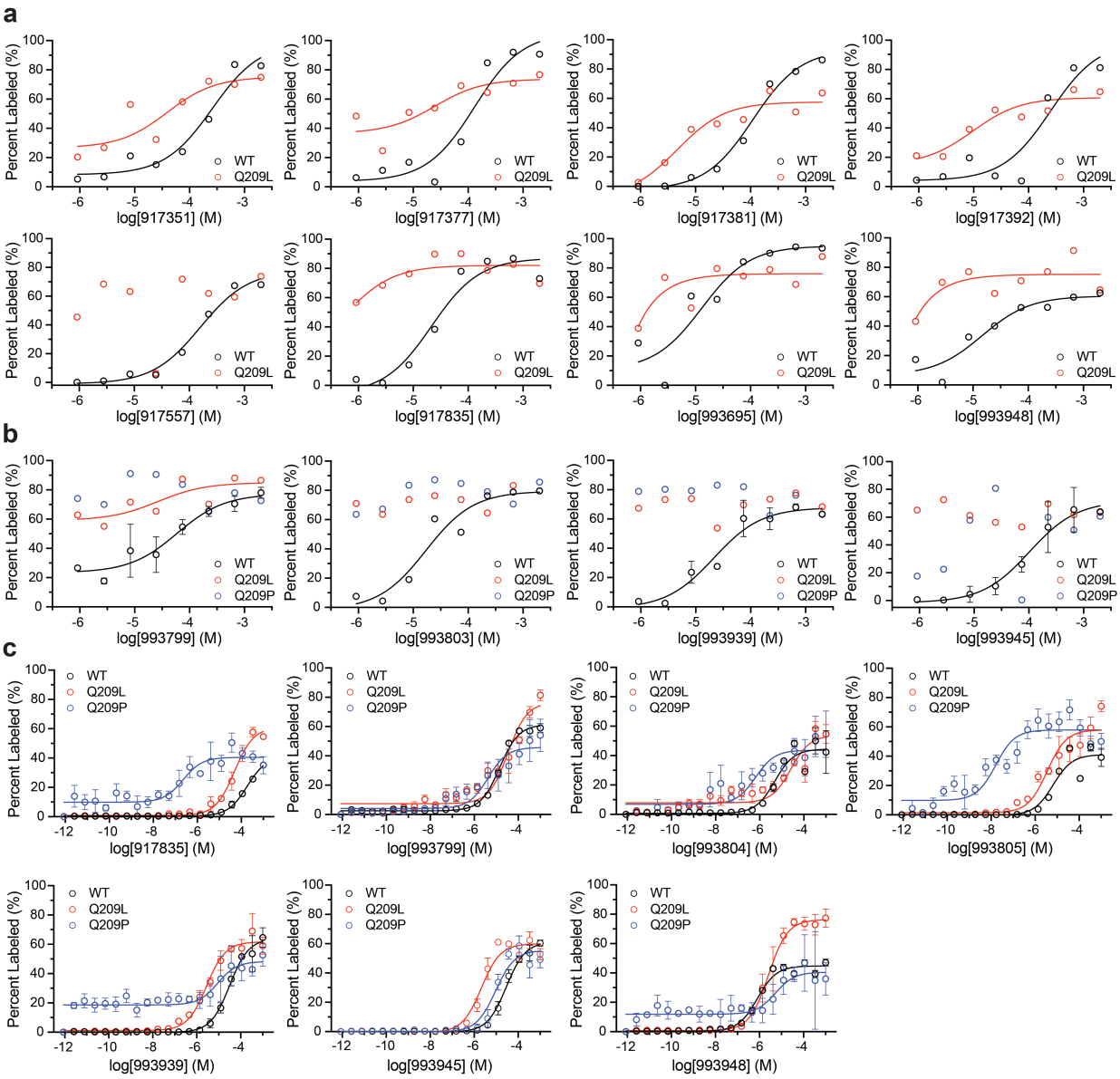

Extended Data Figure 2.3 LC/MS dose-response labeling assay of lead molecules
(a) LC/MS dose-response curves for disulfide-containing fragments against WT and Q209L $G\alpha_q$-GTPγS. Eight of the nineteen tested Q209L hit compounds showed putative oncogene selectivity and are shown here. Data represent unicate from one biological experiment. (b) LC/MS dose-response curves for disulfide-containing fragments against WT, Q209L, and Q209P $G\alpha_q$-GTPγS. Four of the five tested Q209L and Q209P hit compounds showed putative oncogene selectivity and are shown here. Data represent technical replicates from one biological experiment. (c) Extended 20-point dose-response LC/MS assay for best 10 mutant-selective compounds. Data represent mean and standard deviation from triplicate measurements in one biological experiment.

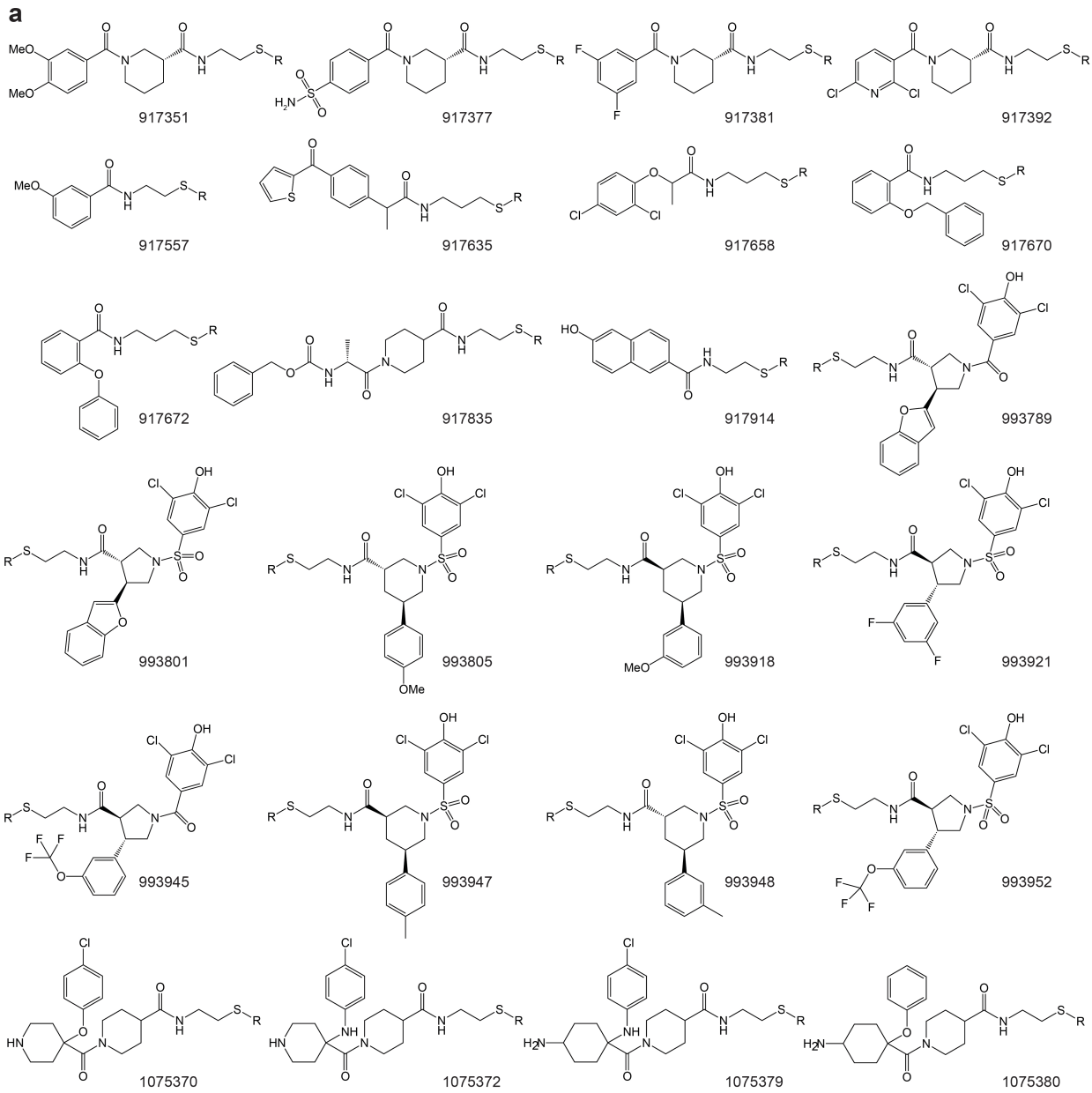

Extended Data Fig 2.4 Chemical structures of functionally tested disulfide-containing fragments

(a) Chemical structures of disulfide-containing fragments that were tested in the PLCβ_3-TMR fluorescence polarization assay.

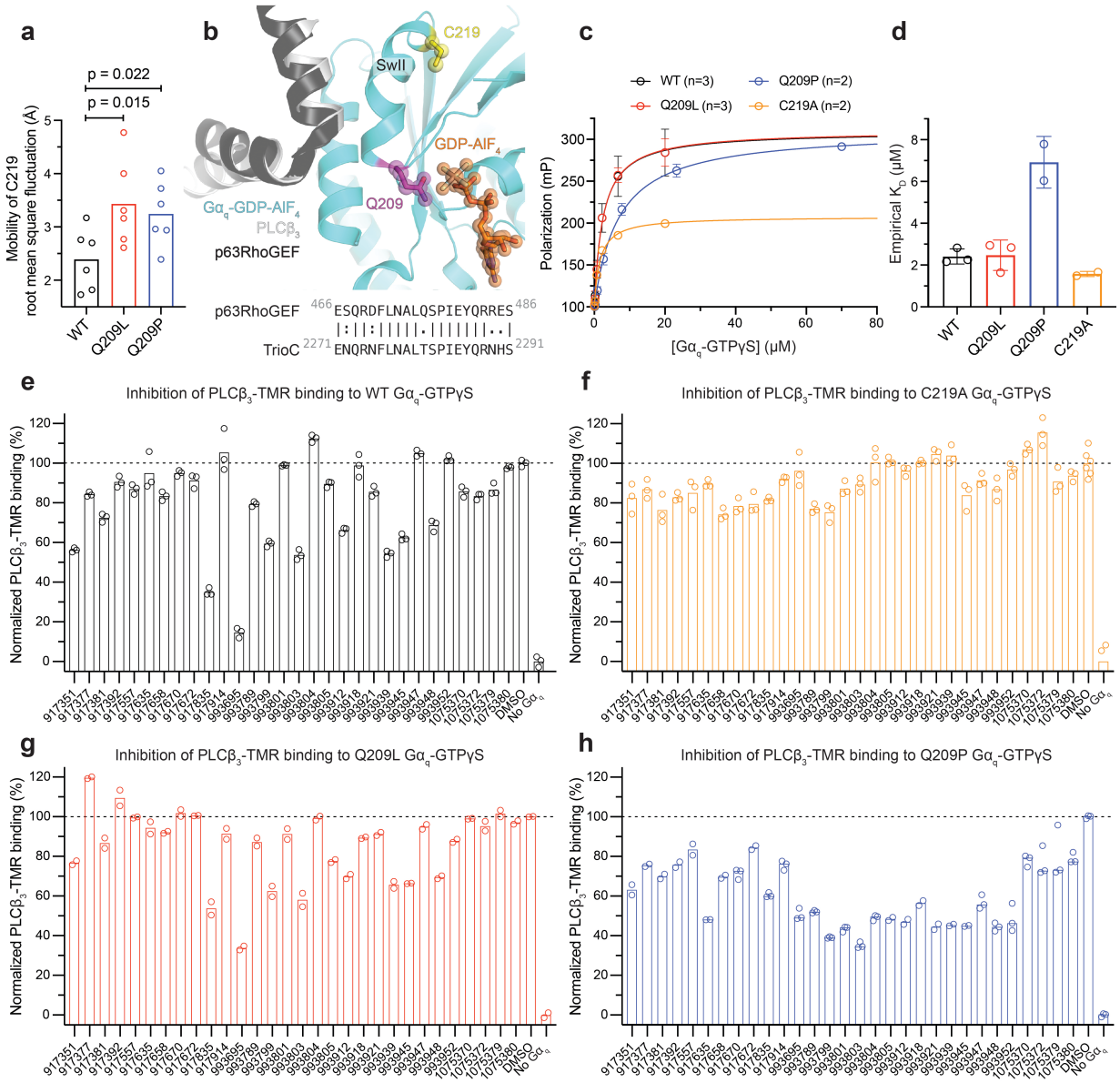

Extended Data Figure 2.5 Probing disulfide-containing fragment activity with PLCβ$_3$-TMR fluorescence polarization assay

(See next page for caption)

Extended Data Figure 2.5 Probing disulfide-containing fragment activity with PLCβ$_3$-TMR fluorescence polarization assay

Quantitation of C219 mobility in molecular dynamics simulations as measured by root mean square fluctuation (r.m.s.f.), computed from all C219 atoms. Bar graphs show mean r.m.s.f. across six independent molecular dynamics simulations. Individual r.m.s.f. values that were averaged across each independent simulation are shown. There is a significant increase in C219 mobility in Q209L (P = 0.015) and Q209P (P = 0.022) Gα$_q$-GTP simulations compared to WT Gα$_q$-GTP simulations (Mann-Whitney U-test). (b) Gα$_q$-GDP-AlF$_4$ SwII binding interface with Gα$_q$-effector proteins: PLCβ$_3$ (PDB 7SQ2 ref[30]) and p63RhoGEF (PDB 2RGN ref[32]). PLCβ$_3$ and p63RhoGEF bind to a similar region on Gα$_q$-GDP-AlF$_4$ SwII. The 21-amino acid SwII binding motif of p63RhoGEF is aligned with close homolog TrioC (86% sequence similarity). (c) PLCβ$_3$-TMR saturation binding isotherms to Gα$_q$-GTPγS. Data points represent mean fluorescent polarization across independent biological replicates (WT, n = 3; Q209L, n = 3; Q209P, n = 2; C219A, n= 2). Error bars represent standard deviation of mean fluorescent polarization across biological replicates. (d) Empirically determined K_D for PLCβ$_3$-TMR binding to Gα$_q$-GTPγS. Bar graphs represent mean K_D across biological replicates (WT, n = 3; Q209L, n = 3; Q209P, n = 2; C219A, n= 2). Data points represent independently fit K_D values from biological replicates. Error bars show standard deviation of independently fit K_D values across biological replicates. Inhibition of PLCβ$_3$-TMR binding to (e) WT, (f) C219A, (g) Q209L and (h) Q209P Gα$_q$-GTPγS by disulfide-containing fragments. Individual technical replicates from one biological replicate are shown. Raw fluorescent polarization values (mP units) were normalized to vehicle (DMSO) and no Gα$_q$-GTPγS controls as 100% and 0% binding, respectively.

Publishing Agreement

It is the policy of the University to encourage open access and broad distribution of all theses, dissertations, and manuscripts. The Graduate Division will facilitate the distribution of UCSF theses, dissertations, and manuscripts to the UCSF Library for open access and distribution. UCSF will make such theses, dissertations, and manuscripts accessible to the public and will take reasonable steps to preserve these works in perpetuity.

I hereby grant the non-exclusive, perpetual right to The Regents of the University of California to reproduce, publicly display, distribute, preserve, and publish copies of my thesis, dissertation, or manuscript in any form or media, now existing or later derived, including access online for teaching, research, and public service purposes.

DocuSigned by:
Julian Harris
7F938B30FF274B3...
Author Signature

5/15/2022
Date